学 位 論 文

Numerical Simulation with a Finite Element Method for the Development of Mechanical and Thermal Structure in Subduction Zones

有限要素法を用いたプレート沈み込み帯の

力学的－熱的構造発達シミュレーション

平成 20 年 3 月 博士（理学）申請

東京大学大学院理学系研究科

地球惑星科学専攻

鹿倉 洋介

Abstract

Topography in plate subduction zones is formed as the result of interaction between the internal crustal processes such as igneous activity and tectonic deformation due to plate subduction and the external surface processes such as erosion and sedimentation controlled by climate and environment. In the present study we focus on the internal crustal processes and reveal the mechanism governing the development of mechanical and thermal structure in plate subduction zones through numerical simulation with a mechanical-thermal interaction model.

In the numerical simulation of mechanical and thermal structure development in plate subduction zones, the following points are essential: 1) rational representation of plate-to-plate interaction, 2) realistic modeling of rheological structure, and 3) interaction between mechanical and thermal processes. For the first point, we rationally represented the plate-to-plate interaction by the increase of tangential displacement discontinuity (fault slip) at plate interfaces. For the second point, we modeled the realistic rheological structure of subduction zones with a finite element method (FEM). As to the third point, we constructed a mechanical-thermal interaction model by combining a thermal FEM model for temperature changes due to thermal diffusion and advection with a mechanical FEM model for internal velocity fields due to plate subduction through a temperature-dependent constitutive equation prescribing rheological properties of materials.

First, we developed a mechanical FEM model to compute the long-term internal velocity fields for a simple subduction zone, which is modeled by an elastic continental plate and an elastic oceanic plate descending into an underlying viscoelastic half-space. The steady plate subduction is represented by the steady increase of tangential

displacement discontinuity at the interface between the continental and oceanic plates (Matsu'ura & Sato, 1989). The most direct way to obtain the internal velocity fields is to solve a boundary value problem for the elastic-viscoelastic composite medium in the time domain, but it is very difficult even in a simple case. In order to avoid the difficulty in computation, we applied the corresponding principle of linear elasticity (Lee, 1955; Radok, 1957) and the equivalent theorem (Fukahata & Matsu'ura, 2006) to the elastic-viscoelastic problem, and reduced it to a simple elastic problem, which is formally obtained from the original elastic-viscoelastic problem by regarding the underlying viscoelastic half-space as the elastic half-space with the rigidity of zero. Then, we can use a standard elastic FEM to construct a mechanical model for computing long-term internal velocity fields due to steady plate subduction in a realistic situation. In the construction of the mechanical FEM model, we represented the tangential displacement discontinuity at the plate interface with the split node technique (Melosh & Raefsky, 1981). The negative and positive buoyancy effects related to surface uplift and subsidence were incorporated into the stress-free conditions at the Earth's surface (Williams & Richardson, 1991). When we take the rigidity of the underlying elastic half-space to be zero, the computational instability called "volumetric locking" arises. We resolved this computational instability by using the selective-reduced integration scheme in FEM computation algorithm (Hughes, 1980).

With the mechanical FEM model we computed the internal velocity fields due to steady plate subduction and obtained the following results. In the case of a horizontally layered model, the long-term internal deformation fields calculated from the FEM model almost completely agree with those from analytical expressions by Fukahata & Matsu'ura (2006). In the case of a descending slab model, the maximum surface uplift rate in the overriding plate is significantly faster than that in the case of the horizontally layered

model. If the descending slab is thicker, the uplift zone in the overriding plate and the subsidence zone around the trench become broader, and the uplift and subsidence rates become faster. If the overriding plate is thicker, the subsidence pattern around the trench does not change significantly, but the uplift pattern in the overriding plate changes notably.

Next, we developed the thermal FEM model to compute temperature changes due to thermal diffusion and advection. In the development of the thermal FEM model, we considered three sources of advection; the subduction of the cold oceanic slab, the mantle flow induced by slab subduction, and the vertical deformation of the overriding plate. With the thermal FEM model we computed temporal change in thermal structure for given internal velocity fields. The computed results show that the third source is less effective in heat transfer, but crucial to understand the mechanism governing the geomorphic development in plate subduction zones.

Finally, combining the thermal FEM model with the mechanical FEM model, we constructed a mechanical-thermal interaction model. In this model the mechanical-thermal interaction is described through a temperature-dependent constitutive equation prescribing rheological properties of materials; that is, the temperature-dependence of the mantle viscosity by Courtney & Beaumont (1983). With the mechanical-thermal interaction model, we numerically simulated the development of mechanical and thermal structure in a plate subduction zone. In this simulation, at a certain time step, we compute internal velocity fields due to plate subduction. Then, using the computed internal velocity fields, we evaluate temperature changes due to thermal diffusion and advection, and update the boundaries between the lithosphere and the asthenosphere to compute internal velocity fields at the next time step. Following such a computation algorithm, we revealed the evolution process of mechanical and thermal structure in the plate subduction zone over a

span of 5 Myr. In the early stages of plate subduction (0-2 Myr), the cooling of the mantle wedge leads to the thickening of the overriding lithosphere near the plate boundary and increases the uplift rates of the lithosphere beneath the island arc. As time goes on, the thinning of the lithosphere beneath the island arc proceeds, and the uplift rates further increase. This simulation result indicates that the mechanical-thermal interaction is crucial to understand the geomorphic evolution in plate subduction zones.

Contents

Chapter 1. Introduction

Topography in plate subduction zones is formed as the result of interaction between the internal crustal processes such as igneous activity and tectonic deformation due to plate subduction and the external surface processes such as erosion and sedimentation controlled by climate and environment. The internal processes cause surface uplift and subsidence, while the external processes even the Earth's surface through mass transfer from highlands to lowlands. Therefore, we can regard the internal and external processes as active and passive processes, respectively. In the present study we focus on the internal crustal processes in plate subduction zones.

The steady subduction of oceanic plates beneath continental plates causes not only the deformation of the elastic plates but also steady flow in the Earth's mantle. These internal deformation processes transfer heat in advection and change temperature distribution in subduction zones. Since the rheological properties of the mantle strongly depend on temperature, the change in temperature will lead to the change of mechanical structure in subduction zones. This means that the mechanical-thermal interaction is essential to understand the mechanism governing the development of mechanical and thermal structure in subduction zones. Since the mechanical-thermal interaction is very complicated, one of the best ways to quantitatively understand the mechanism governing the internal processes in subduction zones is physics-based numerical simulation. In the numerical simulation the following points are essential: 1) rational representation of plate-to-plate interaction, 2) realistic modeling of rheological structure, and 3) interaction between mechanical and thermal processes.

For the representation of plate-to-plate interaction, several models have been

proposed. For example, Giunchi et al. (1996) and Toth & Gurnis (1998) give the horizontal velocity of a descending oceanic plate relative to the overriding continental plate at the end of the oceanic plate as a boundary condition to represent the plate-to-plate interaction. In such external loading models the compressive stress fields produced in oceanic plates become uniform in space. This contradicts seismological observations. On the other hand, Bott et al. (1989), Wdowinski & O'Connell (1991), Giunchi et al. (1994), Zong & Gurnis (1994) and Billen & Gurnis (2001) have proposed more physical models counting the negative buoyancy of cold descending slabs as driving force. These models may be categorized as a kind of mantle convection models. Since plate motion is considered to be the appearance of the thermal convection of the Earth's mantle on the surface, the most orthodox way to represent the plate-to-plate interaction would be physics-based mantle convection modeling. The purpose of the numerical simulations based on the mantle convection models is to reproduce actual plate subduction processes; that is, the 3-D geometry of descending slabs and their relative velocities to overriding plates. As yet, unfortunately, this purpose has not achieved. On the other hand, we can now precisely determine the actual 3-D geometry of plate interfaces from seismological observations (e.g., Hashimoto et al., 2004) and the actual relative velocities among plates from space-based geodetic measurements such as GPS, SLR and VLBI (e.g., Sella et al., 2002). Given the 3-D plate interface geometry and relative plate velocities, we can compute internal velocity fields due to plate-to-plate interaction by solving a kind of boundary value problems in continuum mechanics. In this approach the plate-to-plate interaction is rationally represented by the increase of tangential displacement discontinuity (fault slip) at plate interfaces (Matsu'ura & Sato, 1989). The tangential displacement discontinuity is mathematically

equivalent to the force system of a double couple with no net force and no net torque (Maruyama, 1963; Burridge & Knopoff, 1964). Therefore, giving the increase rate of tangential displacement discontinuity at a plate interface means specifying the increase rate of internal force acting on the plate interface produced by the plate-to-plate interaction. With such a kinematic approach based on elastic/viscoelastic dislocation theory, Matsu'ura and his coworkers have succeeded in explaining island arc-trench formation in subduction zones (Sato & Matsu'ura, 1992, 1993; Hashimoto et al., 2004), tectonic deformation processes in the India-Eurasia collision zone (Takada & Matsu'ura, 2004, 2007), and tectonic evolution in the Mariana back-arc region (Hashima et al., 2008). In these studies, however, the lithosphere-asthenosphere system in subduction zones is simply modeled by an elastic surface layer overlying a viscoelastic half-space.

In subduction zones, elastic oceanic plates are mechanically interacting with overriding elastic plates, and descending into the viscoelastic mantle. Then, FEM modeling is very useful for the realistic representation of rheological structure in subduction zones. Actually, in the studies of long-term crustal deformation in subduction zones, various types of FEM models have been used. For example, Zhong & Gurnis (1994) and Toth & Gurnis (1998) independently developed 2-D viscous fluid FEM models. Giunchi et al. (1994) constructed a 2-D viscoelastic FEM model with TECTON (Melosh & Raefsky, 1980), and Giunchi et al. (1996) constructed a 2-D viscoelastic FEM model with MARC (Marc Analysis Research Corp., 1994). Billen & Gurnis (2001) constructed a 3-D viscous fluid FEM model with CITCOM (Moresi & Gurnis, 1996).

The mechanical process and the thermal process interact with each other in two ways. First, the internal velocity field induced by oceanic plate subduction transfers heat

in advection and changes temperature distribution in subduction zones. Second, the change in temperature leads to the change of rheological structure in subduction zones. Many researchers have studied thermal structure in subduction zones (e.g., Hasebe et al., 1970; Honda, 1985; Furukawa, 1993). For the development of thermal structure, England & Richardson (1977), Koons (1987), Royden (1993), Platt & England (1994), and Fukahata & Matsu'ura (2000) have studied from various points of view and concluded that the advection term is essential in the development of thermal structure in subduction zones. As the sources of advection we can consider the subduction of cold oceanic slabs, the mantle flow induced by slab subduction, and the vertical deformation of overriding plates. According to Fukahata & Matsu'ura (2000), the third source is less effective in heat transfer, but crucial to understand the mechanism governing the geomorphic development in subduction zones. Second, the change in temperature leads to the change of rheological structure in subduction zones. The temperature dependence of mantle viscosity has been studied, for example, by Courtney & Beaumont (1983). On the basis of their temperature-viscosity relation, Toth & Gurnis (1998) studied the development of mechanical and thermal structure at the early stage of plate subduction.

In the present study, on the basis of these considerations, we construct a mechanical-thermal interaction model by combining a thermal FEM model for temperature change with a mechanical FEM model for internal deformation. In Chapter 2, we develop a mechanical FEM model to compute long-term internal velocity fields due to steady plate subduction. We show that the problem can be reduced to a simple elastic problem by applying the corresponding principle of linear elasticity (Lee, 1955; Radok, 1957) and the equivalent theorem (Fukahata & Matsu'ura, 2006) to the original elastic-viscoelastic problem. With the mechanical FEM model we compute the internal

velocity fields due to steady plate subduction for some representative cases. In Chapter 3, we develop a thermal FEM model to compute temperature changes due to thermal diffusion and advection. Then, combining the thermal FEM model with the mechanical FEM model, we construct a mechanical-thermal interaction model and numerically simulate the development of mechanical and thermal structure in a plate subduction zone. In Chapter 4, we discuss the applicability and limitation of the present models through the comparison of the simulation results with observations.

Chapter 2. Long-term Internal Deformation in Subduction Zones

We develop a mechanical FEM model to compute the long-term internal velocity fields for a simple plate subduction zone, which is modeled by an elastic continental plate and an elastic oceanic plate descending into an underlying viscoelastic half-space. The steady plate subduction is represented by the steady increase of tangential displacement discontinuity at the interface between the continental and oceanic plates (Matsu'ura & Sato, 1989). In order to solve the elastic-viscoelastic boundary value problem, we apply the corresponding principle of linear elasticity (Lee, 1955; Radok, 1957) and the equivalent theorem (Fukahata & Matsu'ura, 2006), and reduce it to a simple elastic boundary value problem. Then, we construct a mechanical FEM model with the split node technique (Melosh & Raefsky, 1981) for representing tangential displacement discontinuity at plate interfaces, the modified traction free condition (Williams & Richardson, 1991) for taking account of the gravitational effects of surface uplift and subsidence, and the selective-reduced integration scheme (Hughes, 1980) for resolving the computational instability called "volumetric locking."

2.1 Mathematical formulation of a quasi-static viscoelastic problem

We consider a quasi-static problem for internal deformation due to the steady increase of tangential displacement discontinuity (fault slip) at an interface Σ between an elastic continental plate and an elastic oceanic plate descending into the underlying Maxwellian viscoelastic asthenosphere. In general, given the quasi-static displacements $U_i(\boldsymbol{x},t;\boldsymbol{\xi},\tau)$ at the point $\boldsymbol{x}$ and time t due to a unit-step tangential displacement

discontinuity (fault slip) at the point $\boldsymbol{\xi}$ and time τ on the plate interface Σ, which are called step response functions hereafter, we can calculate the quasi-static viscoelastic displacements $u_i(\boldsymbol{x},t)$ due to arbitrary spatiotemporal fault slip distribution $\Delta u(\boldsymbol{\xi},\tau)$ by using the technique of hereditary integral as

$$u_i(\mathbf{x},t) = \int_{-\infty}^{t}\int_{\Sigma} U_i(\mathbf{x},t-\tau;\boldsymbol{\xi},0)\frac{\partial \Delta u(\boldsymbol{\xi},\tau)}{\partial \tau} d\boldsymbol{\xi} d\tau \,. \tag{2.1}$$

Long-term velocity fields due to steady plate subduction

In the case of steady plate subduction, the spatiotemporal fault slip distribution is given by $\Delta u = V_{pl} t H(t)$, and so Eq. (2.1) becomes

$$u_i(\mathbf{x},t) = V_{pl}\int_{0}^{t}\int_{\Sigma} U_i(\mathbf{x},t-\tau;\boldsymbol{\xi},0) d\boldsymbol{\xi} d\tau \,. \tag{2.2}$$

For sufficiently large t in comparison with the stress relaxation time τ_v of the viscoelastic asthenosphere, we can regard the step response functions as constants $U_i(\boldsymbol{x},t\to\infty;\boldsymbol{\xi},0)$ in time. Then, Eq. (2.2) can be written as

$$\begin{aligned} u_i(\mathbf{x},t) &= V_{pl}\int_{0}^{t_c}\int_{\Sigma} U_i(\mathbf{x},t-\tau;\boldsymbol{\xi},0) d\boldsymbol{\xi} d\tau \\ &\quad + V_{pl}(t-t_c)\int_{\Sigma} U_i(\mathbf{x},t\to\infty;\boldsymbol{\xi},0) d\boldsymbol{\xi} \end{aligned}, \tag{2.3}$$

where t_c denotes a time much larger than τ_v. Since the first term on the right hand side of Eq. (2.3) is independent of time, the partial derivatives of $u_i(\boldsymbol{x},t)$ with respect to time, namely velocity components, for $t >> \tau_v$ are given by

$$v_i(\mathbf{x},t) \equiv \frac{\partial}{\partial t} u_i(\mathbf{x},t) = V_{pl}\int_{\Sigma} U_i(\mathbf{x},t\to\infty;\boldsymbol{\xi},0) d\boldsymbol{\xi} \,. \tag{2.4}$$

That is, for the computation of long-term velocity fields due to steady plate subduction, we need only the values of slip response functions at $t\to\infty$.

Viscoelastic slip response functions

Now we consider quasi-static internal deformation due to uniform unit-step slip $H(t)$ at an interface Σ between an elastic continental plate Ω^{e2} and an elastic oceanic plate Ω^{e1} descending into an underlying Maxwellian viscoelastic half-space Ω^{v}. Denoting displacement components by u_i $(i=1,2,3)$, strain components by ε_{ij} $(i,j=1,2,3)$, and stress components by σ_{ij} $(i,j=1,2,3)$, we can describe the quasi-static boundary value problem by a set of the following equations in tensor form: the equation of equilibrium

$$\frac{\partial \sigma_{ij}}{\partial x_j} + f_i = 0, \tag{2.5}$$

the definition of strain

$$\varepsilon_{ij} = \frac{1}{2}\left(\frac{\partial u_i}{\partial x_j} + \frac{\partial u_j}{\partial x_i}\right), \tag{2.6}$$

the constitutive equations

$$\begin{cases} \sigma'_{ij} = 2\mu^e \varepsilon'_{ij} \\ \sigma_{kk} = 3\kappa^e \varepsilon_{kk} \end{cases} \quad \text{in } \Omega^{e1} \text{ and } \Omega^{e2} \tag{2.7}$$

and

$$\begin{cases} \dfrac{\partial}{\partial t}\sigma'_{ij} + \dfrac{\mu^v}{\eta}\sigma'_{ij} = 2\mu^v \dfrac{\partial}{\partial t}\varepsilon'_{ij} \\ \sigma_{kk} = 3\kappa^v \varepsilon_{kk} \end{cases} \quad \text{in } \Omega^{v} \tag{2.8}$$

with

$$\begin{cases} \sigma'_{ij} = \sigma_{ij} - \dfrac{1}{3}\sigma_{kk}\delta_{ij} \\ \varepsilon'_{ij} = \varepsilon_{ij} - \dfrac{1}{3}\varepsilon_{kk}\delta_{ij} \end{cases}, \tag{2.9}$$

and boundary conditions at the ground surface $x_3 = 0$ and the plate Σ

$$\begin{cases} \sigma_{13} = \sigma_{23} = 0, \quad \sigma_{33} - \rho^e g u_3 = 0 & \text{at the Earth's surface } x_3 = 0 \\ \Delta u = H(t) & \text{at the plate interface } \Sigma \end{cases} . \tag{2.10}$$

Here, $\mu^{e(v)}$, $\kappa^{e(v)}$, η and ρ^e are the rigidity, bulk modulus, viscosity and density of the corresponding medium, respectively, and g denotes the acceleration of gravity at the Earth's surface. In this description, as can be seen from Eq. (2.10), the plate-to-plate mechanical interaction is represented by the unit-step tangential displacement discontinuity at the plate interface, and the effect of gravity is incorporated into the traction free conditions at the Earth's surface. Therefore, the body force term f_i $(i = 1, 2, 3)$ in Eq. (2.5) is actually zero.

Solving the above boundary value problem in a direct way, we will be able to obtain a quasi-static viscoelastic solution in the time domain. However, it is not easy matter, because the constitutive equation of the viscoelastic medium in Eq. (2.8) includes the time derivatives of stress and strain components.

The correspondence principle of linear viscoelasticity

In order to obtain the explicit expressions for the slip response functions $U_i(\boldsymbol{x}, t; \boldsymbol{\xi}, 0)$, we can use the correspondence principle of linear viscoelasticity (Lee, 1955; Radok, 1957). Performing Laplace transformation to a set of equations (2.5)- (2.8) and (2.10), which describes the viscoelastic boundary value problem, we obtain

$$\frac{\partial \tilde{\sigma}_{ij}}{\partial x_j} + \tilde{f}_i = 0 , \tag{2.11}$$

$$\tilde{\varepsilon}_{ij} = \frac{1}{2}\left(\frac{\partial \tilde{u}_i}{\partial x_j} + \frac{\partial \tilde{u}_j}{\partial x_i} \right), \tag{2.12}$$

$$\begin{cases} \tilde{\sigma}'_{ij} = 2\mu^e \tilde{\varepsilon}'_{ij} \\ \tilde{\sigma}_{kk} = 3\kappa^e \tilde{\varepsilon}_{kk} \end{cases} \quad \text{in } \Omega^{e1} \text{ and } \Omega^{e2}, \tag{2.13}$$

$$\begin{cases} \tilde{\sigma}'_{ij} = 2\dfrac{s\mu^v}{s+1/\tau_v}\tilde{\varepsilon}'_{ij} \\ \tilde{\sigma}_{kk} = 3\kappa^v \tilde{\varepsilon}_{kk} \end{cases} \quad \text{in } \Omega^v \tag{2.14}$$

and

$$\begin{cases} \tilde{\sigma}_{13} = \tilde{\sigma}_{23} = 0, \quad \tilde{\sigma}_{33} - \rho^e g\tilde{u}_3 = 0 & \text{at the Earth's surface } x_3 = 0 \\ \Delta\tilde{u} = \dfrac{1}{s} & \text{at the plate interface } \Sigma \end{cases}. \tag{2.15}$$

Here, s is the Laplace transform variable and the tilde denotes the Laplace transform of the corresponding physical quantity.

Introducing the Laplace operator $\hat{\mu}^v(s)$ defined by

$$\hat{\mu}^v(s) = \frac{s\mu^v}{s+1/\tau_v}, \tag{2.16}$$

we can rewrite Eq. (2.14) as

$$\begin{cases} \tilde{\sigma}'_{ij} = 2\hat{\mu}^v(s)\tilde{\varepsilon}'_{ij} \\ \tilde{\sigma}_{kk} = 3\kappa^v \tilde{\varepsilon}_{kk} \end{cases} \quad \text{in } \Omega^v. \tag{2.17}$$

From comparison between Eq. (2.13) and Eq. (2.17), we can see that the Laplace transform of the constitutive equation for the viscoelastic medium Ω^v is formally identical with that for the elastic media Ω^{e1} and Ω^{e2}, except that the rigidity μ^v is replaced with the s-dependent operator $\hat{\mu}^v(s)$. This means that the viscoelastic boundary value problem in the s domain is mathematically parallel to the associated elastic boundary value problem in the time domain. Then, applying the corresponding principle of linear viscoelasticity (Lee, 1955; Radok, 1957) to the associated elastic solution $U_i^e(\boldsymbol{x}, t>0; \boldsymbol{\xi}, 0 \,|\, \mu^e, \kappa^e, \mu^v, \kappa^v)$, we obtain the viscoelastic solution in the s

domain as

$$\tilde{U}_i(\boldsymbol{x},s;\boldsymbol{\xi}) = \frac{1}{s} U_i^e(\boldsymbol{x},t>0;\boldsymbol{\xi},0 \,|\, \mu^e,\kappa^e,\hat{\mu}^v(s),\kappa^v) \tag{2.18}$$

The viscoelastic solution in the time domain can be obtained by performing the inverse Laplace transformation of Eq. (2.18).

The equivalence theorem

In the present study we are interested in the steady velocity fields after complete stress relaxation in the viscoelastic medium Ω^v. With the limiting value theorem in the Laplace transformation we can directly evaluate the ultimate values of the slip response functions $U_i(\boldsymbol{x},t;\boldsymbol{\xi},0)$ at $t \to \infty$ from the viscoelastic solution $\tilde{U}_i(\boldsymbol{x},s;\boldsymbol{\xi})$ in the s domain as:

$$U_i(\boldsymbol{x},t\to\infty;\boldsymbol{\xi},0) = \lim_{s\to 0} s\tilde{U}_i(\boldsymbol{x},s;\boldsymbol{\xi}) \tag{2.19}$$

Substituting Eq. (2.18) into the above equation, we obtain

$$U_i(\boldsymbol{x},t\to\infty;\boldsymbol{\xi},0) = \lim_{s\to 0} U_i^e(\boldsymbol{x},t>0;\boldsymbol{\xi},0 \,|\, \mu^e,\kappa^e,\hat{\mu}^v(s),\kappa^v) \tag{2.20}$$

In this expression the s-dependence appears only through the s-dependent operator $\hat{\mu}^v(s)$. From the explicit expressions for $\hat{\mu}^v(s)$ in Eq. (2.16) we obtain its limiting values at $s \to 0$ as

$$\lim_{s\to 0} \hat{\mu}^v(s) = \lim_{s\to 0} \frac{s\mu^v}{s+1/\tau_v} = 0 \tag{2.21}$$

Then, we may rewrite Eq. (2.20) as

$$U_i(\boldsymbol{x},t\to\infty;\boldsymbol{\xi},0) = U_i^e(\boldsymbol{x},t>0;\boldsymbol{\xi},0 \,|\, \mu^e,\kappa^e,\mu^v\to 0,\kappa^v) \tag{2.22}$$

This relation is known as the equivalence theorem (Fukahata & Matsu'ura, 2006), which means that the viscoelastic step response at $t \to \infty$ is mathematically equivalent

to the associated elastic response with $\mu^v \to 0$. In other words, we can directly obtain the steady solution of the viscoelastic boundary value problem by solving the associated elastic boundary value problem with $\mu^v \to 0$ in the region corresponding to the viscoelastic medium.

2.2 A numerical model for internal deformation with FEM

In Section 2.1 we showed that long-term internal velocity fields due to steady plate subduction could be obtained by solving the associated elastic problem. In this section we develop a mechanical FEM model to compute the internal velocity fields with several special techniques in a standard elastic FEM. First, we show the way to construct the stiffness equation in elastic problems. Then, we describe the three special techniques used for model construction; that is, the split node technique by Melosh & Raefsky (1981) to represent tangential displacement discontinuity at plate interfaces, the FEM representation for traction free condition at the Earth's surface by Williams & Richardson (1991) to include the gravitational effects of surface uplift and subsidence, and the Selective-Reduced Integration (SRI) scheme by Hughes (1980) to resolve the computational instability called "volumetric locking".

Basic equations for quasi-static, plane strain problems

We consider a quasi-static, plane strain problem for steady plate subduction at a constant rate V_{pl} as shown in Fig. 1, where the y-axis is taken vertically downward, and the $y = 0$ plane represents the Earth's surface. The *x*- and *z*-axes are taken to be perpendicular and parallel to the strike of a plate boundary, respectively. The oceanic and continental plates (Ω^{e1} and Ω^{e2}) are assumed to be normally elastic, and the

underlying asthenosphere (Ω^v) to be elastic but very weak in shear on the basis of Eq. (2.22). In plane strain problems, the *x*- and y-displacement components (*u* and *v*) are independent of *z*, and the z-component (*w*) is zero:

$$u = u(x, y), \quad v = v(x, y), \quad w = 0 . \tag{2.23}$$

So, the nonzero strain components are ε_{xx}, ε_{xy} and ε_{yy}, and the nonzero independent stress components are σ_{xx}, σ_{xy} and σ_{yy} (the stress component σ_{zz} is nonzero, but not independent). Here, all the displacement components, the strain components and the stress components are the function of x and y (independent of *z*). Then, we can describe the quasi-static boundary value problem by a set of the following equations: the equation of equilibrium

$$\begin{cases} \dfrac{\partial \sigma_{xx}}{\partial x} + \dfrac{\partial \sigma_{xy}}{\partial y} = -f_x \\ \dfrac{\partial \sigma_{xy}}{\partial x} + \dfrac{\partial \sigma_{yy}}{\partial y} = -f_y \end{cases}, \tag{2.24}$$

the definition of strain

$$\begin{cases} \varepsilon_{xx} = \dfrac{\partial u}{\partial x} \\ \varepsilon_{yy} = \dfrac{\partial v}{\partial y} \\ 2\varepsilon_{xy} = \dfrac{\partial u}{\partial y} + \dfrac{\partial v}{\partial x} \end{cases}, \tag{2.25}$$

the constitutive equations

$$\begin{cases} \sigma_{xx} = \left(\kappa^e + \dfrac{4}{3}\mu^e\right)\varepsilon_{xx} + \left(\kappa^e - \dfrac{2}{3}\mu^e\right)\varepsilon_{yy} \\ \sigma_{yy} = \left(\kappa^e - \dfrac{2}{3}\mu^e\right)\varepsilon_{xx} + \left(\kappa^e + \dfrac{4}{3}\mu^e\right)\varepsilon_{yy} \\ \sigma_{xy} = 2\mu^e \varepsilon_{xy} \end{cases} \quad \text{in } \Omega^{e1} \text{ and } \Omega^{e2} \tag{2.26}$$

and

$$\begin{cases} \sigma_{xx} = \left(\kappa^v + \frac{4}{3}\mu^v\right)\varepsilon_{xx} + \left(\kappa^v - \frac{2}{3}\mu^v\right)\varepsilon_{yy} \\ \sigma_{yy} = \left(\kappa^v - \frac{2}{3}\mu^v\right)\varepsilon_{xx} + \left(\kappa^v + \frac{4}{3}\mu^v\right)\varepsilon_{yy} \qquad \text{in } \Omega^v \quad (\mu^v \to 0), \\ \sigma_{xy} = 2\mu^v \varepsilon_{xy} \end{cases} \tag{2.27}$$

and boundary conditions

$$\begin{cases} \sigma_{xy} = 0, \quad \sigma_{yy} - \rho g v = 0 & \text{at the Earth's surface } (y = 0) \\ \Delta u = V_{pl} t H(t) & \text{at the plate interface } \Sigma \end{cases}. \tag{2.28}$$

Here, we supposed that the oceanic plate subduction started at the time $t = 0$ at a constant rate V_{pl}, and took the gravitationally equilibrium state before the initiation of plate subduction as the reference to measure the displacement, strain and stress. The driving force of plate subduction is represented by the steady increase of tangential displacement discontinuity, $\Delta u = V_{pl} t H(t)$, at the plate interface Σ.

The stiffness equation for quasi-static, plane strain problems

From Eqs (2.24), (2.25) and (2.26) or (2.27), we can obtain Navier's equation for quasi-static, plane strain problems in matrix form:

$$\boldsymbol{S}^T \boldsymbol{D} \boldsymbol{S} \boldsymbol{u} = -\boldsymbol{f}, \tag{2.29}$$

where $\boldsymbol{S}$ is the 3×2 differential operator matrix, $\boldsymbol{D}$ is the 3×3 elasticity matrix, $\boldsymbol{u}$ is the 2×1 displacement vector, and $\boldsymbol{f}$ is the 2×1 force vector, defined by

$$\boldsymbol{S} = \begin{bmatrix} \frac{\partial}{\partial x} & 0 \\ 0 & \frac{\partial}{\partial y} \\ \frac{\partial}{\partial y} & \frac{\partial}{\partial x} \end{bmatrix}, \quad \boldsymbol{D} = \begin{bmatrix} \kappa + \frac{4}{3}\mu & \kappa - \frac{2}{3}\mu & 0 \\ \kappa - \frac{2}{3}\mu & \kappa + \frac{4}{3}\mu & 0 \\ 0 & 0 & \mu \end{bmatrix}, \quad \boldsymbol{u} = \begin{pmatrix} u \\ v \end{pmatrix}, \quad \boldsymbol{f} = \begin{pmatrix} f_x \\ f_y \end{pmatrix}. \tag{2.30}$$

Denoting the boundary of the region Ω by Γ, the mechanical boundary condition

(traction boundary condition) is represented as

$$(\boldsymbol{DSu})\cdot\boldsymbol{n}=\boldsymbol{t} \qquad \text{on } \Gamma_t, \tag{2.31}$$

where $\boldsymbol{t}$ is the specific traction vector acting on the boundary Γ_t with the outward unit normal vector $\boldsymbol{n}$. On the other hand, the geometric boundary condition (displacement boundary condition) is represented as

$$\boldsymbol{u}=\boldsymbol{d} \qquad \text{on } \Gamma_d, \tag{2.32}$$

where $\boldsymbol{d}$ is the specific displacement vector on Γ_d. It should be noted that the mechanical boundary Γ_t and the geometric boundary Γ_d satisfy the following conditions:

$$\Gamma_t \bigcap \Gamma_d = 0 \quad \text{and} \quad \Gamma_t \bigcup \Gamma_d = \Gamma. \tag{2.33}$$

Eqs (2.29), (2.31) and (2.32) compose the boundary value problem in the strong form.

The weak form representation of the boundary value problem can be obtained as follows. Multiplying the both sides of Eq. (2.29) by arbitrary virtual displacement $\delta\boldsymbol{u}^*$ that satisfies $\delta\boldsymbol{u}^*=\boldsymbol{0}$ on Γ_d, and integrating them over the region Ω, we obtain

$$\int_\Omega (\boldsymbol{S}\delta\boldsymbol{u}^*)^T\boldsymbol{DSu}d\Omega = -\int_\Omega \delta\boldsymbol{u}^{*T}\boldsymbol{f}\,d\Omega. \tag{2.34}$$

Applying the Green's theorem to the left hand side of the above equation, we obtain

$$\int_\Omega \delta\boldsymbol{u}^{*T}(\boldsymbol{S}^T\boldsymbol{DSu})d\Omega = \int_\Omega \delta\boldsymbol{u}^{*T}\boldsymbol{f}\,d\Omega + \int_\Gamma \delta\boldsymbol{u}^{*T}(\boldsymbol{DSu})\cdot\boldsymbol{n}d\Gamma. \tag{2.35}$$

Since $\delta\boldsymbol{u}^*=\boldsymbol{0}$ on Γ_d, we can rewrite Eq. (2.35) as

$$\int_\Omega (\boldsymbol{S}\delta\boldsymbol{u}^*)^T\boldsymbol{DSu}dV = \int_\Omega \delta\boldsymbol{u}^{*T}\boldsymbol{f}\,d\Omega + \int_{\Gamma_t} \delta\boldsymbol{u}^{*T}\boldsymbol{t}\,d\Gamma. \tag{2.36}$$

This gives the weak form representation of the boundary value problem.

Now we divide the region Ω into a number of finite elements, and represent the displacement field $\boldsymbol{u}$ in each element Ω_e by the nodal displacement vector $\boldsymbol{u}_i$ ($i=1,...,p$) with interpolation functions $N_i(x,y)$:

$$\boldsymbol{u}(x,y) \simeq \sum_{i=1}^{p} N_i(x,y)\boldsymbol{u}_i \ . \tag{2.37}$$

In the same way, we approximate the virtual displacement field, $\delta\boldsymbol{u}^*$, and the strain fields, $\boldsymbol{Su}$ and $\boldsymbol{S}\delta\boldsymbol{u}^*$, in Ω_e as

$$\delta\boldsymbol{u}^*(x,y) \simeq \sum_{i=1}^{p} N_i(x,y)\delta\boldsymbol{u}_i^* \tag{2.38}$$

and

$$\boldsymbol{Su} \simeq \sum_{i=1}^{p} \boldsymbol{B}_i\boldsymbol{u}_i, \quad \boldsymbol{S}\delta\boldsymbol{u}^* \simeq \sum_{i=1}^{p} \boldsymbol{B}_i\delta\boldsymbol{u}_i^* \tag{2.39}$$

with

$$\boldsymbol{B}_i = \begin{bmatrix} \dfrac{\partial N_i}{\partial x} & 0 \\ 0 & \dfrac{\partial N_i}{\partial y} \\ \dfrac{\partial N_i}{\partial y} & \dfrac{\partial N_i}{\partial x} \end{bmatrix}. \tag{2.40}$$

Then, we obtain the approximate representation of Eq. (2.36) as

$$\int_{\Omega_e} \delta\boldsymbol{u}_\alpha^{*T} \boldsymbol{B}_\alpha{}^T \boldsymbol{D}\boldsymbol{B}_\beta \boldsymbol{u}_\beta \ d\Omega = \int_{\Omega_e} \delta\boldsymbol{u}_\alpha^{*T} N_\alpha^T \boldsymbol{f} \ d\Omega + \int_{\Gamma_t \cap \Omega_e} \delta\boldsymbol{u}_\alpha^{*T} N_\alpha^T \boldsymbol{t} \, d\Gamma \ . \tag{2.41}$$

Here, the repetition of subscript, α and β, in a term denotes a summation with respect to that subscript over its range $(\alpha, \beta = 1, 2, ..., p)$. From Eq. (2.41), since $\delta\boldsymbol{u}_\alpha^*$ are arbitrary nodal displacement vectors, we obtain the stiffness equation for each element Ω_e as

$$\boldsymbol{K}_{\alpha\beta}^e \boldsymbol{u}_\beta = \boldsymbol{f}_\alpha^e \qquad (\alpha = 1, ...p) \tag{2.42}$$

with

$$\boldsymbol{K}_{\alpha\beta}^e = \int_{\Omega_e} \boldsymbol{B}_\alpha^T \boldsymbol{D}\boldsymbol{B}_\beta d\Omega \tag{2.43}$$

$$\boldsymbol{f}_\alpha^e = \int_{\Omega_e} N_\alpha^T \boldsymbol{f} \ d\Omega + \int_{\Gamma_t \cap \Omega_e} N_\alpha^T \boldsymbol{t} \, d\Gamma \ . \tag{2.44}$$

Here, $\boldsymbol{K}_{\alpha\beta}^{e}$ is the element stiffness matrix, and $\boldsymbol{f}_{\alpha}^{e}$ is the element equivalent nodal force vector. Constructing the stiffness equations (2.42) for all nodes and superposing them, we finally obtain the global stiffness equation:

$$\boldsymbol{KU} = \boldsymbol{F}, \tag{2.45}$$

where $\boldsymbol{U}$ is the unknown vector of nodal displacements, $\boldsymbol{F}$ is the known nodal force vector, and $\boldsymbol{K}$ is the known stiffness matrix.

In order to obtain the explicit expressions of $\boldsymbol{F}$ and $\boldsymbol{K}$, we must specify the shape of elements. In the present study we use the isoparametric bilinear quadrilateral element ($p = 4$). We introduce a local coordinate system defined for each element. The mapping from the global coordinate system (x, y) to the local coordinate system (ξ, η) is done as

$$\begin{cases} x(\xi,\eta) = \sum_{i=1}^{4} N_i(\xi,\eta) x_i^e \\ y(\xi,\eta) = \sum_{i=1}^{4} N_i(\xi,\eta) y_i^e \end{cases}, \tag{2.46}$$

with

$$\begin{cases} N_1(\xi,\eta) = \frac{1}{4}(1-\xi)(1-\eta) \\ N_2(\xi,\eta) = \frac{1}{4}(1+\xi)(1-\eta) \\ N_3(\xi,\eta) = \frac{1}{4}(1+\xi)(1+\eta) \\ N_4(\xi,\eta) = \frac{1}{4}(1-\xi)(1+\eta) \end{cases}, \tag{2.47}$$

where (x_i^e, y_i^e) denote the given node point coordinates. In the same way, by using the nodal displacements (u_i^e, v_i^e), the displacement field in the element is represented as

$$\begin{cases} u(\xi,\eta) = \sum_{i=1}^{4} N_i(\xi,\eta) u_i^e \\ v(\xi,\eta) = \sum_{i=1}^{4} N_i(\xi,\eta) v_i^e \end{cases} . \tag{2.48}$$

Then, the element stiffness matrix in Eq. (2.43) can be written as

$$\boldsymbol{K}_{\alpha\beta}^e = \int_{\Omega_e} \boldsymbol{B}_\alpha^T \boldsymbol{D} \boldsymbol{B}_\beta d\Omega = \int_{-1}^{1}\int_{-1}^{1} \boldsymbol{B}_\alpha^T \boldsymbol{D} \boldsymbol{B}_\beta J(\xi,\eta) d\xi d\eta \ , \tag{2.49}$$

where J is the Jacobean defined by

$$J(\xi,\eta) = \begin{vmatrix} \partial x/\partial\xi & \partial y/\partial\xi \\ \partial x/\partial\eta & \partial y/\partial\eta \end{vmatrix} . \tag{2.50}$$

By using the Gauss-Legendre numerical integration formula, the definite integral on the right hand side of Eq. (2.49) is carried out as

$$\boldsymbol{K}_{\alpha\beta}^e = \sum_{p=1}^{4} \left[\boldsymbol{B}_\alpha^T \boldsymbol{D} \boldsymbol{B}_\beta J \right]_{\substack{\xi=\xi_p \\ \eta=\eta_p}} . \tag{2.51}$$

where (ξ_p, η_p) denote the evaluation points given by

$$(\xi_p,\eta_p) = \left(-\frac{1}{\sqrt{3}}, -\frac{1}{\sqrt{3}}\right), \left(\frac{1}{\sqrt{3}}, -\frac{1}{\sqrt{3}}\right), \left(\frac{1}{\sqrt{3}}, \frac{1}{\sqrt{3}}\right), \left(-\frac{1}{\sqrt{3}}, \frac{1}{\sqrt{3}}\right). \tag{2.52}$$

As to the nodal force vector $\boldsymbol{F}$, in a similar way, the first term of the element nodal force vector in Eq. (2.44) can be evaluated as

$$\int_{\Omega_e} N_\alpha^T \boldsymbol{f} \ d\Omega = \boldsymbol{f} \int_{-1}^{+1}\int_{-1}^{+1} N_\alpha J d\xi d\eta = \boldsymbol{f} \sum_{p=1}^{4} \left[N_\alpha J \right]_{\substack{\xi=\xi_p \\ \eta=\eta_p}} . \tag{2.53}$$

Split node technique to represent displacement discontinuity

The FEM schemes for modeling displacement discontinuity in elastic material have been proposed by Jungle & Fazier (1973), Smith (1974), Melosh & Raefsky (1981), and

Melosh & Williams (1989). In the present study, in order to represent tangential displacement discontinuity (fault slip) at a plate interface in FEM, we use the split node technique by Melosh & Raefsky (1981).

As shown in the previous part of this section, the fundamental equation in the finite element analysis of quasi-static, plane strain problems is the global stiffness equation in Eq. (2.45), which is obtained by superposing the local stiffness matrix equations in Eq. (2.42):

$$\boldsymbol{K}^e_{\alpha\beta}\boldsymbol{u}_\beta = \boldsymbol{f}^e_\alpha \qquad (\alpha = 1,...p) \tag{2.42}$$

In the split node technique, the displacements at shared nodes are not equal, but differ by a fixed amount. This technique is explained by a simple 1-D example, for which we choose a 3-nodes-2-elements truss problem. The schematic explanation for the split node technique in a 1-D problem is shown in Fig. 2(a). In this case, each element has two nodes. The displacements $\boldsymbol{u}_\beta$ are related to the forces $\boldsymbol{f}^e_\alpha$ through the local stiffness matrix $\boldsymbol{K}^e_{\alpha\beta}$ as

$$\begin{bmatrix} K^e_{11} & K^e_{12} \\ K^e_{21} & K^e_{22} \end{bmatrix} \begin{bmatrix} U^e_1 \\ U^e_2 \end{bmatrix} = \begin{bmatrix} F^e_1 \\ F^e_2 \end{bmatrix} \qquad (e = 1, 2), \tag{2.54}$$

where U^e_i and F^e_i are the displacement and force at the node i of the element e, respectively. At normal nodes the global displacements $\underline{U}_i$ and global forces $\underline{F}_i$ are related to the local displacements U^e_j and the local forces F^e_j by the simple rules: $\underline{U}_1 = U^1_1$, $\underline{U}_2 = U^1_2 = U^2_1$ and $\underline{U}_3 = U^2_2$, and $\underline{F}_1 = F^1_1$, $\underline{F}_2 = F^1_2 + F^2_1$ and $\underline{F}_3 = F^2_2$. Thus, the global stiffness equation becomes

$$\begin{bmatrix} K^1_{11} & K^1_{12} & 0 \\ K^1_{21} & K^1_{22} + K^2_{11} & K^2_{12} \\ 0 & K^2_{21} & K^2_{22} \end{bmatrix} \begin{bmatrix} \underline{U}_1 \\ \underline{U}_2 \\ \underline{U}_3 \end{bmatrix} = \begin{bmatrix} \underline{F}_1 \\ \underline{F}_2 \\ \underline{F}_3 \end{bmatrix}. \tag{2.55}$$

When the global node 2 is the split node, we write the displacement at the node 2 of the element 1 as $U_2^1 = \langle U_2^1 \rangle + \Delta U_2^1$ and that of the element 2 as $U_1^2 = \langle U_1^2 \rangle + \Delta U_1^2$. Taking $\langle U_2^1 \rangle$ and $\langle U_1^2 \rangle$ to be the common displacement, the difference between ΔU_2^1 and ΔU_1^2 gives the relative displacement. Thus, the rule for assembly is $\underline{U}_2 = \langle U_2^1 \rangle = \langle U_1^2 \rangle$ and $\Delta U_1^2 = -\Delta U_2^1$, and the local stiffness equation for the element 1 becomes

$$\begin{bmatrix} K_{11}^1 & K_{12}^1 \\ K_{21}^1 & K_{22}^1 \end{bmatrix} \begin{bmatrix} U_1^1 \\ \langle U_2^1 \rangle + \Delta U_2^1 \end{bmatrix} = \begin{bmatrix} F_1^1 \\ F_2^1 \end{bmatrix}. \tag{2.56}$$

The above equation can be rewritten as

$$\begin{bmatrix} K_{11}^1 & K_{12}^1 \\ K_{21}^1 & K_{22}^1 \end{bmatrix} \begin{bmatrix} U_1^1 \\ \langle U_2^1 \rangle \end{bmatrix} = \begin{bmatrix} F_1^1 - K_{12}^1 \Delta U_2^1 \\ F_2^1 - K_{22}^1 \Delta U_2^1 \end{bmatrix}. \tag{2.57}$$

For the element 2 we obtain a similar equation. The fully assembled global stiffness equation is

$$\begin{bmatrix} K_{11}^1 & K_{12}^1 & 0 \\ K_{21}^1 & K_{22}^1 + K_{11}^2 & K_{12}^2 \\ 0 & K_{21}^2 & K_{22}^2 \end{bmatrix} \begin{bmatrix} \underline{U}_1 \\ \underline{U}_2 \\ \underline{U}_3 \end{bmatrix} = \begin{bmatrix} \underline{F}_1 - K_{12}^1 \Delta U_2^1 \\ \underline{F}_2 - K_{22}^1 \Delta U_2^1 - K_{11}^2 \Delta U_1^2 \\ \underline{F}_3 - K_{21}^2 \Delta U_1^2 \end{bmatrix}. \tag{2.58}$$

This splitting induces fictitious forces on the nodes adjacent to the split node, as well as the split node itself.

In Fig. 2 (b), we show the split node model in a 2-D plane strain problem. Here, we set the nodes 2 and 5 as the splitting nodes: that is, the displacement discontinuity is distributed on the face between the node 2 and the node 5 in the global number. In this case, we obtain the following local stiffness equation for the element 1:

$$\begin{bmatrix} \boldsymbol{K}_{11}^1 & \boldsymbol{K}_{12}^1 & \boldsymbol{K}_{13}^1 & \boldsymbol{K}_{14}^1 \\ \boldsymbol{K}_{21}^1 & \boldsymbol{K}_{22}^1 & \boldsymbol{K}_{23}^1 & \boldsymbol{K}_{24}^1 \\ \boldsymbol{K}_{31}^1 & \boldsymbol{K}_{32}^1 & \boldsymbol{K}_{33}^1 & \boldsymbol{K}_{34}^1 \\ \boldsymbol{K}_{41}^1 & \boldsymbol{K}_{42}^1 & \boldsymbol{K}_{43}^1 & \boldsymbol{K}_{44}^1 \end{bmatrix} \begin{bmatrix} \boldsymbol{U}_1^1 \\ \boldsymbol{U}_2^1 \\ \boldsymbol{U}_3^1 \\ \boldsymbol{U}_4^1 \end{bmatrix} = \begin{bmatrix} \boldsymbol{F}_1^1 - \boldsymbol{K}_{12}^1 \Delta \boldsymbol{U}_2^1 - \boldsymbol{K}_{13}^1 \Delta \boldsymbol{U}_3^1 \\ \boldsymbol{F}_2^1 - \boldsymbol{K}_{22}^1 \Delta \boldsymbol{U}_2^1 - \boldsymbol{K}_{23}^1 \Delta \boldsymbol{U}_3^1 \\ \boldsymbol{F}_3^1 - \boldsymbol{K}_{32}^1 \Delta \boldsymbol{U}_2^1 - \boldsymbol{K}_{33}^1 \Delta \boldsymbol{U}_3^1 \\ \boldsymbol{F}_4^1 - \boldsymbol{K}_{42}^1 \Delta \boldsymbol{U}_2^1 - \boldsymbol{K}_{43}^1 \Delta \boldsymbol{U}_3^1 \end{bmatrix}, \tag{2.59}$$

where $\boldsymbol{K}$, $\boldsymbol{U}$, and $\boldsymbol{F}$ denote the 2×2 conversion matrix, the 2×1 displacement vector, and the 2×1 force vector, respectively. The local stiffness equation for the second element is given by

$$\begin{bmatrix} \boldsymbol{K}_{11}^2 & \boldsymbol{K}_{12}^2 & \boldsymbol{K}_{13}^2 & \boldsymbol{K}_{14}^2 \\ \boldsymbol{K}_{21}^2 & \boldsymbol{K}_{22}^2 & \boldsymbol{K}_{23}^2 & \boldsymbol{K}_{24}^2 \\ \boldsymbol{K}_{31}^2 & \boldsymbol{K}_{32}^2 & \boldsymbol{K}_{33}^2 & \boldsymbol{K}_{34}^2 \\ \boldsymbol{K}_{41}^2 & \boldsymbol{K}_{42}^2 & \boldsymbol{K}_{43}^2 & \boldsymbol{K}_{44}^2 \end{bmatrix} \begin{bmatrix} \boldsymbol{U}_1^2 \\ \boldsymbol{U}_2^2 \\ \boldsymbol{U}_3^2 \\ \boldsymbol{U}_4^2 \end{bmatrix} = \begin{bmatrix} \boldsymbol{F}_1^2 - \boldsymbol{K}_{11}^2 \Delta \boldsymbol{U}_1^2 - \boldsymbol{K}_{14}^2 \Delta \boldsymbol{U}_4^2 \\ \boldsymbol{F}_2^2 - \boldsymbol{K}_{21}^2 \Delta \boldsymbol{U}_1^2 - \boldsymbol{K}_{24}^2 \Delta \boldsymbol{U}_4^2 \\ \boldsymbol{F}_3^2 - \boldsymbol{K}_{31}^2 \Delta \boldsymbol{U}_1^2 - \boldsymbol{K}_{34}^2 \Delta \boldsymbol{U}_4^2 \\ \boldsymbol{F}_4^2 - \boldsymbol{K}_{41}^2 \Delta \boldsymbol{U}_1^2 - \boldsymbol{K}_{44}^2 \Delta \boldsymbol{U}_4^2 \end{bmatrix}. \tag{2.60}$$

Here,

$$\begin{cases} \boldsymbol{U}_2^1 = \left\langle \boldsymbol{U}_2^1 \right\rangle + \Delta \boldsymbol{U}_2^1, \quad \boldsymbol{U}_3^1 = \left\langle \boldsymbol{U}_3^1 \right\rangle + \Delta \boldsymbol{U}_3^1 \\ \boldsymbol{U}_1^2 = \left\langle \boldsymbol{U}_1^2 \right\rangle + \Delta \boldsymbol{U}_1^2, \quad \boldsymbol{U}_4^2 = \left\langle \boldsymbol{U}_4^2 \right\rangle + \Delta \boldsymbol{U}_4^2 \end{cases}, \tag{2.61}$$

and the rule for assembly is now

$$\begin{cases} \underline{\boldsymbol{U}}_1 = \boldsymbol{U}_1^1, \quad \underline{\boldsymbol{U}}_2 = \left\langle \boldsymbol{U}_2^1 \right\rangle = \left\langle \boldsymbol{U}_1^2 \right\rangle, \quad \underline{\boldsymbol{U}}_3 = \boldsymbol{U}_2^2 \\ \underline{\boldsymbol{U}}_4 = \boldsymbol{U}_4^1, \quad \underline{\boldsymbol{U}}_5 = \left\langle \boldsymbol{U}_3^1 \right\rangle = \left\langle \boldsymbol{U}_4^2 \right\rangle, \quad \underline{\boldsymbol{U}}_6 = \boldsymbol{U}_3^2 \\ \Delta \boldsymbol{U}_2^1 = -\Delta \boldsymbol{U}_1^2, \quad \Delta \boldsymbol{U}_3^1 = -\Delta \boldsymbol{U}_4^2 \end{cases}. \tag{2.62}$$

Then, the fully assembled stiffness equation becomes

$$\begin{bmatrix} \boldsymbol{K}_{11}^1 & \boldsymbol{K}_{12}^1 & 0 & \boldsymbol{K}_{14}^1 & \boldsymbol{K}_{13}^1 & 0 \\ \boldsymbol{K}_{21}^1 & \boldsymbol{K}_{22}^1 + \boldsymbol{K}_{11}^2 & \boldsymbol{K}_{12}^2 & \boldsymbol{K}_{24}^1 & \boldsymbol{K}_{23}^1 + \boldsymbol{K}_{14}^2 & \boldsymbol{K}_{13}^2 \\ 0 & \boldsymbol{K}_{21}^2 & \boldsymbol{K}_{22}^2 & 0 & \boldsymbol{K}_{24}^2 & \boldsymbol{K}_{23}^2 \\ \boldsymbol{K}_{41}^1 & \boldsymbol{K}_{42}^1 & 0 & \boldsymbol{K}_{44}^1 & \boldsymbol{K}_{43}^1 & 0 \\ \boldsymbol{K}_{31}^1 & \boldsymbol{K}_{32}^1 + \boldsymbol{K}_{41}^2 & \boldsymbol{K}_{42}^2 & \boldsymbol{K}_{34}^1 & \boldsymbol{K}_{33}^1 + \boldsymbol{K}_{44}^2 & \boldsymbol{K}_{43}^2 \\ 0 & \boldsymbol{K}_{31}^2 & \boldsymbol{K}_{32}^2 & 0 & \boldsymbol{K}_{34}^2 & \boldsymbol{K}_{33}^2 \end{bmatrix} \begin{bmatrix} \underline{\boldsymbol{U}}_1 \\ \underline{\boldsymbol{U}}_2 \\ \underline{\boldsymbol{U}}_3 \\ \underline{\boldsymbol{U}}_4 \\ \underline{\boldsymbol{U}}_5 \\ \underline{\boldsymbol{U}}_6 \end{bmatrix}$$

$$
= \begin{bmatrix} \boldsymbol{F}_1^1 - \boldsymbol{K}_{12}^1 \Delta \boldsymbol{U}_2^1 - \boldsymbol{K}_{13}^1 \Delta \boldsymbol{U}_3^1 \\ \boldsymbol{F}_2^1 + \boldsymbol{F}_1^2 - \boldsymbol{K}_{22}^1 \Delta \boldsymbol{U}_2^1 - \boldsymbol{K}_{23}^1 \Delta \boldsymbol{U}_3^1 - \boldsymbol{K}_{11}^2 \Delta \boldsymbol{U}_1^2 - \boldsymbol{K}_{14}^2 \Delta \boldsymbol{U}_4^2 \\ \boldsymbol{F}_2^2 - \boldsymbol{K}_{21}^2 \Delta \boldsymbol{U}_2^2 - \boldsymbol{K}_{24}^2 \Delta \boldsymbol{U}_4^2 \\ \boldsymbol{F}_4^1 - \boldsymbol{K}_{42}^1 \Delta \boldsymbol{U}_2^1 - \boldsymbol{K}_{43}^1 \Delta \boldsymbol{U}_3^1 \\ \boldsymbol{F}_3^1 + \boldsymbol{F}_4^2 - \boldsymbol{K}_{32}^1 \Delta \boldsymbol{U}_2^1 - \boldsymbol{K}_{33}^1 \Delta \boldsymbol{U}_3^1 - \boldsymbol{K}_{41}^2 \Delta \boldsymbol{U}_1^2 - \boldsymbol{K}_{44}^2 \Delta \boldsymbol{U}_4^2 \\ \boldsymbol{F}_3^2 - \boldsymbol{K}_{31}^2 \Delta \boldsymbol{U}_1^2 - \boldsymbol{K}_{34}^2 \Delta \boldsymbol{U}_4^2 \end{bmatrix}. \tag{2.63}
$$

Incorporation of gravity effects into traction free conditions at the Earth's surface

The effect of gravity is essential in the present problem. If we ignore the effect of gravity, the convergent plate motion leads to the uniform uplift of overriding plates and the uniform subsidence of underlying plates (Fukahata & Matsu'ura, 2006). This clearly contradicts the situation in the actual subduction zones. So, we cannot ignore the effects of gravity in finite element modeling. We suppose the gravitational equilibrium is achieved in the initial state. Then, we need to consider only the gravitational disturbance caused by plate subduction.

In most FEM models, the effect of gravity has been considered for all the elements (e.g., Gasperini & Sabadini, 1989; Kaufmann et al., 1997). In the present study, we only consider the gravitational disturbance associated with surface uplift and subsidence. The Earth's surface is the boundary with the largest density contrast, and so its vertical deformation produces the largest effect on gravity disequilibrium (e.g., McConnell, 1965; Matsu'ura & Sato, 1989; Williams & Richardson, 1991).

We consider the vertical normal stress σ_{yy}. The vertical normal stress caused by the vertical displacement v on the Earth's surface ($y = 0$) is given by $\rho g v$; that is,

$$
\sigma_{yy}\left(y=0\right) = -\rho g v . \tag{2.64}
$$

The effect of gravity due to crustal deformation is easily incorporated into the FEM

model by a simple rearrangement of the stiffness equation. Now we consider the 2-elements and 6-nodes system. In Fig. 3 we schematically explain how to incorporate the effects of negative and positive buoyancy due to surface uplift and subsidence into traction free conditions at the Earth's surface. The line segment between the forth and sixth nodes constitutes the Earth's surface. Denoting the horizontal lengths of the two adjacent elements by l_1 and l_2, the net gravity force produced by the vertical displacement u_y is $-\rho g v(l_1/2)$ for the forth end node, $-\rho g v(l_1+l_2)/2$ for the firth center node, and $-\rho g v(l_2/2)$ for the sixth end node. Therefore, except end nodes, the effect of gravity due to the surface deformation is given by $f_y = -\rho g \bar{l} v$ with $\bar{l} = (l_1+l_2)/2$, and the stiffness equation for the element 1 can be written as

$$\begin{bmatrix} \boldsymbol{K}_{11}^1 & \boldsymbol{K}_{12}^1 & \boldsymbol{K}_{13}^1 & \boldsymbol{K}_{14}^1 \\ \boldsymbol{K}_{21}^1 & \boldsymbol{K}_{22}^1 & \boldsymbol{K}_{23}^1 & \boldsymbol{K}_{24}^1 \\ \boldsymbol{K}_{31}^1 & \boldsymbol{K}_{32}^1 & \boldsymbol{K}_{33}^1 & \boldsymbol{K}_{34}^1 \\ \boldsymbol{K}_{41}^1 & \boldsymbol{K}_{42}^1 & \boldsymbol{K}_{43}^1 & \boldsymbol{K}_{44}^1 \end{bmatrix} \begin{bmatrix} \boldsymbol{U}_1^1 \\ \boldsymbol{U}_2^1 \\ \boldsymbol{U}_3^1 \\ \boldsymbol{U}_4^1 \end{bmatrix} = \begin{bmatrix} \boldsymbol{F}_1^1 \\ \boldsymbol{F}_2^1 \\ \boldsymbol{F}_3^1 \\ \boldsymbol{F}_4^1 \end{bmatrix} - \begin{bmatrix} 0 & 0 & 0 & 0 \\ 0 & 0 & 0 & 0 \\ 0 & 0 & \boldsymbol{K}_{33}'^1 & 0 \\ 0 & 0 & 0 & \boldsymbol{K}_{44}'^1 \end{bmatrix} \begin{bmatrix} \boldsymbol{U}_1^1 \\ \boldsymbol{U}_2^1 \\ \boldsymbol{U}_3^1 \\ \boldsymbol{U}_4^1 \end{bmatrix} \tag{2.65}$$

with

$$\boldsymbol{K}_{33}'^1 = \begin{bmatrix} 0 & 0 \\ 0 & \rho g l_1/2 \end{bmatrix}, \quad \boldsymbol{K}_{44}'^1 = \begin{bmatrix} 0 & 0 \\ 0 & \rho g l_1/2 \end{bmatrix}. \tag{2.66}$$

We can rewrite the above equation as

$$\begin{bmatrix} \boldsymbol{K}_{11}^1 & \boldsymbol{K}_{12}^1 & \boldsymbol{K}_{13}^1 & \boldsymbol{K}_{14}^1 \\ \boldsymbol{K}_{21}^1 & \boldsymbol{K}_{22}^1 & \boldsymbol{K}_{23}^1 & \boldsymbol{K}_{24}^1 \\ \boldsymbol{K}_{31}^1 & \boldsymbol{K}_{32}^1 & \boldsymbol{K}_{33}^1 + \boldsymbol{K}_{33}'^1 & \boldsymbol{K}_{34}^1 \\ \boldsymbol{K}_{41}^1 & \boldsymbol{K}_{42}^1 & \boldsymbol{K}_{43}^1 & \boldsymbol{K}_{44}^1 + \boldsymbol{K}_{44}'^1 \end{bmatrix} \begin{bmatrix} \boldsymbol{U}_1^1 \\ \boldsymbol{U}_2^1 \\ \boldsymbol{U}_3^1 \\ \boldsymbol{U}_4^1 \end{bmatrix} = \begin{bmatrix} \boldsymbol{F}_1^1 \\ \boldsymbol{F}_2^1 \\ \boldsymbol{F}_3^1 \\ \boldsymbol{F}_4^1 \end{bmatrix}. \tag{2.67}$$

In a similar way, we obtain the stiffness equation for the element 2 as

$$\begin{bmatrix} \boldsymbol{K}_{11}^2 & \boldsymbol{K}_{12}^2 & \boldsymbol{K}_{13}^2 & \boldsymbol{K}_{14}^2 \\ \boldsymbol{K}_{21}^2 & \boldsymbol{K}_{22}^2 & \boldsymbol{K}_{23}^2 & \boldsymbol{K}_{24}^2 \\ \boldsymbol{K}_{31}^2 & \boldsymbol{K}_{32}^2 & \boldsymbol{K}_{33}^2 + \boldsymbol{K}_{33}'^2 & \boldsymbol{K}_{34}^2 \\ \boldsymbol{K}_{41}^2 & \boldsymbol{K}_{42}^2 & \boldsymbol{K}_{43}^2 & \boldsymbol{K}_{44}^2 + \boldsymbol{K}_{44}'^2 \end{bmatrix} \begin{bmatrix} \boldsymbol{U}_1^2 \\ \boldsymbol{U}_2^2 \\ \boldsymbol{U}_3^2 \\ \boldsymbol{U}_4^2 \end{bmatrix} = \begin{bmatrix} \boldsymbol{F}_1^2 \\ \boldsymbol{F}_2^2 \\ \boldsymbol{F}_3^2 \\ \boldsymbol{F}_4^2 \end{bmatrix}, \tag{2.68}$$

with

$$\boldsymbol{K}'^{2}_{33} = \begin{bmatrix} 0 & 0 \\ 0 & \rho g l_2 / 2 \end{bmatrix}, \quad \boldsymbol{K}'^{2}_{44} = \begin{bmatrix} 0 & 0 \\ 0 & \rho g l_2 / 2 \end{bmatrix}. \tag{2.69}$$

The rule for assembly is now

$$\begin{cases} \underline{\boldsymbol{U}}_1 = \boldsymbol{U}^1_1, & \underline{\boldsymbol{U}}_2 = \boldsymbol{U}^1_2 = \boldsymbol{U}^2_1, & \underline{\boldsymbol{U}}_3 = \boldsymbol{U}^2_2 \\ \underline{\boldsymbol{U}}_4 = \boldsymbol{U}^1_4, & \underline{\boldsymbol{U}}_5 = \boldsymbol{U}^1_3 = \boldsymbol{U}^2_4, & \underline{\boldsymbol{U}}_6 = \boldsymbol{U}^2_3 \end{cases}, \tag{2.70}$$

and so the fully assembled stiffness equation becomes

$$\begin{bmatrix} \boldsymbol{K}^1_{11} & \boldsymbol{K}^1_{12} & 0 & \boldsymbol{K}^1_{14} & \boldsymbol{K}^1_{13} & 0 \\ \boldsymbol{K}^1_{21} & \boldsymbol{K}^1_{22} + \boldsymbol{K}^2_{11} & \boldsymbol{K}^2_{12} & \boldsymbol{K}^1_{24} & \boldsymbol{K}^1_{23} + \boldsymbol{K}^2_{14} & \boldsymbol{K}^2_{13} \\ 0 & \boldsymbol{K}^2_{21} & \boldsymbol{K}^2_{22} & 0 & \boldsymbol{K}^2_{24} & \boldsymbol{K}^2_{23} \\ \boldsymbol{K}^1_{41} & \boldsymbol{K}^1_{42} & 0 & \boldsymbol{K}^1_{44} + \boldsymbol{K}'^1_{44} & \boldsymbol{K}^1_{43} & 0 \\ \boldsymbol{K}^1_{31} & \boldsymbol{K}^1_{32} + \boldsymbol{K}^2_{41} & \boldsymbol{K}^2_{42} & \boldsymbol{K}^1_{34} & \boldsymbol{K}^1_{33} + \boldsymbol{K}'^1_{33} + \boldsymbol{K}^2_{44} + \boldsymbol{K}'^2_{44} & \boldsymbol{K}^2_{43} \\ 0 & \boldsymbol{K}^2_{31} & \boldsymbol{K}^2_{32} & 0 & \boldsymbol{K}^2_{34} & \boldsymbol{K}^2_{33} + \boldsymbol{K}'^2_{33} \end{bmatrix} \begin{bmatrix} \underline{\boldsymbol{U}}_1 \\ \underline{\boldsymbol{U}}_2 \\ \underline{\boldsymbol{U}}_3 \\ \underline{\boldsymbol{U}}_4 \\ \underline{\boldsymbol{U}}_5 \\ \underline{\boldsymbol{U}}_6 \end{bmatrix} = \begin{bmatrix} \boldsymbol{F}^1_1 \\ \boldsymbol{F}^1_2 + \boldsymbol{F}^2_1 \\ \boldsymbol{F}^2_2 \\ \boldsymbol{F}^1_4 \\ \boldsymbol{F}^1_3 + \boldsymbol{F}^2_4 \\ \boldsymbol{F}^2_3 \end{bmatrix} \tag{2.71}$$

with

$$\boldsymbol{K}'^{1}_{33} + \boldsymbol{K}'^{2}_{44} = \begin{bmatrix} 0 & 0 \\ 0 & \rho g \left(l_1 + l_2 \right) / 2 \end{bmatrix} = \begin{bmatrix} 0 & 0 \\ 0 & \rho g \bar{l} \end{bmatrix} \tag{2.72}$$

Introducing a special matrix defined by

$$\boldsymbol{E}_{ij} = \begin{cases} \delta_{ij} & \text{if } i = j = 2n \\ 0 & \text{otherwise} \end{cases}, \tag{2.73}$$

we can represent the effect of gravity as

$$\boldsymbol{F}' = -\rho g \bar{l} \boldsymbol{E} \boldsymbol{U} = -\boldsymbol{K}' \boldsymbol{U} . \tag{2.74}$$

Here, n denotes the node point located at the Earth's surface, $2n$ denotes the effect of gravity related to the vertical (y) displacement and force, and $\boldsymbol{K}'$ denotes a diagonal matrix whose nonzero elements are the individual gravity forces. Then, Eq. (2.45) is modified as

$$(\boldsymbol{K}+\boldsymbol{K}')\boldsymbol{U}=\boldsymbol{F}\ . \tag{2.75}$$

The Selective-Reduced Integration scheme to avoid volumetric locking

As shown in Section 2.1, long-term deformation rates due to steady plate subduction can be obtained from the associated elastic solution by taking the rigidity of the medium corresponding the viscoelastic asthenosphere to be zero. When the rigidity approaches zero, the Poisson's ratio approaches 0.5. In numerical computation, this is equivalent to imposing incompressibility condition ($div\boldsymbol{u}=0$) on each element. Then, the "volumetric locking" occurs. Under the incompressibility condition, equivalent stiffness of each element increases. Therefore, the displacements of nodes remain fixed in order to maintain the volume.

As an example, preliminary computations of beam bending were conducted. In Fig. 4 we show the geometry and boundary conditions of the problem. The $100\,\mathrm{m}\times 10\,\mathrm{m}$ rectangular beam is divided into 100×10 elements. At X = 0 m, the fixed boundary condition, $u=v=0$, is applied. The upper and bottom boundaries are free (the traction free condition $\boldsymbol{t}=\boldsymbol{0}$ is imposed). At X = 100 m, a downward force F_y (3.0×10^3 N) is applied. As for the elastic constant, bulk modulus κ is set to be 50.0 GPa, which is the same as that in the series of computations. In order to investigate the behavior of FEM solution, we change the rigidity μ from 50 GPa to 0.5 MPa.

The results of computation are shown in Fig. 5(a) together with the analytical solution. The analytical solution (vertical displacement v) of beam bending is given by

$$v=\frac{3K+4\mu}{\mu\left(3K+\mu\right)}\frac{F_yL^3}{h^3}+\frac{6F_yL}{5\mu h^2} \tag{2.76}$$

Here, L and h are horizontal and vertical length of the beam, respectively. From Fig.

5(a) we can see that the numerical solutions with the full integration scheme differ from analytical solutions as the shear modulus μ approaches 0.

Various types of numerical methods have been developed for solving the problems of volumetric locking. One of the methods is the reduced integration scheme, where we reduce integration point to evaluate strain in an element. For example, numerical integration in each isoparametric bilinear quadrilateral element is usually carried out with four Gaussian quadrature points. Fig. 6 (a) shows the four Gaussian quadrature points in the local coordinate system in the full integration scheme. In the reduced integration scheme, numerical integration is done at one point, located at the center of the element, as shown in Fig. 6 (b). However, in the reduced integration scheme, accuracy is generally worse. Accordingly, there arises the deformation mode called "spurious zero energy mode".

As remedies of these types of problems, the Selective-Reduced Integrations (SRI) schemes have been developed, where reduced integration is applied to only selected terms. We use the SRI scheme by Hughes (1980), where the number of Gaussian quadrature points is reduced only for mean normal stress, and that for deviatoric stress is the same as in the full integration, as shown in Fig. 6 (c). In the following part of this subsection, we briefly explain the formulation of SRI scheme. The main problem in volumetric locking lies in the determination of the mean normal stress related to the volumetric strain. So, it is reasonable to treat the isotropic part and the deviatoric part separately. First, we divide the elasticity matrix $\boldsymbol{D}$ in Eq. (2.30) into the volumetric part $\boldsymbol{D}_V$ and the deviatoric part $\boldsymbol{D}_D$: that is,

$$\boldsymbol{D} = \boldsymbol{D}_V + \boldsymbol{D}_D \tag{2.77}$$

with

$$\boldsymbol{D}_V = \begin{bmatrix} \kappa & \kappa & 0 \\ \kappa & \kappa & 0 \\ 0 & 0 & 0 \end{bmatrix}, \quad \boldsymbol{D}_D = \begin{bmatrix} 4\mu/3 & -2\mu/3 & 0 \\ -2\mu/3 & +4\mu/3 & 0 \\ 0 & 0 & \mu \end{bmatrix}. \tag{2.78}$$

The corresponding element stiffness matrix in Eq. (2.51) is written as

$$\boldsymbol{K}^e_{\alpha\beta} = \sum_{p=1}^{4} \left[\boldsymbol{B}^T_\alpha \boldsymbol{D} \boldsymbol{B}_\beta J \right]_{\substack{\xi=\xi_p \\ \eta=\eta_p}} = \sum_{p=1}^{4} \left[\boldsymbol{B}^T_\alpha \boldsymbol{D}_V \boldsymbol{B}_\beta J \right]_{\substack{\xi=\xi_p \\ \eta=\eta_p}} + \sum_{p=1}^{4} \left[\boldsymbol{B}^T_\alpha \boldsymbol{D}_D \boldsymbol{B}_\beta J \right]_{\substack{\xi=\xi_p \\ \eta=\eta_p}} . \tag{2.79}$$

In the SRI scheme, the volumetric strain or mean normal stress is evaluated in the center of the element; that is, we take the location of integration points for the volumetric part (the first term on the right hand side of the above equation) as (0,0) instead of (ξ_p, η_p) defined in Eq. (2.52). The deviatoric part (the second term) is evaluated through the full integration scheme at the four Gaussian quadrature points, as shown in Fig. 6 (c). Namely, in the SRI scheme, the element stiffness matrix is evaluated as

$$\boldsymbol{K}^e_{\alpha\beta} = \left[\boldsymbol{B}^T_\alpha \boldsymbol{D}_V \boldsymbol{B}_\beta J \right]_{\substack{\xi=0 \\ \eta=0}} + \sum_{p=1}^{4} \left[\boldsymbol{B}^T_\alpha \boldsymbol{D}_D \boldsymbol{B}_\beta J \right]_{\substack{\xi=\xi_p \\ \eta=\eta_p}} . \tag{2.80}$$

From Fig. 5 (b) we can see the numerical solutions with the SRI scheme are consistent with analytical solutions as the shear modulus μ approaches 0.

2.3 Model setting and numerical results

With the mechanical FEM model developed in Section 2.2 we compute the long-term internal velocity fields due to steady plate subduction. First, in order to test the validity of this model, we compute the internal velocity fields for a horizontally layered structure model and compare them with those based on the analytical expressions by Fukahata & Matsu'ura (2006). Next, we examine the effects of elastic plate thickness on the internal velocity fields; especially on surface uplift rates, through the comparison of

the numerical results for various descending slab models with different elastic plate thickness.

Model setting for numerical computation

The model setting for numerical computation is as follows. We took a 2000 km (horizontal)$\times$500 km (vertical) fine-mesh model region composed of 800$\times$500 elements as shown in Fig. 7, where the thick solid line indicates the split nodes to represent the tangential displacement discontinuity (fault slip) at the plate interface. In order to suppress boundary echoes we added a broad coarse-mesh region surrounding the fine-mesh model region. The right side of the total model region is set to be horizontally fixed but vertically free. The base is set to be vertically fixed but horizontally free. The left side is set to be free both for horizontal and vertical displacements. Then, the computed results represent velocity fields relative to a remote reference point fixed on the continental plate. Note that the traction free conditions, $\sigma_{xy} = \sigma_{yy} = 0$, at the upper surface is modified as $\sigma_{xy} = 0$ and $\sigma_{yy} + \rho g v = 0$ to incorporate the negative and positive buoyancy effects related to surface uplift and subsidence. The values of bulk modulus and rigidity for each medium used for numerical computation are given in Tables 1 and 2. It should be noted that the rigidity μ^v of the substratum corresponding to the asthenosphere is taken to be very small (1/10,000) in comparison with that of the elastic plate.

The results of numerical computation

With the mechanical FEM model we compute the long-term internal velocity fields due to steady plate subduction. First, in order to compare with the results based on the

analytical expressions by Fukahata & Matsu'ura (2006), we consider the case of a horizontally layered structure. We took the thickness of the elastic surface layer to be 35 km, and its density and rigidity to be 2.6×10^3 kg/m^3 and 33.2 GPa, respectively (Table 1). The computed velocity fields due to steady plate subduction at 10 mm/yr are shown in Fig. 8, where the red lines indicate the surface velocities computed by the FEM model and the green lines indicate those computed by Fukahata & Matsu'ura (2006). From comparison of these results we can see that the long-term internal deformation fields calculated from the FEM model almost completely agree with those based on analytical expressions by Fukahata & Matsu'ura (2006).

Next, we compute the internal velocity field when the oceanic plate is descending into the asthenosphere as shown in Fig. 7. In this case the descending oceanic plate reaches the 150 km depth. We took the thickness of the descending oceanic plate (L_s) and the overriding continental plate (L_o) to be the same standard value of 50 km. The density and rigidity of the elastic plates are taken to be 2.6×10^3 kg/m^3 and 32 GPa, respectively (Table 2). In Fig. 9 we show the computed internal velocity fields. From comparison of the surface velocity patterns for the descending slab model (red lines) with those for the horizontally layered model (green lines), we can see the following. For the horizontal velocity pattern, we cannot find any difference between these two models. For the vertical velocity pattern, the gross features are similar, but the maximum uplift rates on the overriding plate are significantly different; the maximum uplift rate for the slab descending model is about 40 % faster than that for the horizontally layered model. This difference comes from difference in substantial stiffness between the totally descending slab (the descending slab model) and the partly descending slab (the horizontally layered model).

Now we examine the effects of the thickness of descending oceanic plates on the surface velocity patterns. In this case, fixing the thickness of the overriding plate (L_o) to the standard value (50 km), we changed the thickness of descending oceanic plates (L_s) as 30, 50 and 80 km. The computed surface velocity patterns are shown in Fig. 10. From this figure we can see that the horizontal velocity pattern (the upper panel) scarcely depends on L_s. On the other hand, the dependence of the vertical velocity pattern (the lower panel) on L_s is significant. When the descending oceanic plate becomes thicker, the subsidence zone around the plate boundary broader, and the uplift rate and the subsidence rate become faster. Such a tendency can be explained by the compound effect of the increase in substantial stiffness of the descending plate and the gravitational recovery force to isostasy.

We also examine the effects of the thickness of overriding continental plates on the surface velocity patterns. In this case, fixing the thickness of the descending plate (L_s) to the standard value (50 km), we changed the thickness of overriding plates (L_o) from 20 km to 80 km by 10 km. The computed vertical velocity patterns are shown in Fig. 11. From this figure we can see that the subsidence pattern around the trench scarcely depends on L_o, but the vertical velocity pattern depends on L_o in a complicated way. As the thickness of the overriding plate increases from 20 km to 50 km (the thickness of the descending plate), the uplift zone on the overriding plate moves and expands to the right with decreasing the maximum uplift rate. When the thickness of the overriding plate further increases beyond 50 km, on the other hand, the maximum uplift rate on the overriding plate becomes faster. Such strange behavior in vertical motion can be explained by two reasons. When the thickness of the overriding plate increases, the source area (the directly contact area of the elastic descending and elastic

overriding plates) expands up to the depth of 50 km. This is the first reason. The second reason is similar to the previous case; that is, the compound effect of the increase in substantial stiffness of the overriding plate and the gravitational recovery force to isostasy.

Chapter 3. Development of Mechanical and Thermal Structure in Subduction Zones

In Chapter 2, we developed a mechanical FEM model to compute long-term internal velocity fields due to steady plate subduction for given rheological structure. However, as we mentioned in Chapter 1, the rheological structure in subduction zones develops with time by the effects of thermal diffusion and advection associated with internal deformation due to steady plate subduction. In this chapter, we develop a thermal FEM model to compute internal temperature changes due to thermal diffusion and advection in subduction zones. The temperature changes lead to the change in rheological structure in subduction zones. Then, combining the thermal FEM model with the mechanical FEM model, we construct a simulation system for mechanical-thermal interaction processes, and numerically compute the development of mechanical and thermal structure with time in a plate subduction zone.

3.1 A numerical model for heat transfer with FEM

In the present study we model the diffusion and advection processes in subduction zones in a 2-D framework. The governing equation for heat transfer is given by

$$\rho C \frac{\partial T}{\partial t} + \rho C \left(\dot{u} \frac{\partial T}{\partial x} + \dot{v} \frac{\partial T}{\partial y} \right) - k \left(\frac{\partial^2 T}{\partial x^2} + \frac{\partial^2 T}{\partial y^2} \right) = Q , \tag{3.1}$$

where T is temperature, ρ is density, C is specific heat, $\dot{u}$ is horizontal velocity, $\dot{v}$ is vertical velocity, k is thermal conductivity, and Q is heat generation. The second and third terms on the left-hand side of the above equation represent advection and diffusion, respectively. We describe the conditions to be satisfied on the boundary $\Gamma = \Gamma_T \cup \Gamma_H$

of an objective region Ω as follows. The Dirichlet boundary condition is given by

$$T = \overline{T} \qquad \text{on} \quad \Gamma_T \subset \Gamma \tag{3.2}$$

and the Neumann boundary condition is given by

$$h \equiv \left(T\dot{u} - \chi \frac{\partial T}{\partial x} \right) n_x + \left(T\dot{v} - \chi \frac{\partial T}{\partial y} \right) n_y = \overline{h} \qquad \text{on} \quad \Gamma_H \subset \Gamma \,. \tag{3.3}$$

Here, $\chi = k / \rho C$ denotes thermal diffusivity, n_x and n_y are the x and y components of the unit normal vector of the boundary Γ $(\Gamma_T \cap \Gamma_H = 0)$.

Multiplying the both sides of Eq. (3.1) by arbitrary virtual temperature change δT^* that satisfies $\delta T^* = 0$ on Γ_T, and integrating them over the region Ω, we obtain

$$\int_\Omega \delta T^* \left[\frac{\partial T}{\partial t} + \left(\dot{u} \frac{\partial T}{\partial x} + \dot{v} \frac{\partial T}{\partial y} \right) - \chi \left(\frac{\partial^2 T}{\partial x^2} + \frac{\partial^2 T}{\partial y^2} \right) \right] d\Omega = \int_\Omega \delta T^* q d\Omega \tag{3.4}$$

with

$$q = Q / \rho C \,. \tag{3.5}$$

Applying the Green's theorem to the left hand side of the above equation, and assuming the incompressibility of the medium, $\partial \dot{u} / \partial x + \partial \dot{v} / \partial y = 0$, we obtain

$$\begin{aligned} &\int_\Omega \delta T^* \frac{\partial T}{\partial t} d\Omega - \int_\Omega \left(\frac{\partial \delta T^*}{\partial x} \dot{u} + \frac{\partial \delta T^*}{\partial y} \dot{v} \right) T d\Omega + \int_\Omega \chi \left(\frac{\partial \delta T^*}{\partial x} \frac{\partial \delta T}{\partial x} + \frac{\partial \delta T^*}{\partial y} \frac{\partial \delta T}{\partial y} \right) d\Omega \\ &= -\int_{\Gamma_H} \delta T^* \overline{h} d\Gamma + \int_\Omega \delta T^* q \, d\Omega \end{aligned} \tag{3.6}$$

In a similar way to the case of the mechanical FEM model, we approximate the temperature, the virtual temperature change, and the horizontal and vertical velocities in the quadrilateral element by using the interpolation functions $N_i(x, y)$ as

$$T(x,y)=\sum_{i=1}^{4}N_i(x,y)T_i \tag{3.7}$$

$$\delta T^*(x,y)=\sum_{i=1}^{4}N_i(x,y)\delta T_i^* \tag{3.8}$$

and

$$\begin{cases}\dot{u}(x,y)=\sum_{i=1}^{4}N_i\left(x,y\right)\dot{u}_i \\ \dot{v}(x,y)=\sum_{i=1}^{4}N_i\left(x,y\right)\dot{v}_i\end{cases}. \tag{3.9}$$

Here, T_i and δT_i^* are the nodal temperature and the arbitrary nodal temperature change, respectively, and $\dot{u}_i$ and $\dot{v}_i$ are the nodal horizontal and vertical velocities, respectively. Then, we obtain the approximate representation of Eq. (3.6) as

$$\begin{aligned}&\delta T_\alpha^*\left(\int_\Omega N_\alpha N_\beta d\Omega\right)\frac{\partial T_\beta}{\partial t}-\delta T_\alpha^*\left(\dot{u}_\beta\int_\Omega\frac{\partial N_\alpha}{\partial x}N_\beta N_\gamma d\Omega+\dot{v}_\beta\int_\Omega\frac{\partial N_\alpha}{\partial y}N_\beta N_\gamma d\Omega\right)T_\gamma \\ &+\delta T_\alpha^*\left(\int_\Omega\chi\frac{\partial N_\alpha}{\partial x}\frac{\partial N_\beta}{\partial x}d\Omega+\int_\Omega\chi\frac{\partial N_\alpha}{\partial y}\frac{\partial N_\beta}{\partial y}d\Omega\right)T_\beta \\ &=-\delta T_\alpha^*\left(\int_{\Gamma_H}N_\alpha\bar{h}d\Gamma\right)+\delta T_\alpha^*\left(\int_\Omega N_\alpha q\,d\Omega\right)\end{aligned}. \tag{3.10}$$

Here, the repetition of subscript, α and β, in a term denotes a summation with respect to that subscript over its range $(\alpha,\beta=1,...,4)$. From Eq. (3.10), since δT_α^* is arbitrary nodal temperature change, we obtain the heat transfer equation for each element as

$$M_{\alpha\beta}\frac{\partial T_\beta}{\partial t}+(B_{\alpha\beta}+S_{\alpha\beta})T_\beta=\bar{H}_\alpha \qquad (\alpha=1,...4) \tag{3.11}$$

where $M_{\alpha\beta}$, $B_{\alpha\beta}$, $S_{\alpha\beta}$ and $\bar{H}_\alpha$ are the 4×4 heat capacity matrix, the 4×4 heat advection matrix, the 4×4 heat conduction matrix and the 4×1 heat flux vector,

which are defined by

$$M_{\alpha\beta} = \int_{\Omega} N_{\alpha} N_{\beta} d\Omega \tag{3.12}$$

$$B_{\alpha\beta} = \dot{u}_{\gamma} \int_{\Omega} \frac{\partial N_{\alpha}}{\partial x} N_{\beta} N_{\gamma} d\Omega + \dot{v}_{\gamma} \int_{\Omega} \frac{\partial N_{\alpha}}{\partial y} N_{\beta} N_{\gamma} d\Omega \tag{3.13}$$

$$S_{\alpha\beta} = \int_{\Omega} \chi \frac{\partial N_{\alpha}}{\partial x} \frac{\partial N_{\beta}}{\partial x} d\Omega + \int_{\Omega} \chi \frac{\partial N_{\alpha}}{\partial y} \frac{\partial N_{\beta}}{\partial y} d\Omega \tag{3.14}$$

and

$$\bar{H}_{\alpha} = \int_{\Gamma_H} N_{\alpha} \bar{h} d\Gamma + \int_{\Omega} N_{\alpha} q \, d\Omega \,. \tag{3.15}$$

Constructing the heat transfer equation (3.11) for all nodes and superposing them, we obtain the global equation.

Integrating Eq. (3.11) with respect to time t, we can obtain the time-dependent temperature fields. For the time integration we use the explicit method:

$$M_{\alpha\beta} T_{\beta}^{n+1} = \left[M_{\alpha\beta} + (B_{\alpha\beta} + S_{\alpha\beta}) \Delta t \right] T_{\beta}^{n} + \bar{H}_{\alpha}^{n} \Delta t \,, \tag{3.16}$$

where T_{β}^{n} denotes the temperature at the time step n.

3.2 Development of thermal structure under a constant velocity field

Now we simulate the time development of thermal structure due to plate subduction using the thermal FEM model constructed in Section 3.1. In the numerical simulation, we take a model region to be 2000 km (horizontal) $\times$ 500 km (vertical), which is the same as the fine-mesh region of the mechanical FEM model in Chapter 2. The model region is divided into 300×500 elements in the computation of thermal structure, while it was divided into 800×500 elements in the computation of mechanical deformation. The split nodes, which represent the plate interface, are located at the 100th node point from the left boundary. Another difference in the model region

between the mechanical and the thermal problems is the broad coarse-mesh region surrounding the fine-mesh model region. In the thermal problem, we do not put the broad coarse-mesh region surrounding the fine-mesh model region, because the temperature field in the broad coarse-mesh region hardly affects that in the fine-mesh model region.

As shown in Section 2.3, the velocity field, which corresponds to the advective terms $\dot{u}$ and $\dot{v}$ in the thermal conduction equation (3.1), strongly depends on the rheological structure, such as the thickness of the lithosphere. So, in obtaining the velocity field, we first have to specify the boundary between the lithosphere and asthenosphere, which should be primarily controlled by temperature. Based on the estimates of the effective elastic thickness with a thermal and a thin elastic plate model, Courtney & Beaumont (1983) have obtained the relation of viscosity η to temperature T as

$$\eta = \eta_m \exp\left[\frac{Q_{act}}{R}\left(\frac{1}{T} - \frac{1}{T_m}\right)\right]. \tag{3.17}$$

Here, Q_{act} denotes the activation energy for creep, R the gas constant, T_m the temperature at a reference depth, and η_m the viscosity at the temperature T_m. As shown in Eq. (3.17), the rheological property continuously changes with temperature, but we consider only two rheological properties, elastic lithosphere and viscoelastic asthenosphere, for simplicity. Based on Eq. (3.17), we take the boundary between the lithosphere and asthenosphere to be $700\,°\mathrm{C}$, which corresponds to the viscosity of 5.0×10^{22} Pa s, when we use the following values: R = 8.31 J K^{-1}mol^{-1}, T_m = $1200\,°\mathrm{C}$, Q_{act} = 170 kJ/mol, and η_m = 4.0×10^{19} Pa s.

The temperature field at the initial condition ($t = 0$) is shown in Fig. 12, where

the thermal structure is represented with the color scale put in the right bottom. The isotherms are also shown by the green lines every $200\,°\mathrm{C}$. The lithosphere-asthenosphere boundary, which corresponds to the isotherm of $700\,°\mathrm{C}$, is represented by the blue line. The temperature at the Earth's surface is taken to be $0\,°\mathrm{C}$. In the footwall, the temperature increases with depth at a constant rate of $12\,°\mathrm{C/km}$ until the depth of 100 km, where the temperature is $1200\,°\mathrm{C}$. In the hanging wall, the temperature increases with depth at a constant rate of $17.1\,°\mathrm{C/km}$ until 70 km, where the temperature is $1200\,°\mathrm{C}$. Below 100 km in the footwall and 70 km in the hanging wall, the temperature is constant at $1200\,°\mathrm{C}$. In the boundary zone between the footwall and the hanging wall, the temperature is smoothly connected. The boundary conditions of temperature after $t > 0$ are taken to be the same as the initial conditions.

Under this rheological structure, by giving the steady slip at a plate convergence rate $V_{pl} = 5$ cm/yr on the plate interface, we obtain the velocity field as shown in Fig. 13. Using this velocity field, we simulate the development of thermal structure in the following. Actually, the velocity field in Fig. 13 changes with time, because it depends on the rheological structure determined by the temperature field. In this section, however, we only investigate the time development of thermal structure under the given velocity field, before examining the effect of non-linear interaction between crustal deformation and thermal structure. In the numerical simulation of thermal structure development we use the following values: thermal conductivity k to be 3.0 W $\mathrm{K^{-1}\,m^{-1}}$, density ρ to be 3.26×10^3 $\mathrm{kg/m^3}$, and specific heat C to be 1.25×10^3 J $\mathrm{K^{-1}\,kg^{-1}}$. The time step of computation is taken to be 100 years. Through the computation we assume that the surface erosion (sedimentation) rates are equal to the surface uplift (subsidence) rates everywhere.

We direct our attention to temperature changes for the first 5 Myr after the initiation of plate subduction, because the crustal deformation is expected to be the most active in this period (Sato & Matsu'ura, 1993). The result of numerical simulation is shown in Fig. 14. The most conspicuous feature in the evolution of thermal structure in subduction zones is, of course, cooling by the descending oceanic slab. As seen in Fig. 14, the temperature in and around the descending slab rapidly decreases with time. The subduction of cold oceanic slab, however, hardly affects the inland temperature field even at t = 5 Myr. This result is reasonable, because the effective distance $L \simeq \sqrt{\chi t}$ of thermal conduction in the Earth's lithosphere is only about 13 km for $t = 5$ Myr, which is much shorter than the characteristic width (≈ 300 km) of island arc-trench systems.

Another remarkable feature in the thermal evolution process (Fig. 14) is the increase of temperature beneath the arc due to the duration of active uplift and erosion (Fukahata & Matsu'ura, 2000). Because of that, for example, the isotherm of 200°C comes to very close to the Earth's surface at t = 5 Myr. The isotherm of 700°C, the lithosphere-asthenosphere boundary, is also uplifted from 41 to 28 km during 5 Myr. The uplift rate of isotherm is about 2.6 mm/yr, which is nearly the same as the crustal uplift rate (3 mm/yr). The increase of temperature must change the velocity field through the change of the rheological structure, which is the problem of the next section.

3.3 Mechanical-thermal coupled simulation

In Section 3.2, we simulated the development of thermal structure under a given constant velocity field irrespective of the change of thermal structure. Actually, the

velocity field changes if the temperature field changes, because the rheological structure depends on the temperature field. In this section, considering the change in rheological structure due to the development of thermal structure, we simulate the mechanical-thermal interaction process in plate subduction zones.

In the mechanical-thermal interaction model we compute the velocity field and thermal structure in the following procedure: 1) from the $700\,°\mathrm{C}$ isotherm of the initial temperature field, determine the geometry of the lithosphere-asthenosphere boundary, 2) for given rheological structure, compute the internal velocity field with the mechanical FEM model, 3) for given velocity field, compute the next-step temperature field with the thermal FEM model. The above procedure successively iterates. In the actual numerical simulation, we take the time step of the computation for thermal structure to be 10^2 yr, while for deformation field to be 5×10^4 yr. From a theoretical point of view, the effective distance $L \simeq \sqrt{\chi t}$ of thermal conduction for 5×10^4 yr is only about 1 km. This distance is much shorter than the thickness of lithosphere about 50 km. So, the above-mentioned successive iteration procedure is reasonable.

We start the numerical simulation from the initiation of plate subduction. We take the temperature field at t = 0 to be the same as in Fig. 12. The setting for computation, such as the model region and the boundary conditions, is also the same as in the numerical simulations of Section 2.3 and 3.2. With the above-mentioned procedure we numerically simulate the coupled process of deformation field and thermal structure, by giving a steady slip of 5 cm/yr along the plate interface defined by the isotherm of $700\,°\mathrm{C}$. For the purpose of stabilization in computation, the slip rate decreases linearly from 5 cm/yr at $700\,°\mathrm{C}$ to 0 cm/yr at $1200\,°\mathrm{C}$. In Fig. 15 we show the development of thermal structure, deformation field, and uplift rate profile at the

Earth's surface. In the top diagram, the red line shows the uplift rate profile at the Earth's surface. For comparison, we also show the uplift rate profile at the initial condition by the black line. The black arrows in the bottom diagram represent the velocity field.

In Fig. 15 the most irrespective change in the thermal structure, which is the same as in Fig. 14, is cooling by the descending oceanic slab. But in the coupled model, we can see the development of the deformation fields with time. First, cooling by the descending oceanic slab results in the increase of uplift rate in the arc and subsidence rate around the trench (Fig. 15 (b) and (c)). This is the effect of the cold slab on deformation field, as shown in Fig. 9. Fast uplift motion beneath the arc causes the thinning of the arc lithosphere, which results in the localization of the still faster uplift rate in the arc (Fig. 15 (e) and (f)). The downward drag of the asthenosphere near the elastic cold slab is clearly found in this stage.

In order to more clearly see the time development of thermal structure and deformation fields, we summarize the change of the uplift rate profile and the lithosphere-asthenosphere boundary in Fig. 16, where the black, red and blue lines correspond to 0, 2 and 5 Myr after the initiation of subduction, respectively. As shown in Fig. 15, the maximum uplift rate at $t = 0$ was 3.1 mm/yr, while the maximum uplift rate becomes 4.1 mm/yr in 2 Myr and 4.5 mm/yr in 5 Myr. We can also recognize the localization of fast uplift motion in the arc. On the other hand, the change of subsidence rate around the trench is not so significant.

The most important observable quantity in investigating the thermal state in the Earth's interior may be surface heat flow. The surface heat flow is calculated by

$$h = k\frac{\partial T}{\partial y}. \tag{3.18}$$

In Fig. 17 we show the patterns of the spatiotemporal variation of surface heat flow computed from the coupled model at $t = 0$, 1, 3, and 5 Myr from the initiation of plate subduction. Due to the duration of fast uplift and erosion, the heat flow steadily grows up. At 5 Myr the maximum heat flow reaches around 300 mW/m^2, which is five times larger than the one at the initial state. On the other hand, the surface heat flow in the fore-arc is very low due to subsidence and sedimentation. These results mean that the effect of advection overwhelms conduction in heat transfer.

The ratio of advection to conduction in heat transfer can be measured from a dimensionless number, called the Péclet number. The Péclet number is defined as

$$Pe = \frac{\dot{u}L}{\chi}, \tag{3.17}$$

where L is a typical length scale. When we take L to be 70 km, below which the temperature in the arc was constant at the initial state, the Péclet number is about 10 for V_{pl} = 4 cm/yr. In the shallow region, of course, we cannot neglect the effect of conduction, but in the evolution of thermal structure in subduction zones, the effect of advection is primarily important. The cooling by the descending oceanic slab is also the effect of advection essentially.

In Fig. 17 we also show the evolution of heat flow profile calculated from the model with a given constant velocity field in Section 3.2 by the black broken line at $t = 0$, 1, 3, and 5 Myr. Even in the constant velocity model, we can see the rise of surface heat flow in the arc. However, the rise of heat flow is limited and the maximum heat flow only reaches 220 mW/m^2 at 5 Myr, because the acceleration of uplift rate due

to cold slab and thinning of the arc lithosphere is not taken into consideration in the constant velocity model. The difference of the results between the constant velocity model and the mechanical-thermal coupled model indicates that the effect of mechanical-thermal interaction is important for the geomorphic evolution in subduction zones.

Chapter 4. Discussion

In the previous chapters, we developed a mechanical FEM model to compute long-term internal velocity fields due to steady plate subduction and a thermal FEM model to compute temperature changes due to thermal diffusion and advection, and constructed a mechanical-thermal interaction model by combining them to simulate the development of mechanical and thermal structure in a plate subduction zone. In this chapter, we first discuss the applicability and limitation of the models, and next compare the computed results with observed geophysical, geological and geomorphological data in subduction zones.

4.1 Applicability and limitation of the models

In the modeling of actual processes in subduction zones, we have done various simplifications on the basis of the consideration for effective time scales of phenomena. In this section, we make clear the assumptions used for simplification, and discuss the applicability and limitation of the models.

In the computation of internal velocity fields, we assumed complete stress relaxation of the asthenosphere and steady plate subduction at a constant rate. In fact, large interplate earthquakes occur with the recurrence interval of about 10^2 years. The effective stress relaxation time of the asthenosphere is also about 10^2 years. Therefore, the assumptions of completely relaxed asthenosphere and steady plate subduction are valid for the time scale longer than the order of 10^2 yr. As to the lithosphere, we assumed its perfect elasticity. In fact, the viscosity of the lithosphere is not infinity but in the range of 10^{23}-10^{24} Pa s, and so the effects of stress relaxation of the lithosphere,

which decrease vertical deformation rates, become significant after 2-3 Myr. Therefore, the assumption of perfectly elastic lithosphere is valid for the time scale shorter than 2-3 Myr. Furthermore, we assumed no surface erosion and sedimentation in the computation of internal velocity fields. In fact, the long duration of steady uplift and subsidence forms topographic high and low, and the topographic high and low lead to surface erosion and sedimentation, respectively. In the case of $V_{pl} = 5$ cm/yr, for example, the total amount of uplift reaches 2,000 m at the point of maximum uplift rate during the first 1 Myr. Thereafter, we must consider the effects of surface erosion and sedimentation. The process of surface erosion and sedimentation, which is mass transfer from high lands to lowlands, can be regarded as unloading in uplift regions and loading in subsidence regions. So, this surface process will act to somewhat increase vertical deformation rates. Thus, we may conclude that the computed deformation rates in Section 2.3 are valid for the first 1 Myr of plate subduction, slightly small for the time period of the next 2 Myr, and significantly large thereafter.

In the computation of internal temperature changes, on the other hand, we assumed complete surface erosion and sedimentation. This assumption is valid except for the first 1 Myr of plate subduction, but inconsistent with the assumption of no surface erosion and sedimentation in the computation of internal velocity fields. In fact, as mentioned above, we should assume no erosion and sedimentation for the first 1 Myr and complete erosion and sedimentation thereafter. Considering the long-term stress relaxation of the lithosphere together with the reasonable assumption for erosion and sedimentation, we may conclude that the computed surface heat flow in Section 3.3 is slightly large for the first 1 Myr, slightly small for the time period of the next 2 Myr, and significantly large thereafter. In order to resolve this problem we need to combine

the external surface process of erosion and sedimentation with the internal crustal process treated here in numerical simulation. This is a future problem.

4.2 Comparison of the simulation results with observed data

With the mechanical and thermal FEM models we have computed the crustal deformation rates and thermal structure changes due to steady plate subduction. In order to examine the validity of the FEM models, it is a standard way to directly compare the computed results with observations. However, despite the efforts of previous works such as seismic tomography, the clear images of internal velocity and thermal fields in subduction zone have not yet been obtained. So we focus on directly observable geophysical, geological and geomorphological quantities, such as surface uplift/subsidence rate, topographic relief, free-air gravity anomaly and surface heat flow, closely related to the internal velocity and temperature fields. In this section we first review the relationships between these observable quantities, and then discuss the computed results with comparing to the observed geophysical, geological and geomorphological data in several subduction zones.

Relationship between directly observable geo-scientific quantities

Free-air gravity anomaly can be regarded as the manifestation of mass excess/deficit distribution from the isostasy. Therefore, to maintain its stable pattern, some force is required. Since the asthenosphere underlying the elastic plates behaves like a viscous fluid on a long time scale, the force that maintains the stable free-air gravity anomaly pattern must be caused by plate-to-plate mechanical interaction. Sato & Matsu'ura (1993) and Hashimoto & Matsu'ura (2008) demonstrated that free-air gravity anomaly

in subduction zones, characterized by island-arc high, trench low and outer-rise gentle high, reflects the cumulative effects of long-term crustal uplift and subsidence due to steady plate subduction. As shown in Section 2.3, the rate of crustal uplift and subsidence is roughly proportional to the thickness of the descending slab. On the other hand, topographic relief does not necessarily well correlate with free-air gravity anomaly and also surface uplift/subsidence rates. Topographic relief is formed as the result of long-term complex interaction between geophysical and geochemical processes in subduction zones. In other words, surface uplift/subsidence due to steady plate subduction is not only one cause for the development of topographic relief.

Surface heat flow does less correlate with free-air gravity anomaly and also uplift/subsidence rate due to steady plate subduction. It rather correlates with topographic relief, because topographic relief controls surface erosion rate. From the analysis of surface heat flow data in Japan, Fukahata & Matsu'ura (2001) have demonstrated that observed surface heat flow has good correlation with the elevation. Their result is consistent with the assertion of the present study that the effect of uplift/subsidence and erosion/sedimentation is essentially important for thermal structure in subduction zones. However, in order to validate the importance of non-linear interaction between crustal deformation and thermal structure, we need more detailed information on thermal structure from observation. Actually, it is not straightforward to compare the computed thermal structure with observed data. The change of temperature due to steady plate subduction can reach several hundred degrees (Fig. 15). The rise or fall of temperature causes the change of seismic velocity within several percents. However, the crust has large variety in mineral composition, which can cause significant variation of seismic velocity. Therefore, it is difficult to distinguish the

effect of temperature from the result of seismic tomography for the crust. This would be a future problem.

Free-air gravity anomalies in subduction zones

In Fig. 18 (a), we show the free-air gravity anomalies along the Chile trench near the Trench-Trench-Ridge (TTR) triple junction. The sea floor age is also shown in Fig. 18 (b), where we see that the sea floor age in the Nazca plate is progressively older from 0 Ma at the triple junction (46°S) to about 40 Ma in 28°S. The thickness of the elastic plate is proportional to the square root of the elapsed time since the formation of the oceanic crust. Hence, the change of the sea floor age in Fig. 18 (b) can be directly transformed to the change of the thickness of the subducting lithosphere. The other conditions, such as the plate convergence rate and the thickness of the overriding plate, are roughly the same in this region. In Fig. 18 (a) we can see that the amplitude of the free-air gravity anomalies, which are high in the arc, low in the trench, and moderately high in the outer rise, systematically becomes larger from the triple junction to the northward. For example, the negative free-air gravity anomalies at the trench are about 50 mgal in 45°S, 90 mgal in 40°S, and 140 mgal 34°S. On the other hand, the increase of the free-air gravity anomalies to the southward from the triple junction is rather vague, which is consistent with the smaller change of the sea floor age (Fig. 18 (b)).

We can find a similar relation in the subduction zone of Alaska (Fig. 19), where the sea floor age gradually becomes older from northeast to southwest due to the subduction of the Kula plate beneath the North American plate. Corresponding to the change of the sea floor age, the amplitude of gravity anomalies becomes larger from northeast to southwest, which is consistent with the result of this study. To the farther

west in the Aleutian subduction zone, the amplitude of the gravity anomalies is much larger. This would be due to the change of the geometry of plate interface. The deformation field due to plate subduction is very sensitive to the plate interface geometry. The dip angle of the descending plate is much higher in the Aleutian arc than in Alaska (Jarrard, 1986).

We can also recognize the effect of the thickness of subducting plate even in Japan. The plate interface geometry and the plate convergence rates are significantly different between northeastern and southwestern Japan, but Hashimoto et al. (2004) have already computed uplift rates due to plate subduction taking these effects into consideration. In their computation, however, the difference in lithospheric thickness is not taken into account, because they used a boundary element method, not a finite element method, with the analytically obtained Green's function for a stratified medium (Matsu'ura et al., 1981; Fukahata & Matsu'ura, 2005, 2006). Fig. 20 shows the observed (a) and the computed (b) gravity anomalies in and around Japan. The coincidence between the computation and the observation is astonishing. In addition to the characteristic change of gravity anomalies across the subduction zones, the change of them along the arc is also well reproduced. When we compare the computation with the observation both in northeastern and southwestern Japan, however, we notice a systematic difference in their relation. In northeastern Japan, the computation is smaller than the observed data, while in southwestern Japan the computation is smaller than the observation. This systematic difference can be reasonably explained by the effect of the thickness of subducting lithosphere, which has been missed in their theoretical computation.

The effect of the thickness of the overriding plate is complex (Fig. 11). So, it is

not easy to clearly see such effects from observed geoscience data. In Fig. 21, we show the gravity anomaly map in and around the subduction zones of Kuril and Kamchatka, where the sea floor age and the plate convergence rate are nearly the same, and the rough image of the dip of the subducting plate looks similar (Jarrard, 1986; England et al., 2004). However, the thickness of the overriding plate there must be different, because Kamchatka is composed of continental crust, while Kuril is an oceanic island arc. In Fig. 21 we can see the difference in the amplitude of gravity anomalies, which is higher in Kuril than in Kamchatka. The difference may be due to the change of the thickness of the overriding plate. To conclude that, however, we must do numerical computation taking the detailed geometry of plate interface into account, as done by Hashimoto et al. (2004).

Chapter 5. Conclusions

In the present study we revealed the mechanism governing the development of mechanical and thermal structure in plate subduction zones through numerical simulation with a mechanical-thermal interaction model. In the numerical simulation the following points are essential: 1) rational representation of plate-to-plate interaction, 2) realistic modeling of rheological structure, and 3) interaction between mechanical and thermal processes. For the first point, we rationally represented the plate-to-plate interaction by the increase of tangential displacement discontinuity (fault slip) at plate interfaces (Matsu'ura & Sato, 1989). For the second point, we modeled the realistic rheological structure of subduction zones with a finite element method (FEM). As to the third point, we constructed a mechanical-thermal interaction model by combining a thermal FEM model for temperature changes due to thermal diffusion and advection with a mechanical FEM model for internal velocity fields due to plate subduction through a temperature-dependent constitutive equation prescribing rheological properties of materials.

On the basis of the above-mentioned consideration, we developed a mechanical FEM model to compute the long-term internal velocity fields for a simple subduction zone, which is modeled by an elastic continental plate and an elastic oceanic plate descending into an underlying viscoelastic half-space. In order to avoid mathematical difficulty in solving the elastic-viscoelastic boundary value problem in the time domain, we applied the corresponding principle of linear elasticity (Lee, 1955; Radok, 1957) and the equivalent theorem (Fukahata & Matsu'ura, 2006) to the elastic-viscoelastic problem, and reduced it to a simple elastic problem, which is formally obtained from

the original elastic-viscoelastic problem by regarding the underlying viscoelastic half-space as the elastic half-space with the rigidity of zero. Then, we constructed a mechanical model for computing long-term internal velocity fields due to steady plate subduction by applying a standard elastic FEM. In the construction of the mechanical FEM model, we represented the tangential displacement discontinuity at the plate interface with the split node technique (Melosh & Raefsky, 1981). The negative and positive buoyancy effects related to surface uplift and subsidence were incorporated into the stress-free conditions at the Earth's surface (Williams & Richardson, 1991). When we take the rigidity of the underlying elastic half-space to be zero, the computational instability called "volumetric locking" arises. We resolved this computational instability by using the selective-reduced integration scheme (Hughes, 1980).

With the mechanical FEM model we computed the internal velocity fields due to steady plate subduction and obtained the following results. In the case of a horizontally layered model, the long-term internal deformation fields calculated from the FEM model almost completely agree with those from analytical expressions by Fukahata & Matsu'ura (2006). In the case of a descending slab model, the maximum surface uplift rate on the overriding plate is significantly faster than that in the case of the horizontally layered model. If the descending slab is thicker, the uplift zone on the overriding plate and the subsidence zone around the trench become broader, and the uplift and subsidence rates become faster. If the overriding plate is thicker, the subsidence pattern around the trench does not change significantly, but the uplift pattern in the overriding plate changes notably.

Next, we developed the thermal FEM model to compute temperature changes due to thermal diffusion and advection. In the development of the thermal FEM model,

we considered three sources of advection; the subduction of the cold oceanic slab, the mantle flow induced by slab subduction, and the vertical deformation of the overriding plate. With the thermal FEM model we computed temporal change in thermal structure for given internal velocity fields. The computed results show that the third source is less effective in heat transfer, but crucial to understand the mechanism governing the geomorphic development in plate subduction zones.

Finally, combining the thermal FEM model with the mechanical FEM model, we constructed a mechanical-thermal interaction model. In this model the mechanical-thermal interaction is described through a constitutive equation based on the temperature-dependence of the mantle viscosity by Courtney & Beaumont (1983). With the mechanical-thermal interaction model, we numerically simulated the development of mechanical and thermal structure in a plate subduction zone. In this simulation, at a certain time step, we compute internal velocity fields due to plate subduction. Then, using the computed internal velocity fields, we evaluate temperature changes due to thermal diffusion and advection, and update the boundaries between the lithosphere and the asthenosphere to compute internal velocity fields at the next time step. Following such a computation algorithm, we revealed the evolution process of mechanical and thermal structure in the plate subduction zone over a span of 5 Myr. In the early stages of plate subduction (0-2 Myr), the cooling of the mantle wedge leads to the thickening of the continental lithosphere near the plate boundary and increases the uplift rates of the lithosphere beneath the island arc. Then, as time goes on, the thinning of the lithosphere beneath the island arc proceeds and the uplift rates increase further there. This simulation result indicates that the mechanical-thermal interaction is crucial to understand the geomorphic evolution in plate subduction zones.

References

Billen, M. I. and M. Gurnis (2001), A Low Viscosity Wedge in Subduction Zones, *Earth Planet. Sci. Lett.*, 193, 227-236.

Bott, M. H. P., G. D. Waghorn, and A. Whittaker (1989), Plate boundary forces at subduction zones and trench-arc compression, *Tectonophysics*, 170, 1-15.

Burridge, R., and L. Knopoff (1964), Body force equivalents for seismic dislocations, *Bull. Seism. Soc. Am.*, 54, 1875-1888.

Courtney, R. and C. Beaumont (1983), Thermally activated creep and flexure of the oceanic lithosphere, *Nature*, 305, 201-204.

England, P. C., and S. W. Richardson (1977), The influence of erosion upon the mineral facies of rocks from different metamorphic environments, *J. Geol. Soc. London*, 134, 201-213.

England P., R. Engdahl, and W. Thatcher (2004), Systematic variation in the depths of slabs beneath arc volcanoes, *Geophys. J. Int.*, 156, 377-408.

Fukahata, Y., and M. Matsu'ura (2000), Effects of erosion, sedimentation, and accretion on thermal structure in subduction zones, *Geophys. J. Int.*, 141, 271-281.

Fukahata, Y., and M. Matsu'ura (2001), Correlation between surface heat flow and elevation and its geophysical implication, *Geophys. Res. Lett.*, 28, 2703-2706.

Fukahata, Y., and M. Matsu'ura (2005), General expressions for internal deformation fields due to a dislocation source in multilayered half-space, *Geophys. J. Int.*, 161, 507-521.

Fukahata, Y., and M. Matsu'ura (2006), Quasi-static internal deformation due to a dislocation source in a multilayered elastic/viscoelastic half-space and an

equivalence theorem, *Geophys. J. Int.*, 166, 418-434.

Furukawa, Y. (1993), Depth of the decoupling plate interface and thermal structure, *J. Geophys. Res*., 98, 20005-20013.

Gasperini, P., and R. Sabadini (1989), Lateral heterogeneities in mantle viscosity and post-glacial rebound, *Geophys. J.*, 98, 413-428.

Giunchi, C., P. Gasperini, R. Sabadini, and G. D'Agostino (1994), The role of subduction on the horizontal motions in the Tyrrhenian Basin: A numerical model, *Geophys. Res. Lett.*, 21, 529-532.

Giunchi, C., R. Sabadini, E. Boschi, and P. Gasperini (1996), Dynamic models of subduction: geophysical and geological evidence in the Tyrrhenian Sea, *Geophys. J. Int.*, 126, 555-578.

Hasebe, K., N. Fujii, and S. Uyeda (1970), Thermal processes under island arcs, *Tectonophysics,* 10, 335-355.

Hashima, A., Y. Fukahata, and M. Matsu'ura (2008), 3-D simulation of tectonic evolution of the Mariana arc-back-arc system with a coupled model of plate subduction and back-arc spreading, *Tectonophysics*, doi:10.1016/j.tecto.2008.05.005 (in press).

Hashimoto, C., K. Fukui, and M. Matsu'ura (2004), 3-D modelling of plate interfaces and. numerical simulation of long-term crustal deformation in and around Japan, *Pure Appl. Geophys*., 161, 2053-2068.

Hashimoto, C. and M. Matsu'ura (2008), 3-D simulation of steady plate subduction with tectonic erosion: Current crustal uplift and free-air gravity anomaly, *Pure Appl. Geophys*., 165, 567-583.

Honda, S. (1985), Thermal structure beneath Tohoku, northeast Japan: a case study for

understanding the detailed thermal structure of the subduction zone, *Tectonophysics*, 112, 69-102.

Hughes, T. J. R. (1980), Generalization of selective integration procedures to anisotropic and non linear media, *Int. Numer. Meth. Eng.*, 15, 1413-1418.

Jarrard, R. D. (1986), Relations among subduction parameters, *Rev. Geophys.*, 24, 217-284.

Jungles, P. H., and G. A. Frazier (1973), Finite element analysis for the residual displacements for and earthquake rupture: source parameters for the San Fernando earthquake, Models of tectonic processes associated with earthquakes, *J. Geophys. Res*., 78, 5062-5083.

Kaufmann G., P. Wu, and D. Wolf (1997), Some effects of lateral heterogeneities in the upper mantle on postglacial land uplift close to continental margins, *Geophys. J. Int*., 128, 175-187.

Koons, P. O. (1987), Some thermal and mechanical consequences of rapid uplift; an example. from the Southern Alps, New Zealand, *Earth Planet. Sci. Lett*., 86, 307-319.

Lee, E. H. (1955), Stress analysis in visco-elastic bodies, *Q. Appl. Math.*, 13, 183-190.

Marc Analysis Research Corp. (1994), Volume A User Information, *Palo Alt CA*.

Maruyama, T. (1963), On the force equivalent of dynamic elastic dislocations with reference to the earthquake mechanism, *Bull. Earthquake Res. Inst*., 41, 467-486.

Matsu'ura, M., T. Tanimoto, and T. Iwasaki (1981), Quasi-static displacements due to faulting in a layered half-space with an intervenient viscoelastic layer, *J. Phys. Earth*., 29, 23-54.

Matsu'ura, M., and T. Sato (1989), A dislocation model for the earthquake cycle at

convergent plate boundaries, *Geophys. J. Int.*, 96, 23-32.

McConnell, R. (1965), Isostatic adjustment in a layered earth, *J. Geophys. Res.*, 70, 5171-5188.

Melosh, H. J., and A. Raefsky (1980), The dynamical origin of subduction zone topography, *Geophys. J. R. Astr. Soc.*, 60, 333-354.

Melosh, H. J., and A. Raefsky (1981), A simple and efficient method for introducing faults into finite element computations, *Bull Seism. Soc. Am.*, 71, 1391-1400.

Melosh, H. J., and C. A. Williams (1989), Mechanics of graben formation in crustal rocks: A finite element analysis, *J. Geophys. Res.*, 94, 13,961-13,973.

Moresi, L., and M. Gurnis (1996), Constraints on the lateral strength of slabs from three-dimensional dynamic low models, *Earth Planet. Sci. Lett.*, 138, 15-28.

Müller, R. D., W. R. Roest, J. Y. Royer, L. M. Gahagan, and J. G. Sclater (1997), Digital isochrons of the world's ocean floor, *J. Geophys. Res*., 102, 3211-3214.

Platt J. P., and P. C. England (1994), Convective removal of lithosphere beneath mountain belts; thermal and mechanical consequences, *Am. J. Sci*., 294, 307-336.

Radok, J. R. M. (1957), Visco-elastic stress analysis, *Q. Appl. Math.*, 15, 198-202.

Royden, L. H. (1993), Evolution of retreating subduction boundaries formed during continental collision, *Tectonics*, 12, 629-638.

Sandwell, D. T., and W. H. F. Smith (1997), Marine gravity anomaly from Geosat and ERS 1 satellite altimetry, *J. Geophys. Res.*, 102, 10039-10054.

Sato, T., and M. Matsu'ura (1992), Cyclic crustal movement, steady uplift of marine terraces, and evolution of the island arc-trench system in southwest Japan, *Geophys. J. Int.*, 111, 617-629.

Sato, T., and M. Matsu'ura (1993), A kinematic model for evolution of island arc-trench

systems, *Geophys. J. Int.*, 114, 512-530.

Sclater, J. G., and B. Parsons, (1981), Oceans and continents: Similarities and differences in the mechanism of heat loss, *J. Geophys. Res.*, 86, 11535-11552.

Sella, G. F., T. H. Dixon, and A. Mao (2002), REVEL: A model for Recent plate velocities from space geodesy, *J. Geophys. Res.*, 107, 2081, doi:10.1029/2000JB000033.

Smith, A. T. (1974), Time-dependent strain accumulation and release at Island Arcs: implications for the 1946 Nankaido Earthquake, Ph.D. Thesis, 292 pp., MIT, Cambridge.

Takada, Y., and M. Matsu'ura (2004), A unified interpretation of vertical movement in Himalaya and horizontal deformation in Tibet on the basis of elastic and viscoelastic dislocation theory, *Tectonophysics*, 383, 105-131.

Takada, Y., and M. Matsu'ura (2007), Geometric evolution of a plate interface-branch fault system: Its effects on tectonic development in Himalaya, *J. Asian Earth Sciences*, 29, 490-503.

Toth, J., and M. Gurnis (1998), Dynamics of subduction initiation at preexisting fault zones, *J. Geophys. Res.*, 103, 18053-18067.

Wdowinski, S., and R. O'Connell (1991), Deformation of the Central Andes (15°-27°S) derived from a flow model of subduction zones, *J. Geophys. Res.*, 96, 12245-12255.

Williams, C. A., and R. M. Richardson (1991), A rheologically layered three-dimensional model of the San Andreas fault in Southern California, *J. Geophys. Res.*, 96, 16597-16623.

Zhong, S., and M. Gurnis (1994), Controls on trench topography from dynamic models

of subducted slabs, *J. Geophys. Res.*, 99, 15683-15695.

Tables

Table 1: The coefficients of elasticity used for the computation of internal deformation fields by Fukahata & Matsu'ura (2006).

Coefficient of elasticity	Elastic plates	Asthenosphere
Bulk modulus κ	51.85 GPa	51.85 GPa
Rigidity μ	33.19 GPa	3.319 MPa

Table 2: The coefficients of elasticity used for the computation of internal deformation fields in the present study.

Coefficient of elasticity	Elastic plates	Asthenosphere
Bulk modulus κ	50 GPa	50 GPa
Rigidity μ	32 GPa	3.2 MPa

Figure Captions

Figure 1: A quasi-static, plane strain model of steady plate subduction. The oceanic and continental plates (Ω^{e1} and Ω^{e2}) are elastic. The underlying asthenosphere (Ω^{v}) is assumed to be elastic but very weak in shear. The y axis is taken vertically downward, and the $y = 0$ plane represents the Earth's surface. The *x*- and *z*-axes are taken to be perpendicular and parallel to the strike of a plate boundary, respectively.

Figure 2: The schematic explanation for the split node technique. (a) The case of a 1-D problem. (b) The case of a 2-D problem. The arrows represent displacement/force vectors in the local and global node systems.

Figure 3: The schematic diagram showing how to incorporate the effects of negative and positive buoyancy due to surface uplift and subsidence in traction free conditions at the Earth's surface. In the local system, the effects of buoyancy are evaluated at the local nodes 3 and 4 of the element 1 and the local nodes 3 and 4 of the element 2. In the global system, the effects of buoyancy are evaluated at the global nodes 4, 5, and 6.

Figure 4: The geometry and boundary conditions for a problem of beam bending. A $100\,\mathrm{m} \times 10\,\mathrm{m}$ rectangular beam is divided into 100×10 elements. At X = 0 m, the fixed boundary condition, $u = v = 0$, is applied. The upper and bottom boundaries are free. At X = 100 m, a downward force (3.0×10^3 N) is imposed.

Figure 5: Comparison of two numerical solutions for beam bending with different

integration schemes. (a) The numerical solution with the full integration scheme. (b) The numerical solution with the SRI scheme. The solid triangles and the solid squares represent the numerical solutions with the full integration scheme and the SRI scheme, respectively. The solid line represents analytical solution.

Figure 6: The distribution of Gaussian quadrature points in the local coordinate system. (a) The full integration scheme. The crosses indicate the Gaussian quadrature points. (b) The reduced integration scheme. The triangle indicates the Gaussian quadrature point. (c) The selective-reduced integration scheme. The triangle indicates the Gaussian quadrature points for volumetric strain, and the crosses indicate the Gaussian quadrature points for deviatoric strain.

Figure 7: The model setting for numerical computation. The right side of the total model region is set to be horizontally fixed but vertically free. The base is set to be vertically fixed but horizontally free. The left side is set to be free both for horizontal and vertical displacements. The blue thick solid line indicates the split nodes to represent the tangential displacement discontinuity (fault slip) at the plate interface. The blue region is the area where node points are fine and the yellow region is the displayed area in the following figures.

Figure 8: The computed internal velocity fields due to steady plate subduction for a horizontally layered structure model. The upper two diagrams show the horizontal and vertical velocity profiles at the surface. In each diagram, the red line indicates the surface velocities computed by the FEM model, and the green line indicates those

computed on the basis of analytical expressions by Fukahata & Matsu'ura (2006). The bottom diagram shows the velocity field computed by the present FEM model.

Figure 9: The computed internal velocity fields due to steady plate subduction for a descending slab model. The upper two diagrams show the horizontal and vertical velocity profiles at the surface. In each diagram, the red line indicates the surface velocities for the descending slab model, and the green line indicates those for the horizontally layered structure model. The bottom diagram shows the velocity field computed by the descending slab model.

Figure 10: The effects of the thickness of descending oceanic plates L_s on the surface velocity patterns. The upper and lower panels show the horizontal and vertical velocity patterns, respectively. In each panel, the red, black, and green lines correspond to the case of L_s = 30, 50, and 80 km, respectively.

Figure 11: The effects of the thickness of overriding continental plates L_o on the surface velocity patterns. (a) The vertical velocity patterns for L_o = 20 (red), 30 (green), 40 (blue) and 50 (black) km. (b) The vertical velocity patterns for L_o = 50 (black), 60 (blue), 70 (green) and 80 (red) km.

Figure 12: The temperature field at the initial condition (t = 0). The temperature distribution is represented by the color scale on the right and the isotherms (green lines) with the interval of 200 °C . The lithosphere-asthenosphere boundary, which corresponds to the isotherm of 700 °C , is represented by the blue line. The temperature

at the Earth's surface is taken to be $0\,°\mathrm{C}$.

Figure 13: The internal velocity field used for the computation of thermal structure development. The blue line indicates the lithosphere-asthenosphere boundary. The internal velocity field was computed by giving steady slip at a constant rate of 5 cm/yr along the plate interface indicated by the curved solid line. The upper panel shows surface uplift rates.

Figure 14: The development of thermal structure due to steady plate subduction computed with the thermal FEM model. The internal velocity field in Fig. 13 is given as advection terms in the thermal transfer equation. The panels (a)-(f) are a series of snapshots at $t = 0$, 1, 2, 3, 4 and 5 Myr. The temperature distribution is represented by the color scale on the right and the isotherms (green lines) with the interval of $200\,°\mathrm{C}$. The blue line indicates the $700\,°\mathrm{C}$ isotherm, which corresponds to the lithosphere-asthenosphere boundary.

Figure 15: The result of numerical simulation for the development of mechanical and thermal structure in a subduction zone. The panels (a)-(f) are a series of snapshots at $t = 0$, 1, 2, 3, 4 and 5 Myr. In each panel, the top diagram shows the surface uplift profile indicated by the red line. The black line is the uplift rate profile at $t = 0$. The black arrows in the bottom diagram show the internal velocities. The temperature distribution is represented by the color scale on the right and the isotherms (green lines) with the interval of $200\,°\mathrm{C}$. The blue line indicates the $700\,°\mathrm{C}$ isotherm, which corresponds to the lithosphere-asthenosphere boundary.

Figure 16: The temporal change of the surface uplift rate profile and the lithosphere-asthenosphere boundary. The upper diagram shows the profiles of surface uplift rates at $t = 0$ (black), 2 (red), and 5 (blue) Myr. The bottom diagram shows the lithosphere-asthenosphere boundary (the $700\,°C$ isotherm) at $t = 0$, 2 and 5 Myr with the same color as in the upper diagram.

Figure 17: The development of the surface heat flow profiles computed from the simulation results in Fig. 16. The black, red, green, and blue lines indicate the heat flow profiles at $t = 0$, 1, 3, and 5 Myr. For reference we also show the surface heat flow profiles calculated from the thermal development model assuming constant velocity fields by the broken lines with the same colors in the mechanical-thermal coupled model.

Figure 18: Free-air gravity anomalies and sea floor ages along the Chile trench near the Trench-Trench-Ridge (TTR) triple junction. (a) Free-air gravity anomalies (Müller et al., 1997). (b) Sea floor ages (Sandwell & Smith, 1997).

Figure 19: Free-air gravity anomalies and sea floor ages along the subduction zone of Alaska. (a) Free-air gravity anomalies (Müller et al., 1997). (b) Sea floor ages (Sandwell & Smith, 1997).

Figure 20: Comparison of the observed free-air gravity anomalies and the computed free-air gravity anomaly rates in and around Japan. (a) The observed free-air gravity

anomalies Müller et al. (1997). (b) The computed free-air gravity anomaly rates (Hashimoto & Matsu'ura, 2008).

Figure 21: Free-air gravity anomalies and sea floor ages along the subduction zones of Kuril and Kamchatka. (a) Free-air gravity anomalies (Müller et al., 1997). (b) Sea floor ages (Sclater and Parsons, 1981).

Figures

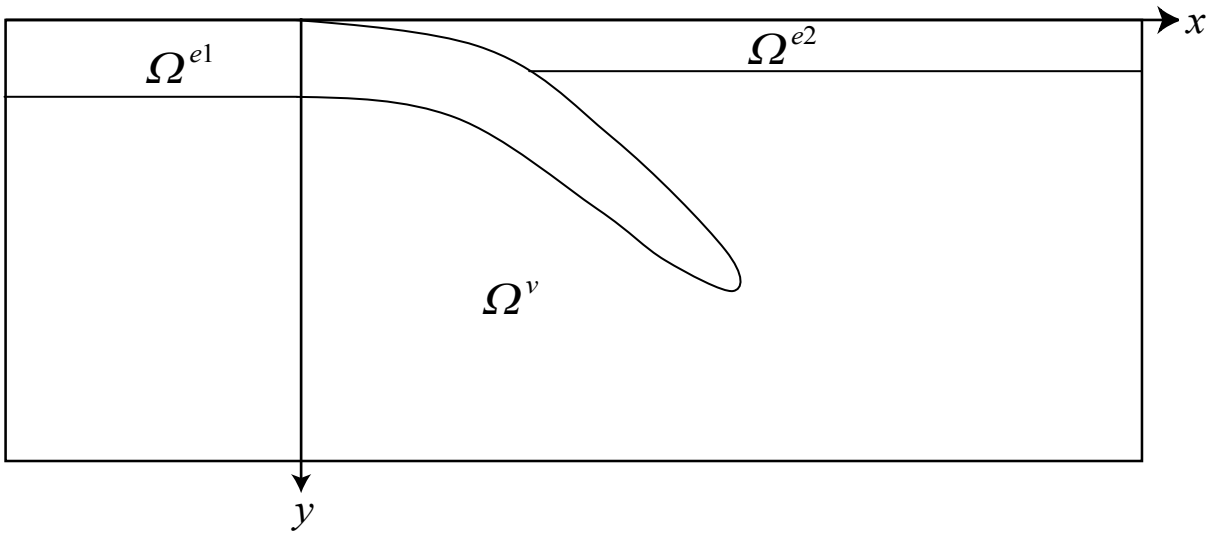

Figure 1

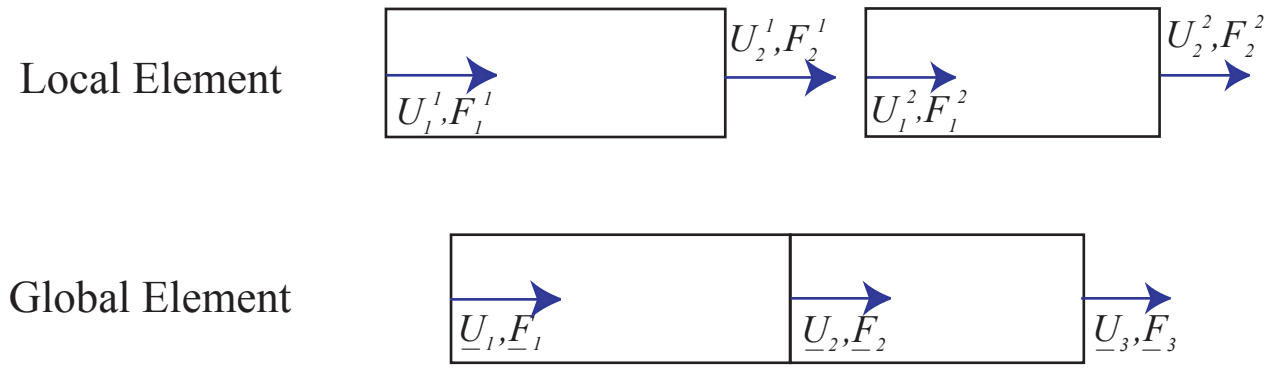
Local Element
U_1^1, F_1^1
U_2^1, F_2^1
U_1^2, F_1^2
U_2^2, F_2^2
Global Element
$\underline{U}_1, \underline{F}_1$
$\underline{U}_2, \underline{F}_2$
$\underline{U}_3, \underline{F}_3$

(a)

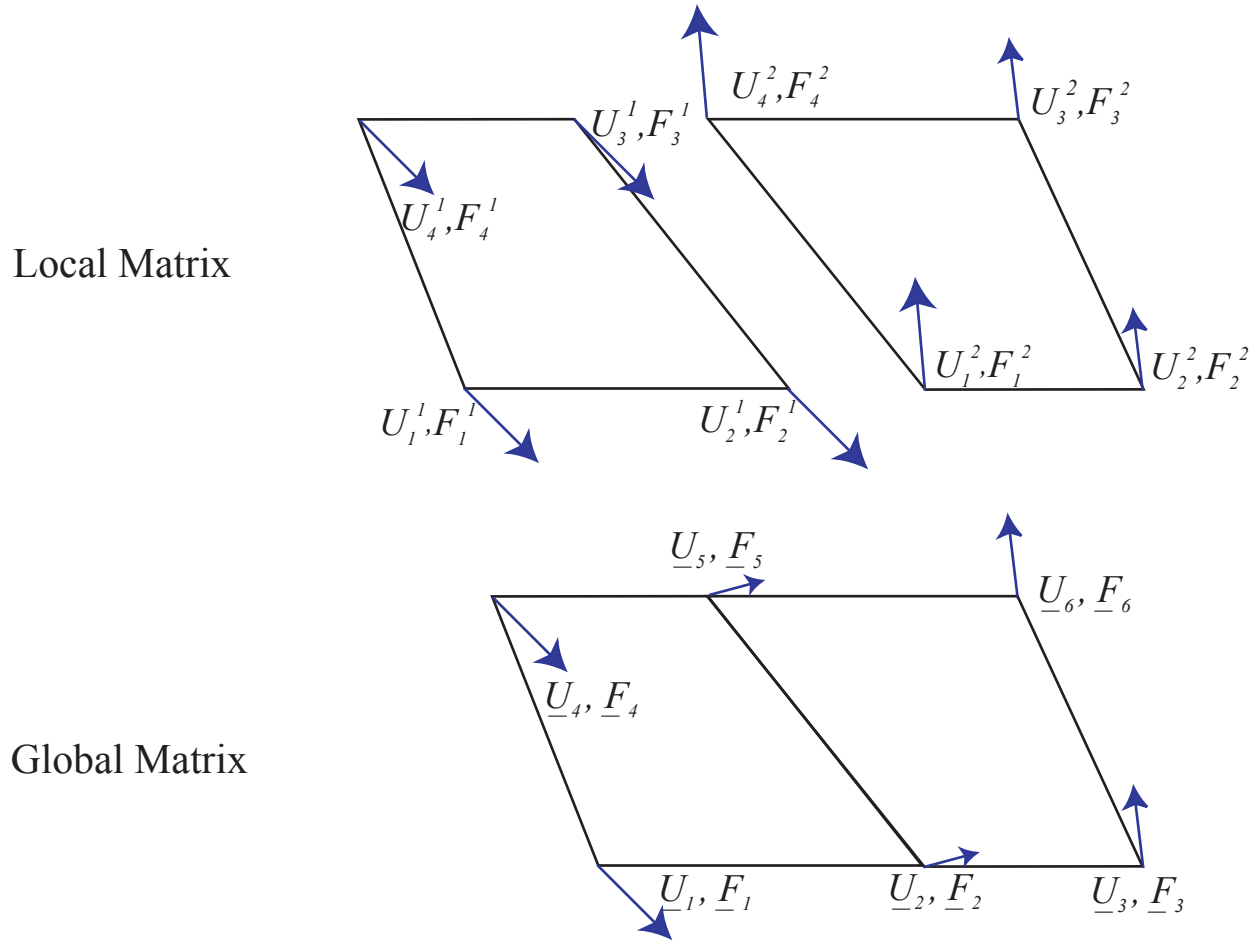
Local Matrix
U_4^1, F_4^1
U_3^1, F_3^1
U_1^1, F_1^1
U_2^1, F_2^1
U_4^2, F_4^2
U_3^2, F_3^2
U_1^2, F_1^2
U_2^2, F_2^2
Global Matrix
$\underline{U}_5, \underline{F}_5$
$\underline{U}_6, \underline{F}_6$
$\underline{U}_4, \underline{F}_4$
$\underline{U}_1, \underline{F}_1$
$\underline{U}_2, \underline{F}_2$
$\underline{U}_3, \underline{F}_3$

(b)

Figure 2

Local Matrix

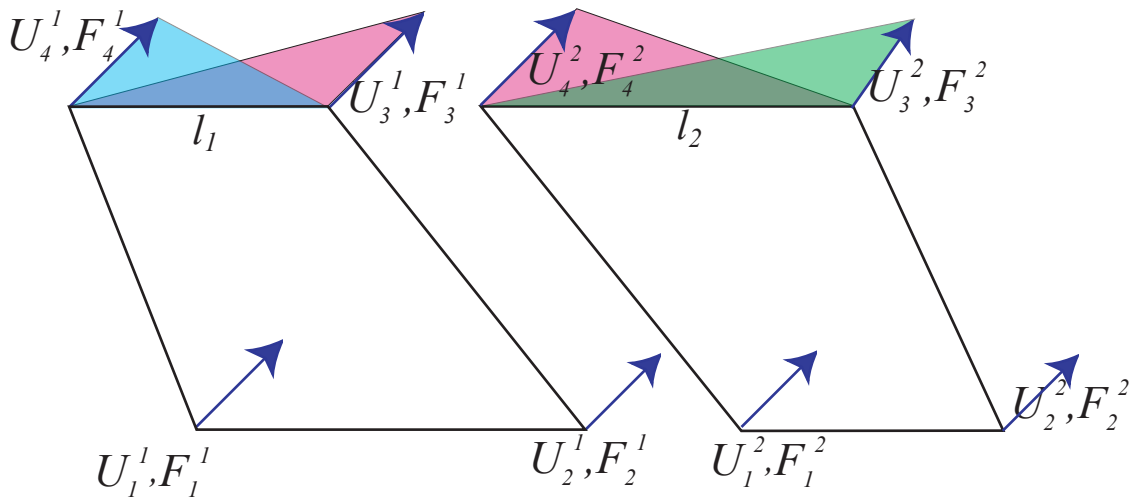

Global Matrix

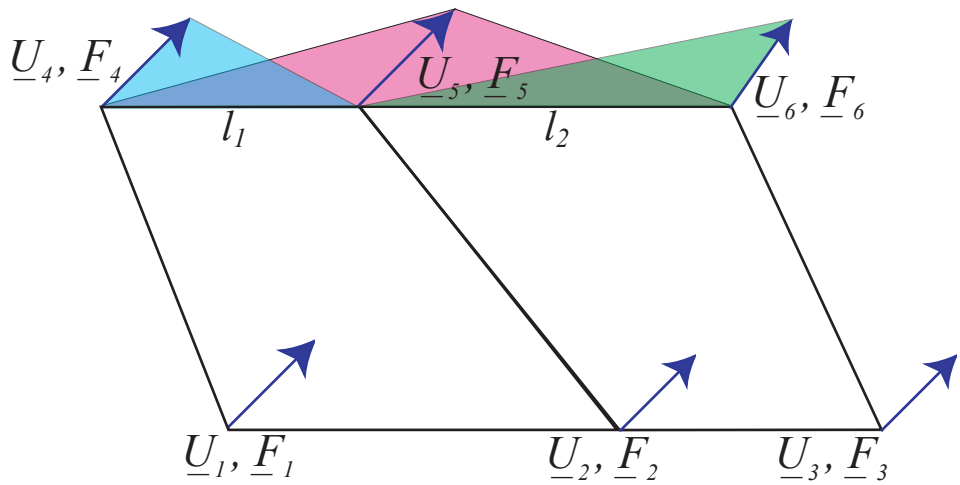

Figure 3

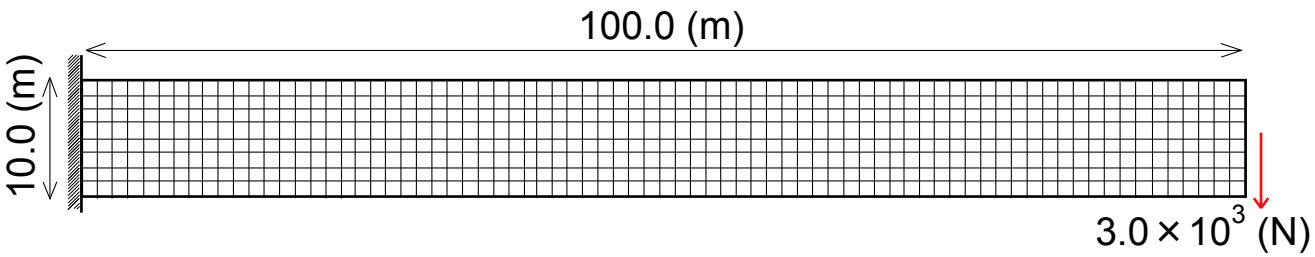

Figure 4

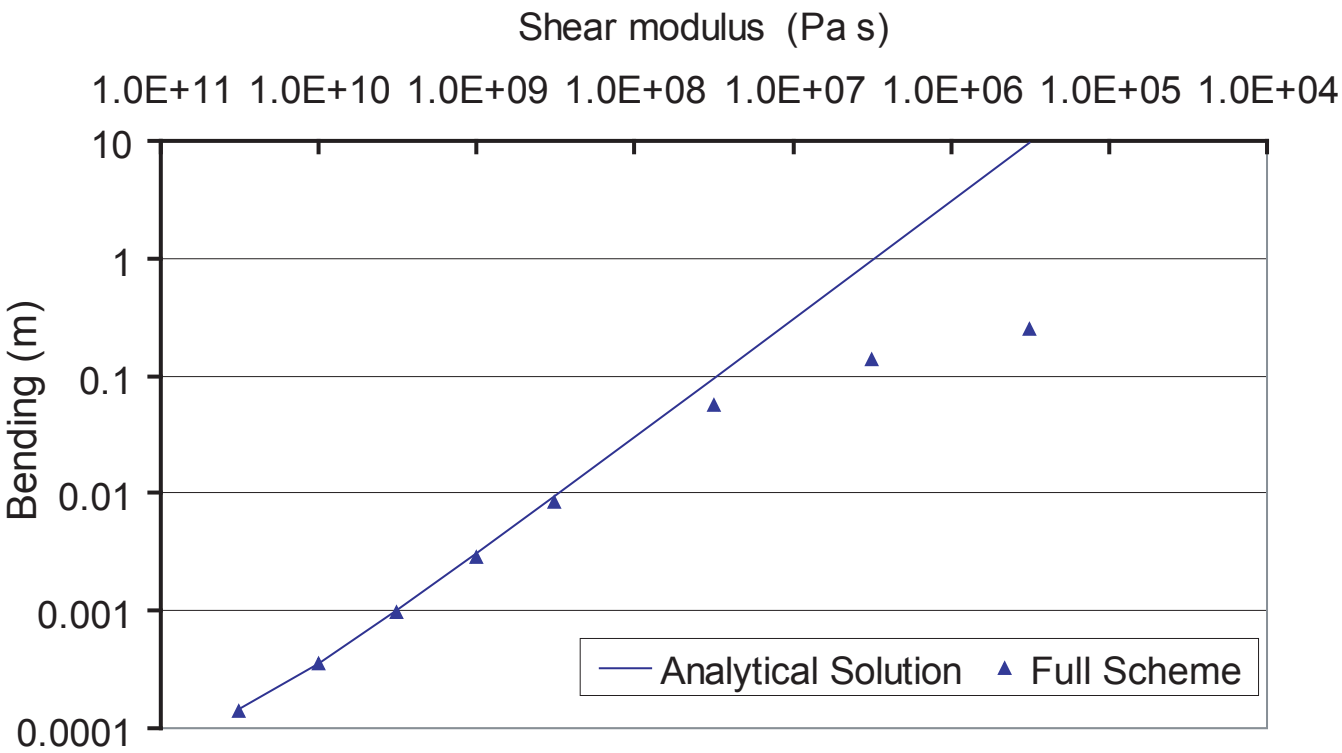
Shear modulus (Pa s)
1.0E+11 1.0E+10 1.0E+09 1.0E+08 1.0E+07 1.0E+06 1.0E+05 1.0E+04
10
1
0.1
0.01
0.001
0.0001
Bending (m)
Analytical Solution
Full Scheme

(a)

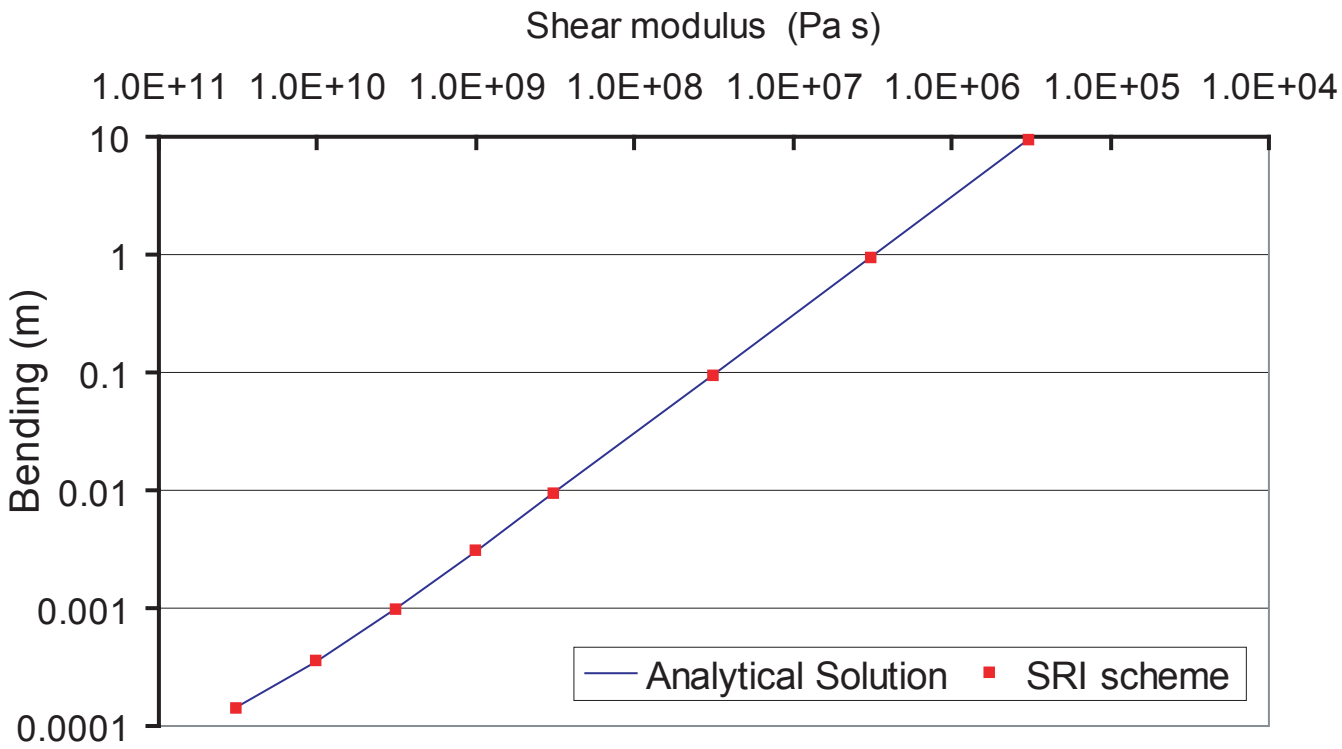
Shear modulus (Pa s)
1.0E+11 1.0E+10 1.0E+09 1.0E+08 1.0E+07 1.0E+06 1.0E+05 1.0E+04
10
1
0.1
0.01
0.001
0.0001
Bending (m)
Analytical Solution
SRI scheme

(b)

Figure 5

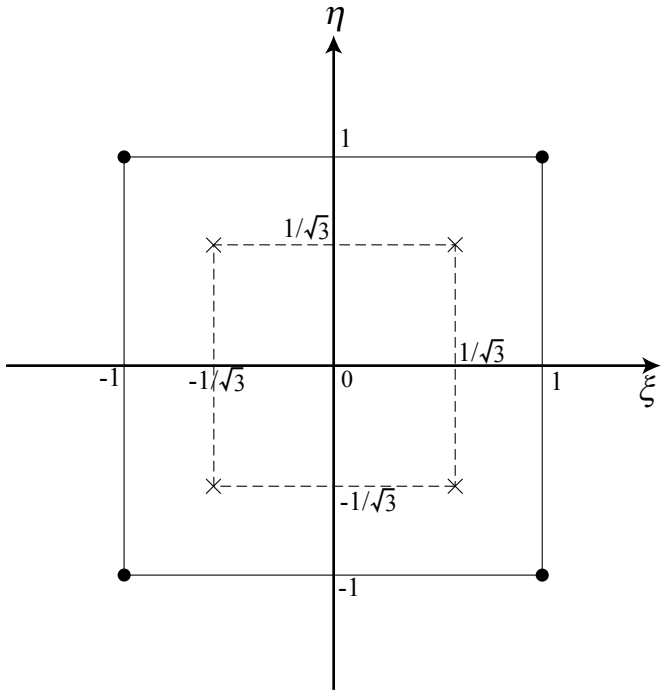

(a)

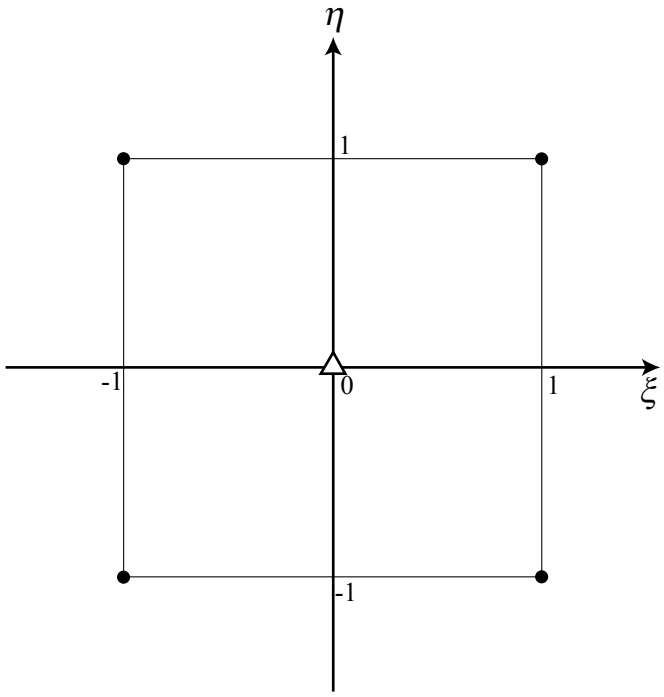

(b)

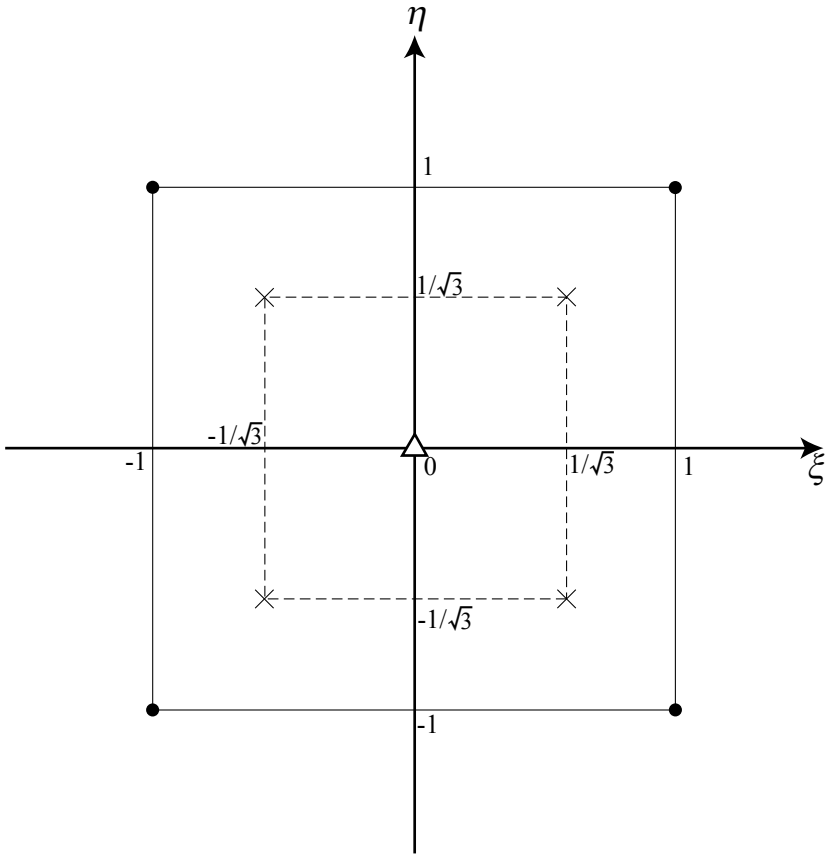

(c)

Figure 6

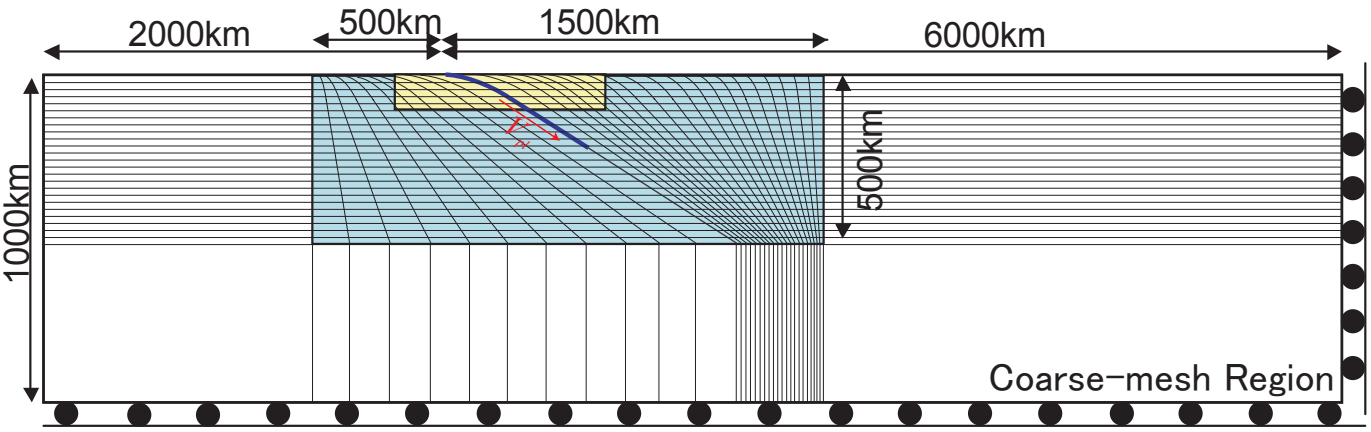

Figure 7

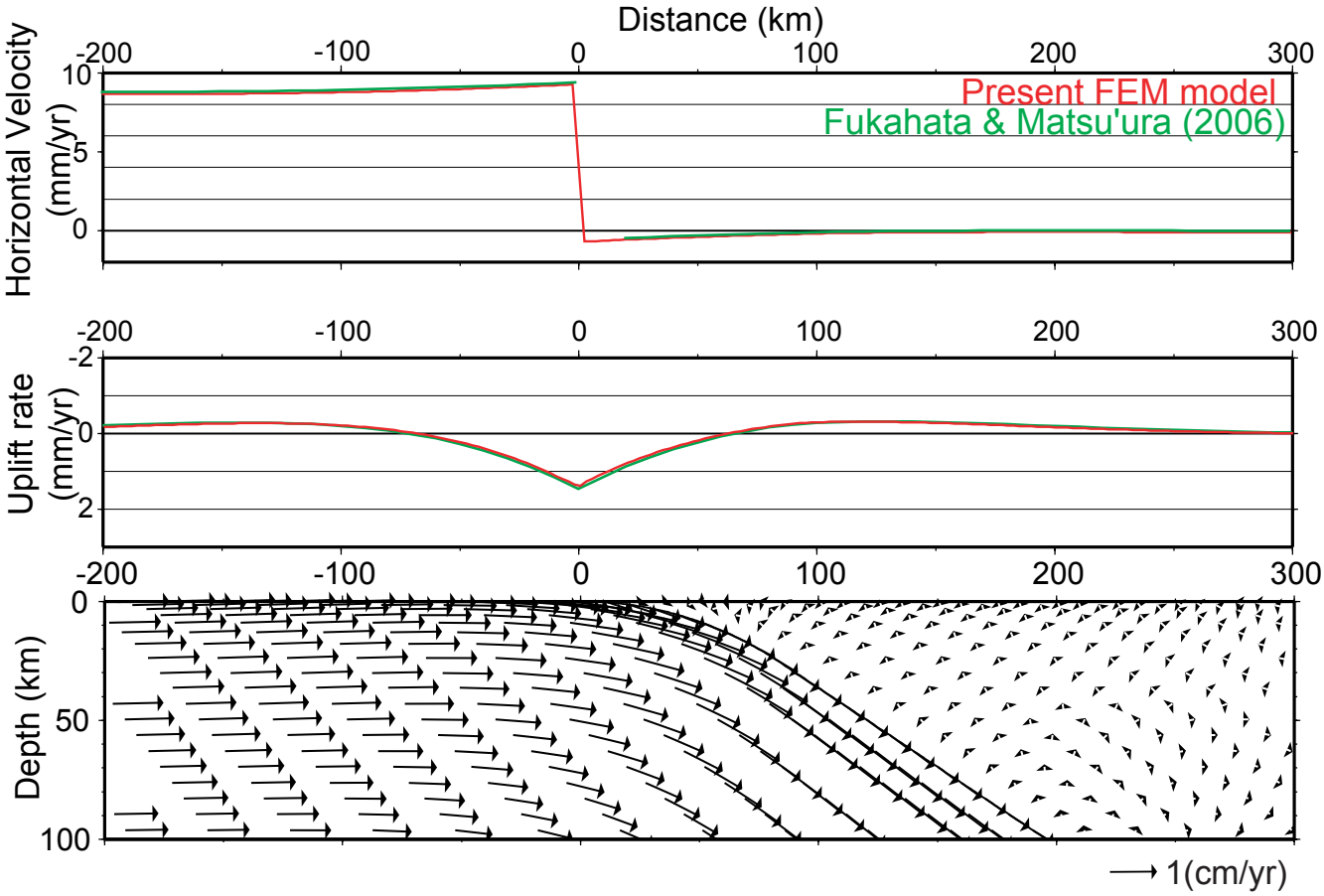

Figure 8

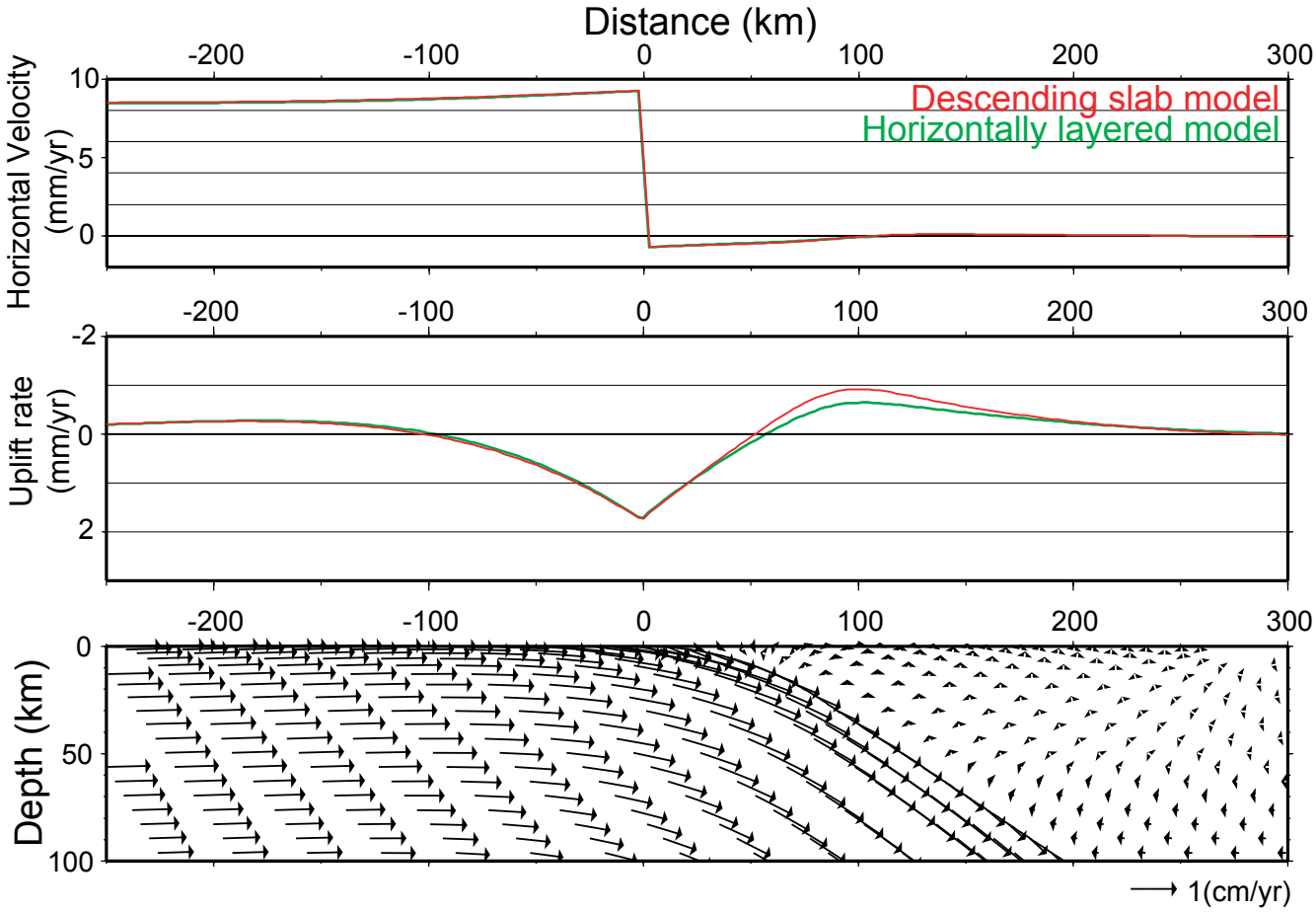

Figure 9

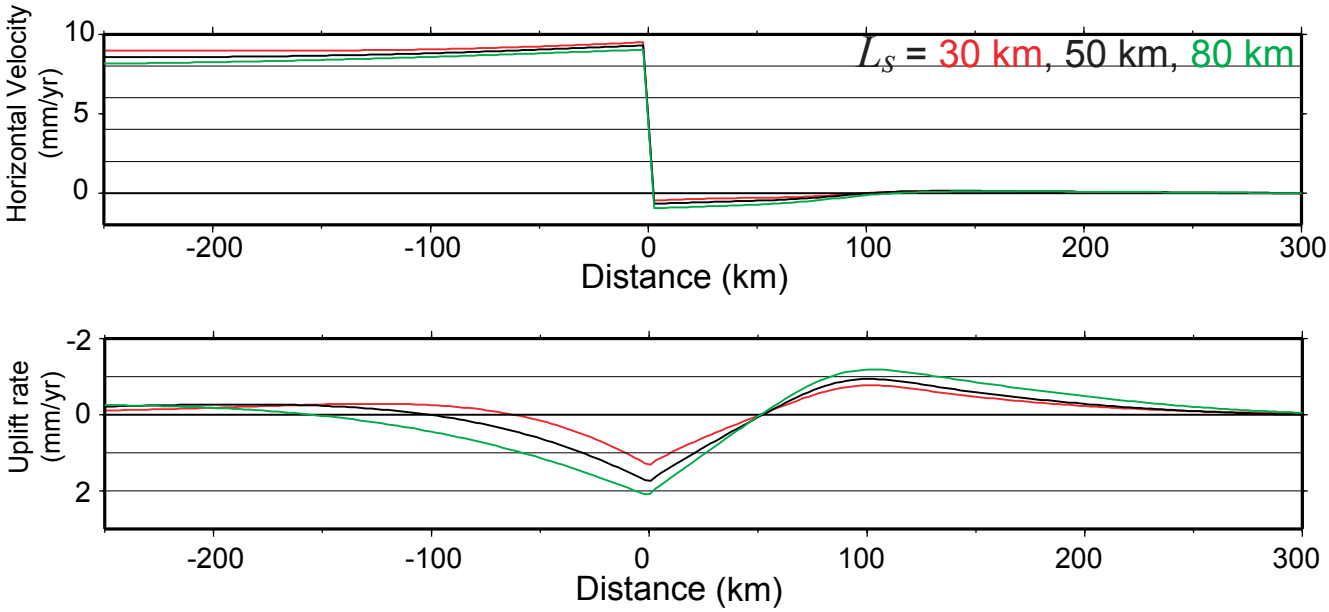

Figure 10

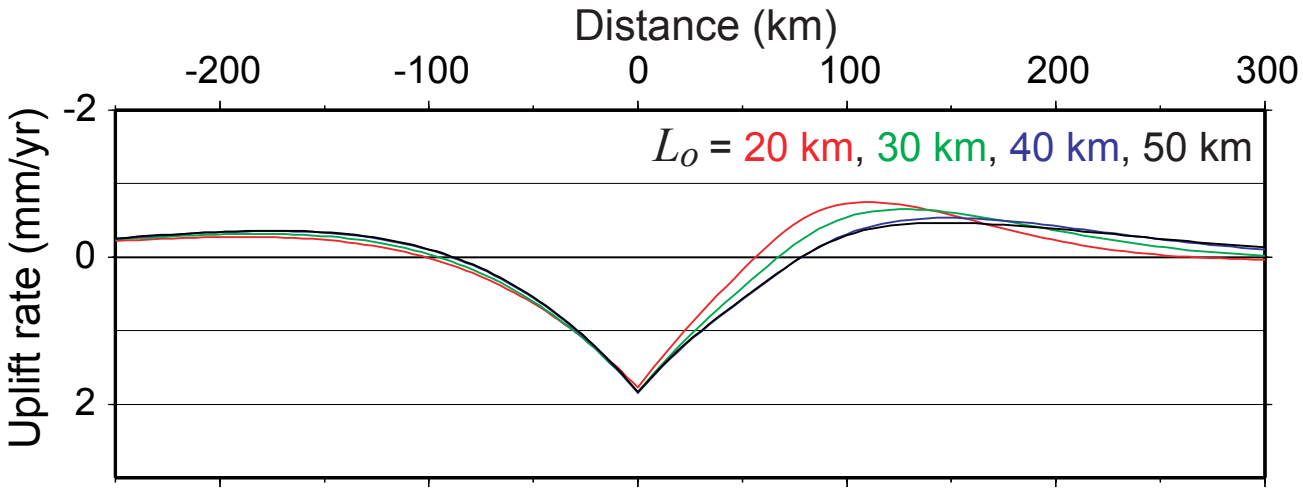
Distance (km)
-200
-100
0
100
200
300
-2
0
2
Uplift rate (mm/yr)
L_o = 20 km, 30 km, 40 km, 50 km

(a)

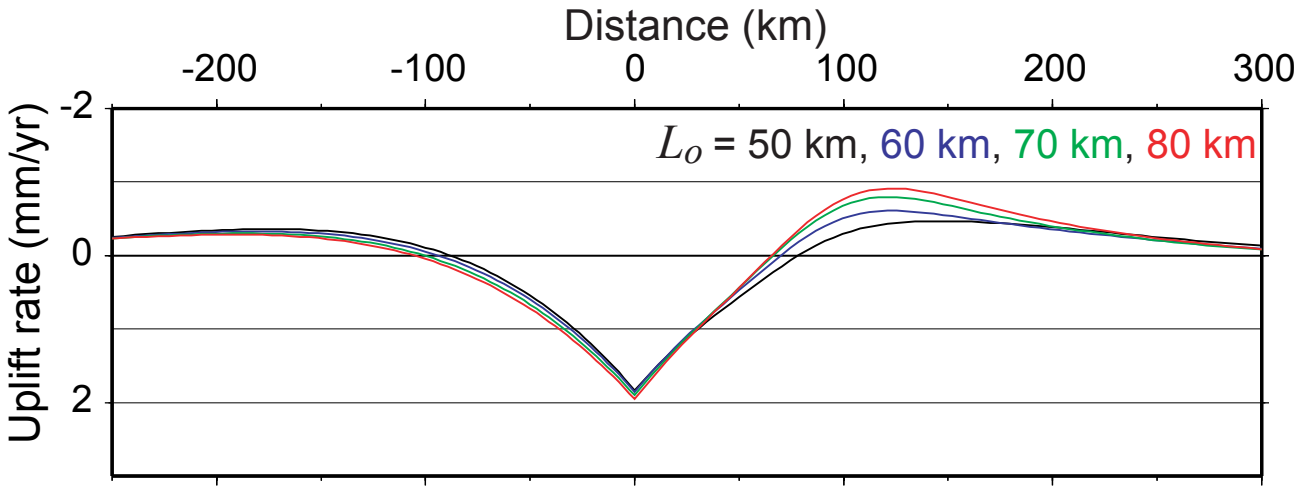
Distance (km)
-200
-100
0
100
200
300
-2
0
2
Uplift rate (mm/yr)
L_o = 50 km, 60 km, 70 km, 80 km

(b)

Figure 11

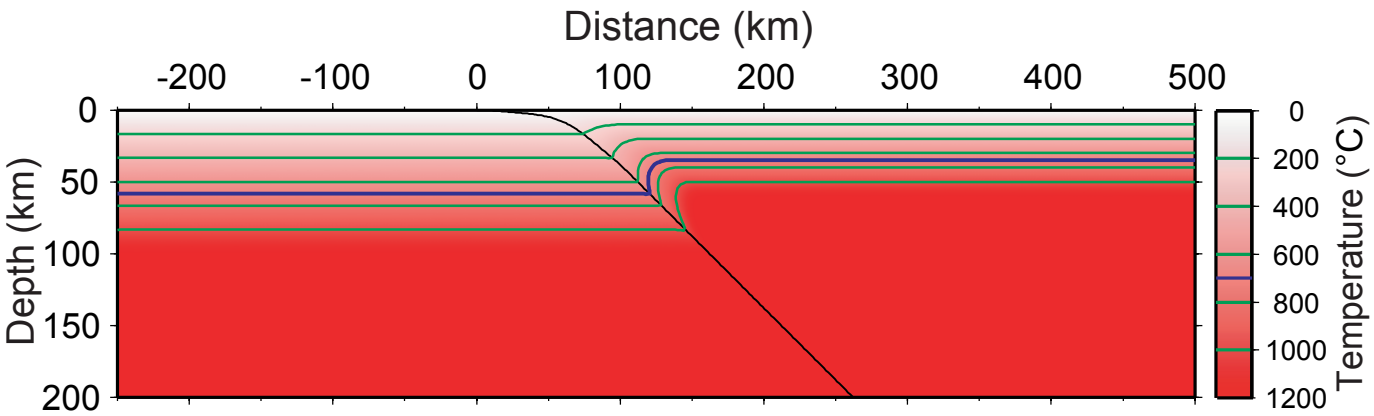

Figure 12

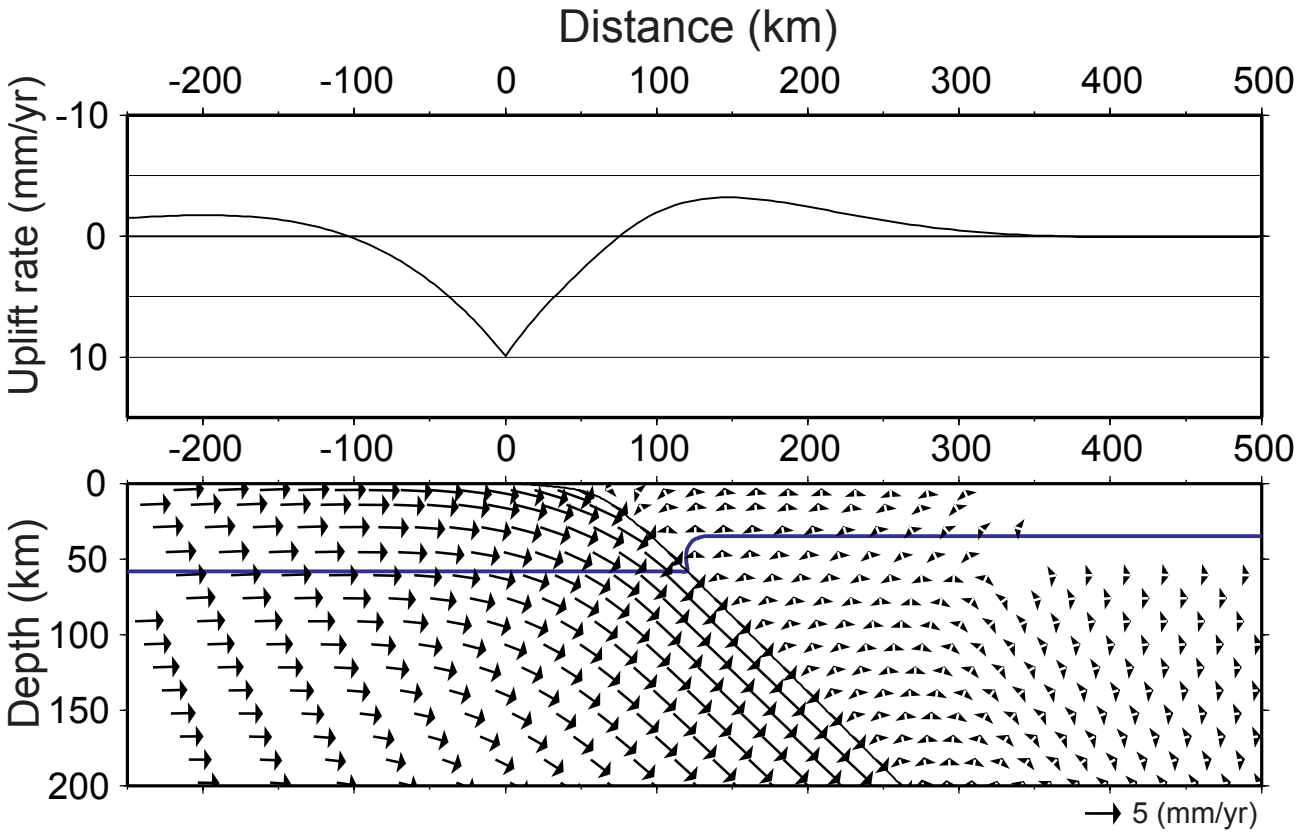

Figure 13

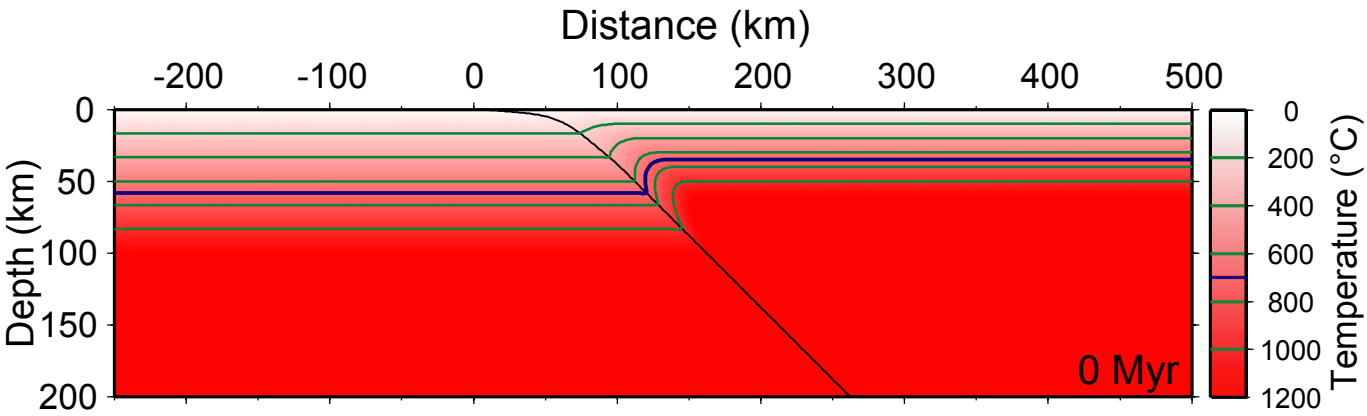

(a)

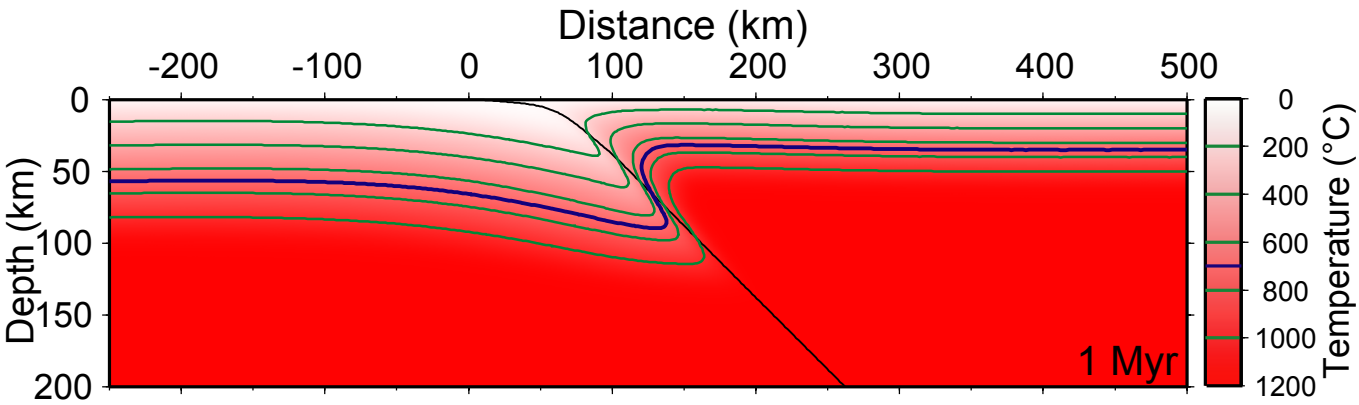

(b)

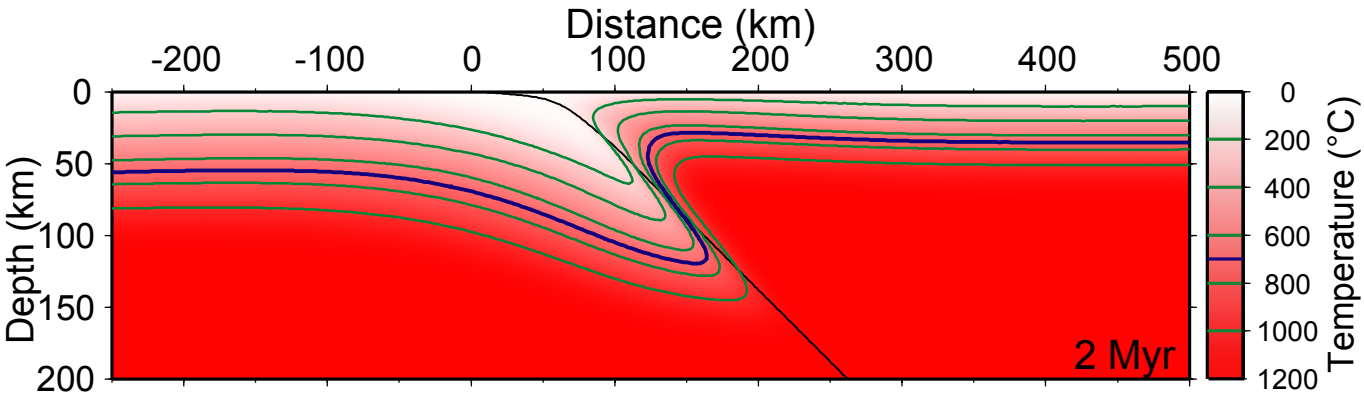

(c)

Figure 14

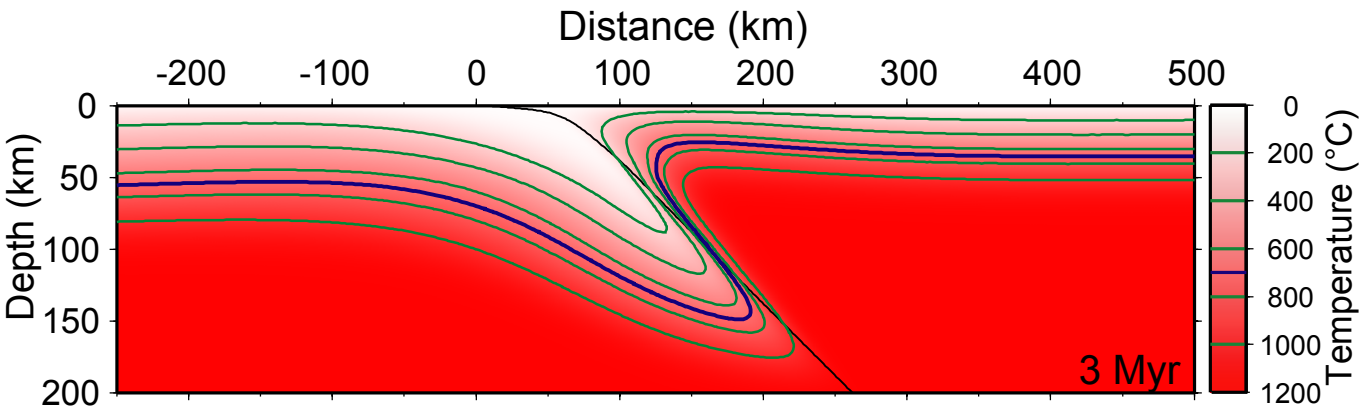

(d)

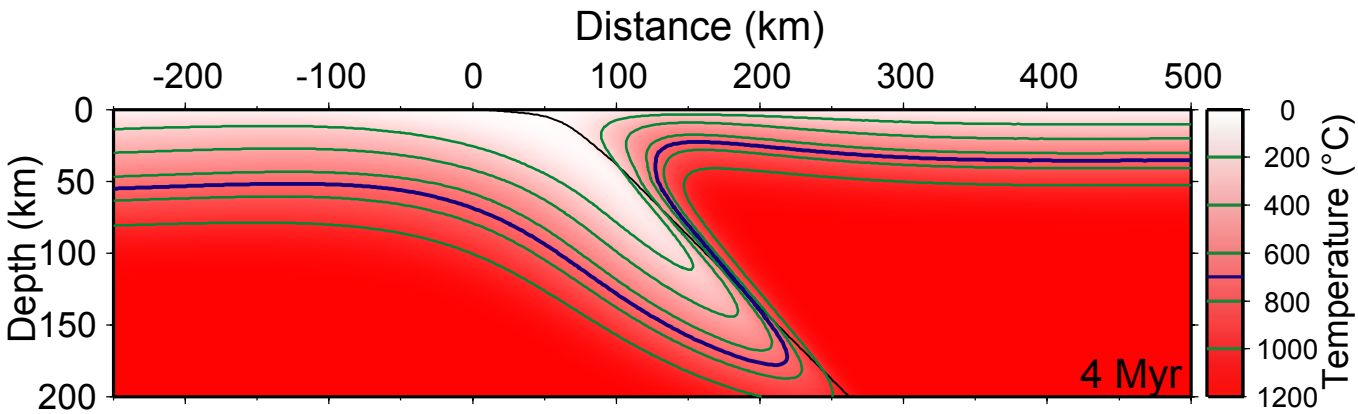

(e)

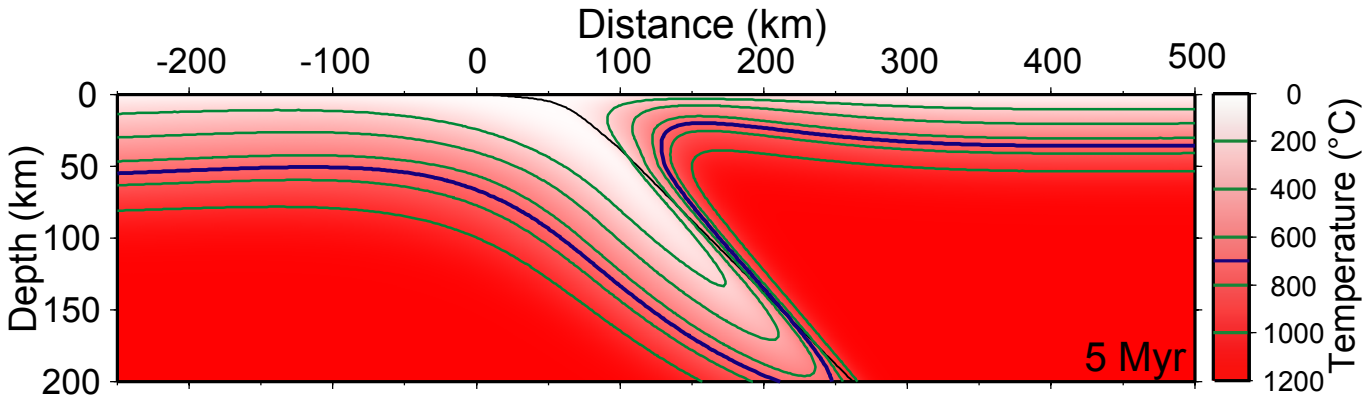

(f)

Figure 14 (continued)

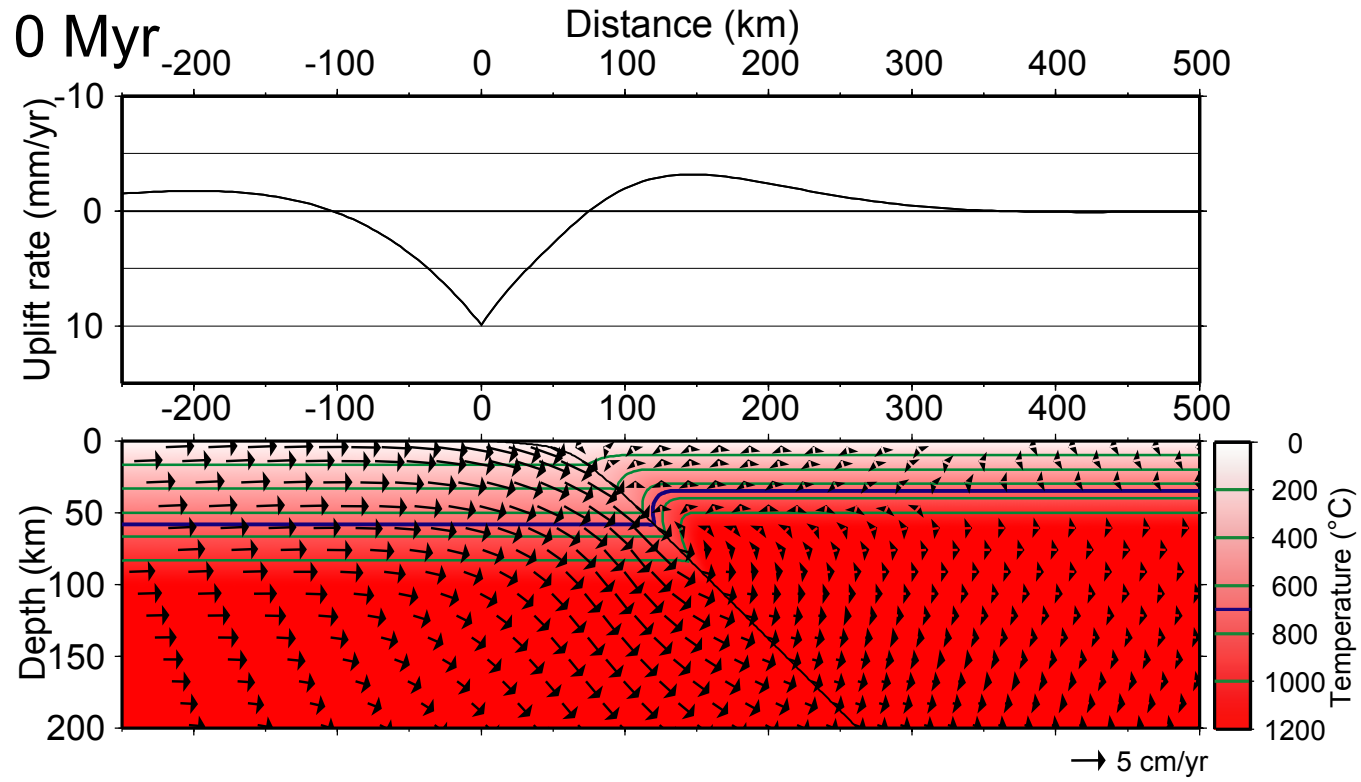
0 Myr
Distance (km)
-200
-100
0
100
200
300
400
500
Uplift rate (mm/yr)
-10
0
10
Depth (km)
0
50
100
150
200
Temperature (°C)
0
200
400
600
800
1000
1200
5 cm/yr

(a)

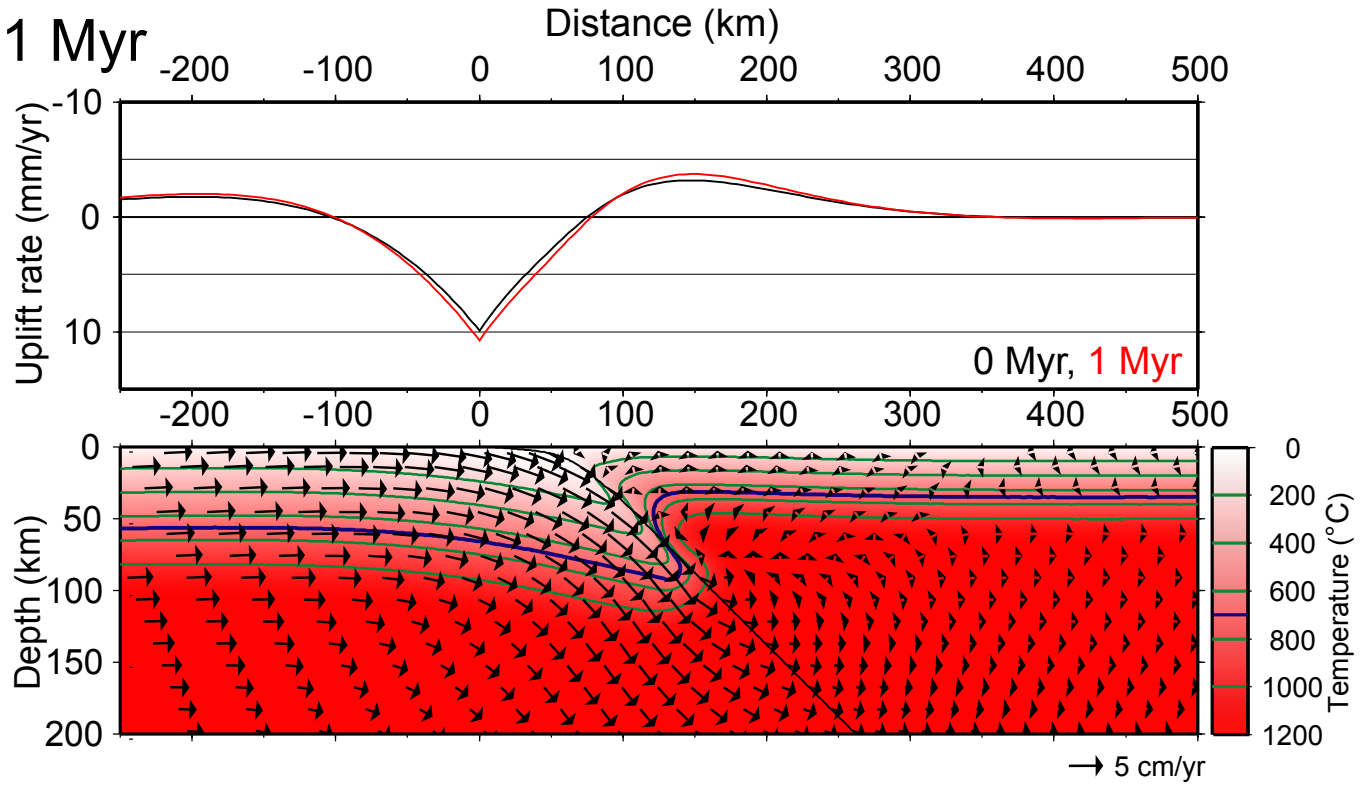
1 Myr
Distance (km)
-200
-100
0
100
200
300
400
500
Uplift rate (mm/yr)
-10
0
10
0 Myr, 1 Myr
Depth (km)
0
50
100
150
200
Temperature (°C)
0
200
400
600
800
1000
1200
5 cm/yr

(b)

Figure 15

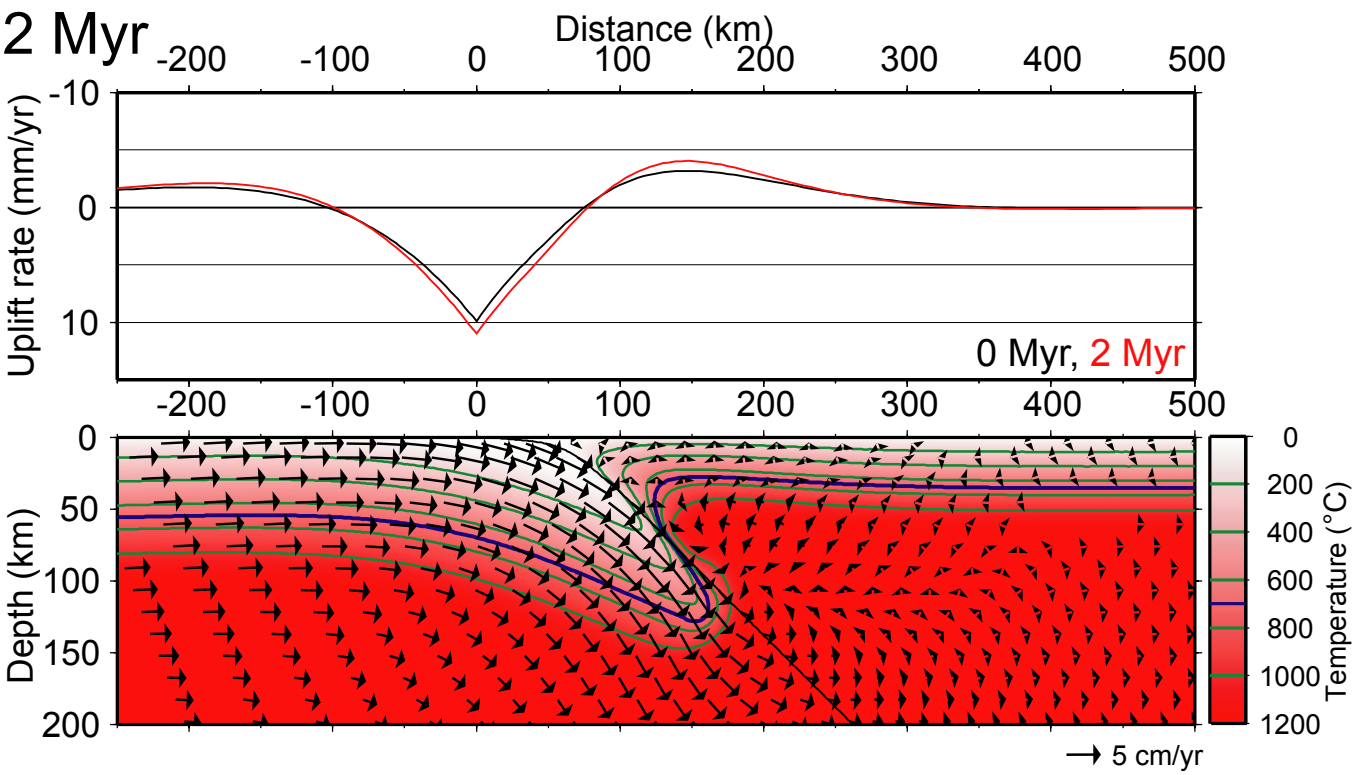

(c)

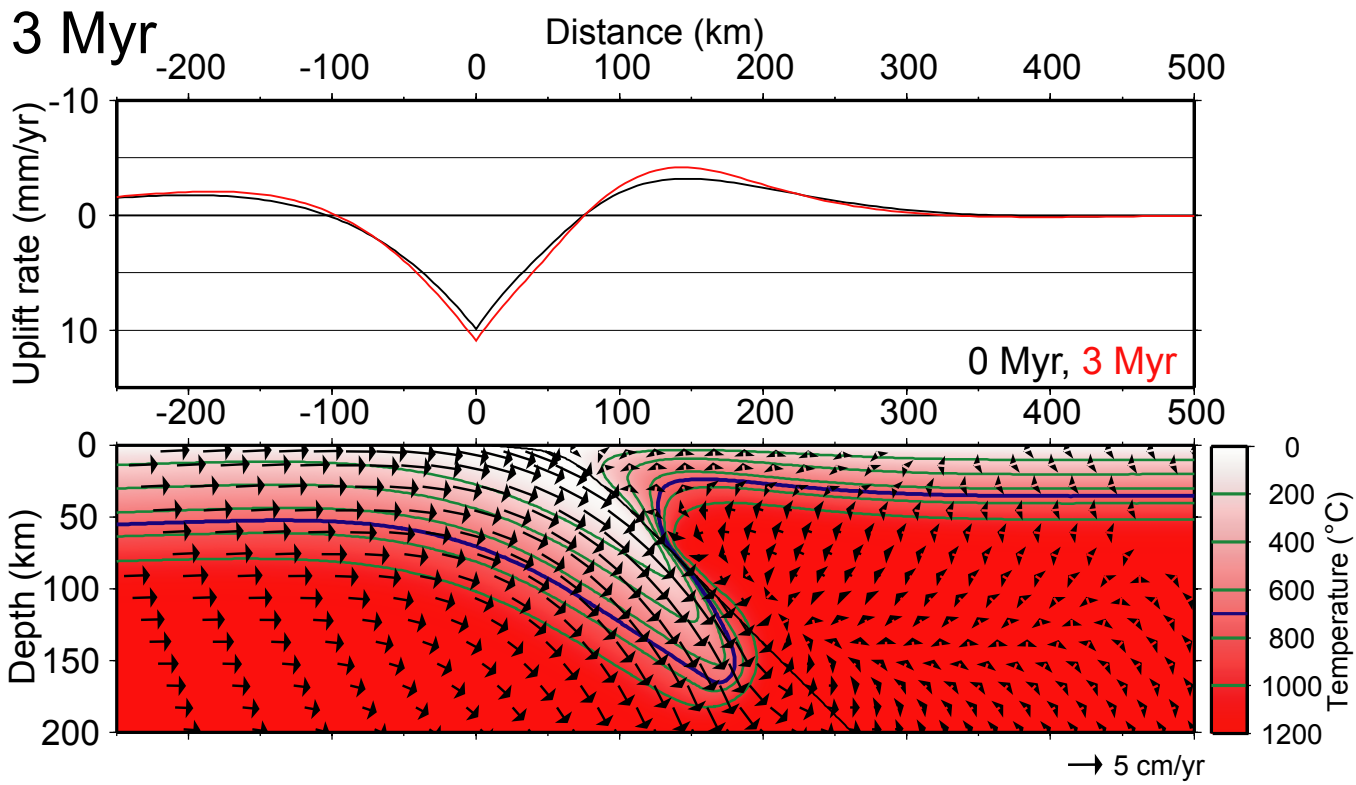

(d)

Figure 15 (continued)

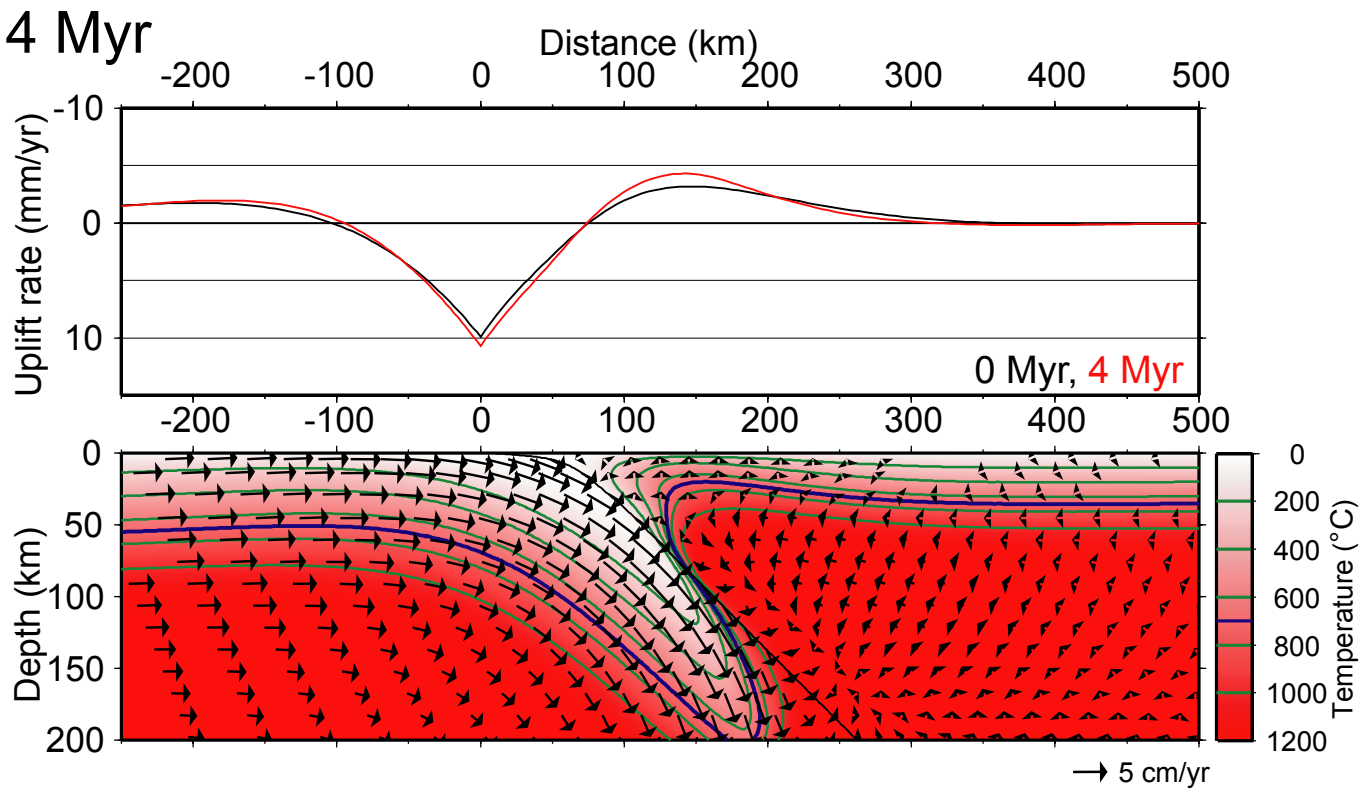

(e)

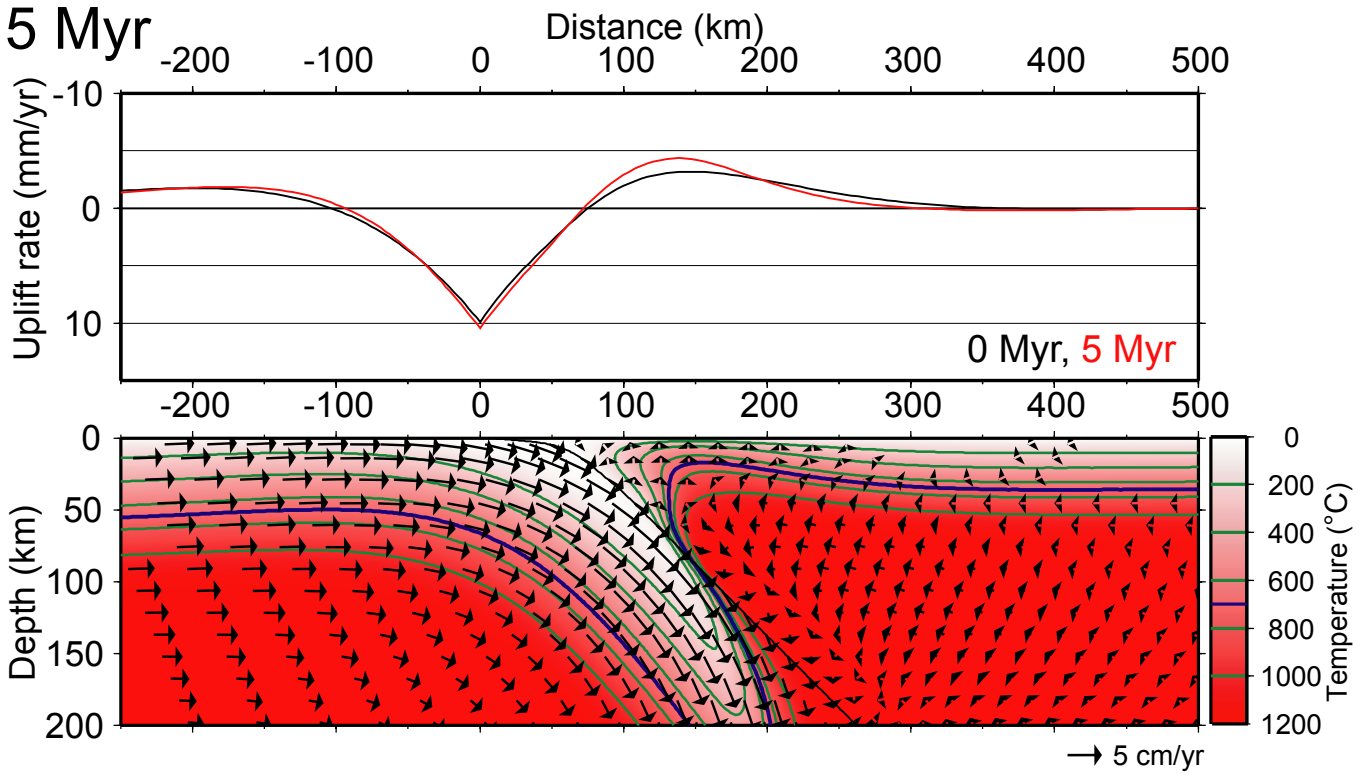

(f)

Figure 15 (continued)

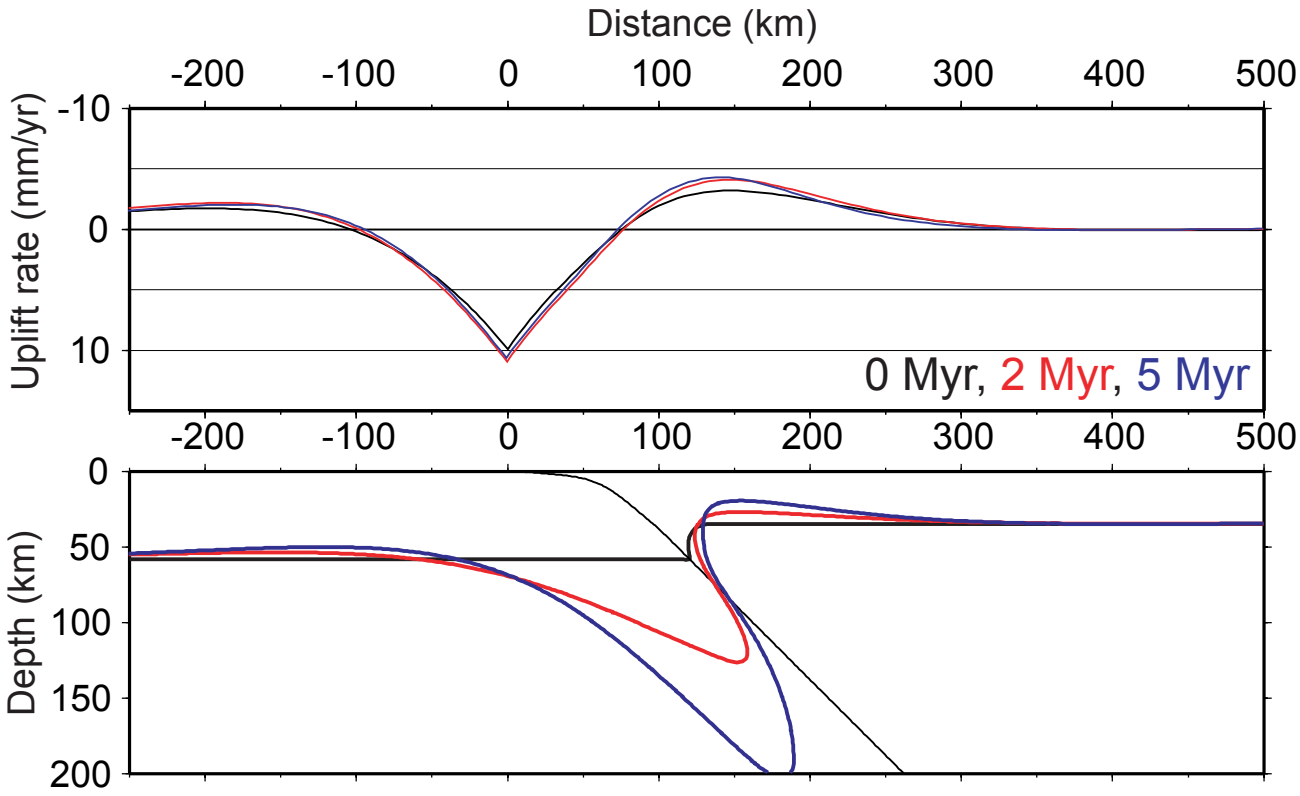

Figure 16

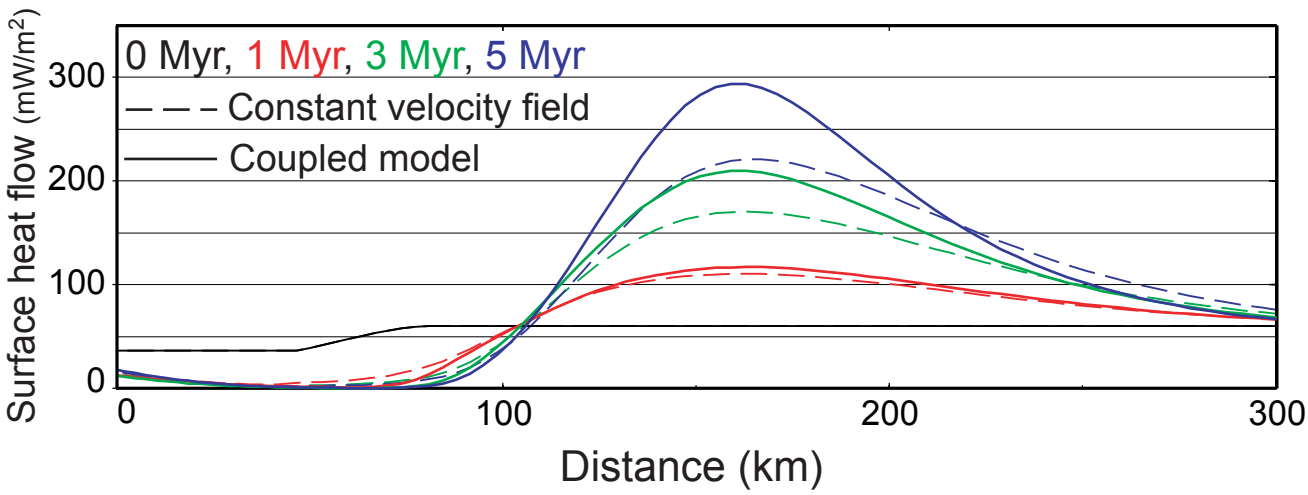

Figure 17

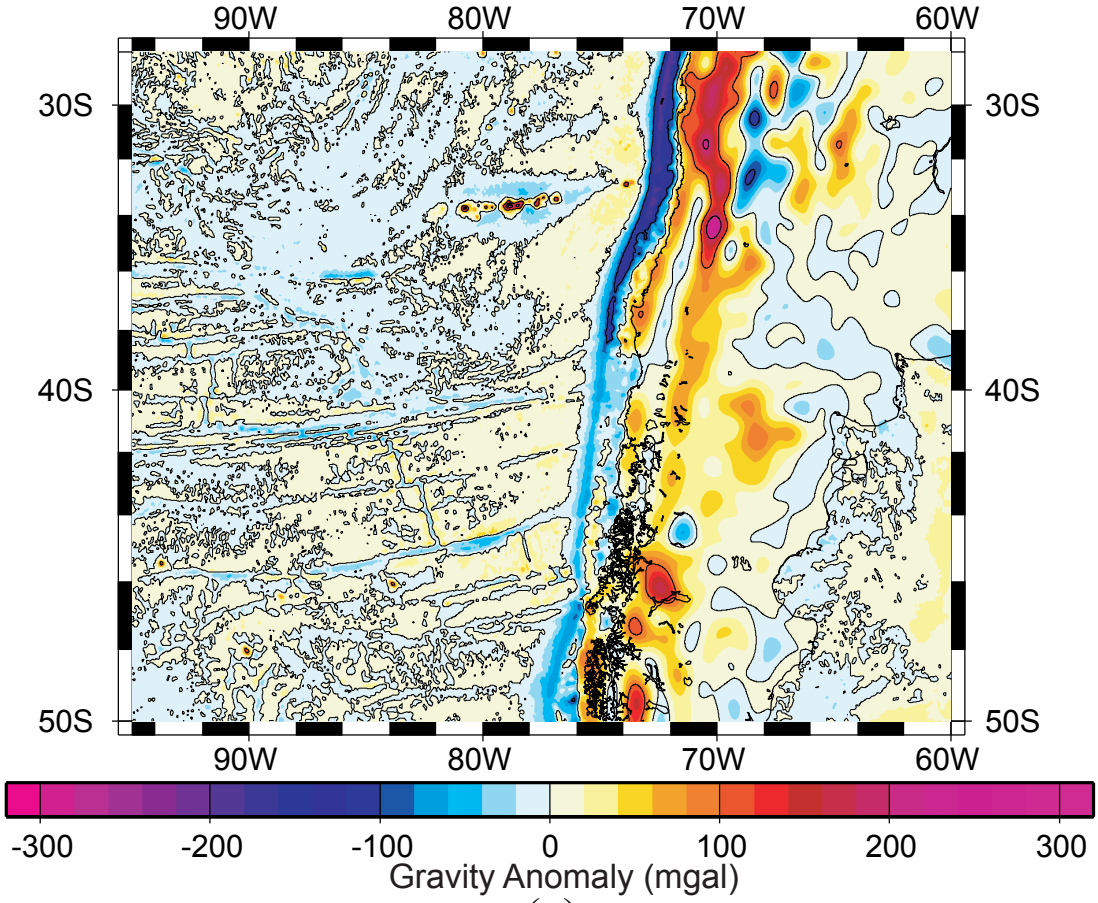
90W
80W
70W
60W
30S
40S
50S
-300
-200
-100
0
100
200
300
Gravity Anomaly (mgal)

(a)

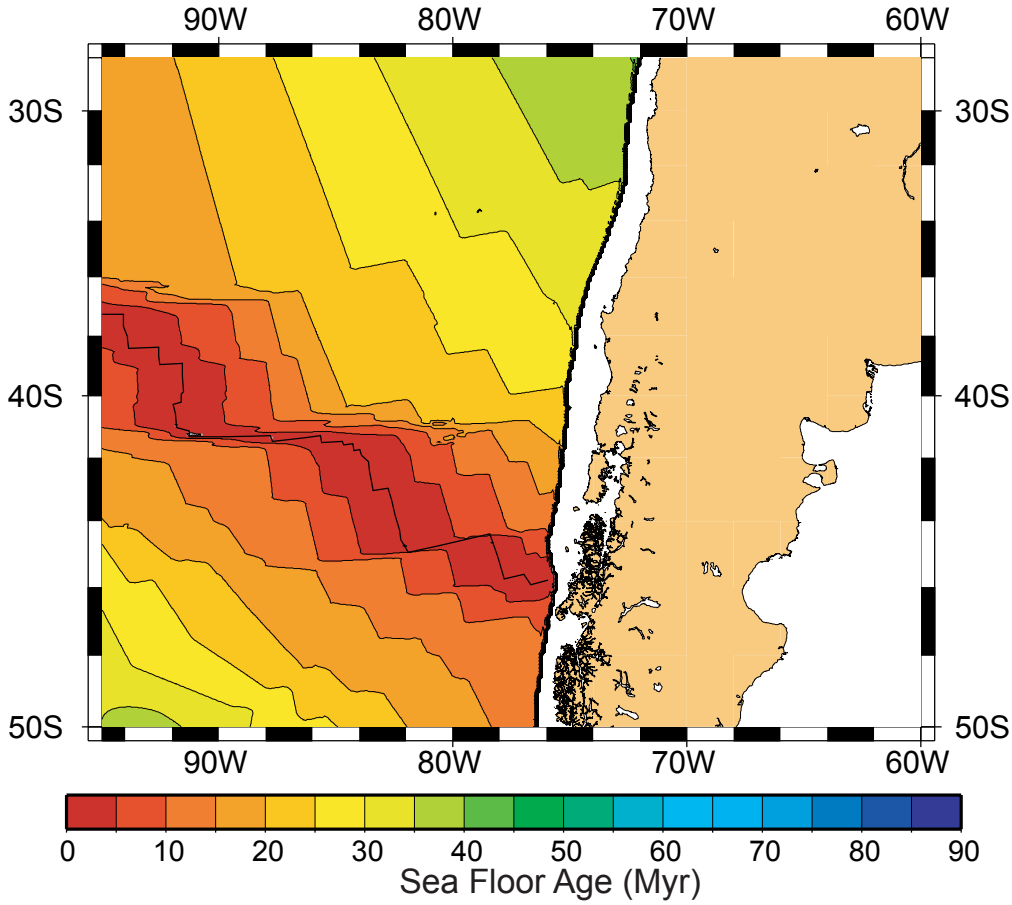
90W
80W
70W
60W
30S
40S
50S
0
10
20
30
40
50
60
70
80
90
Sea Floor Age (Myr)

(b)

Figure 18

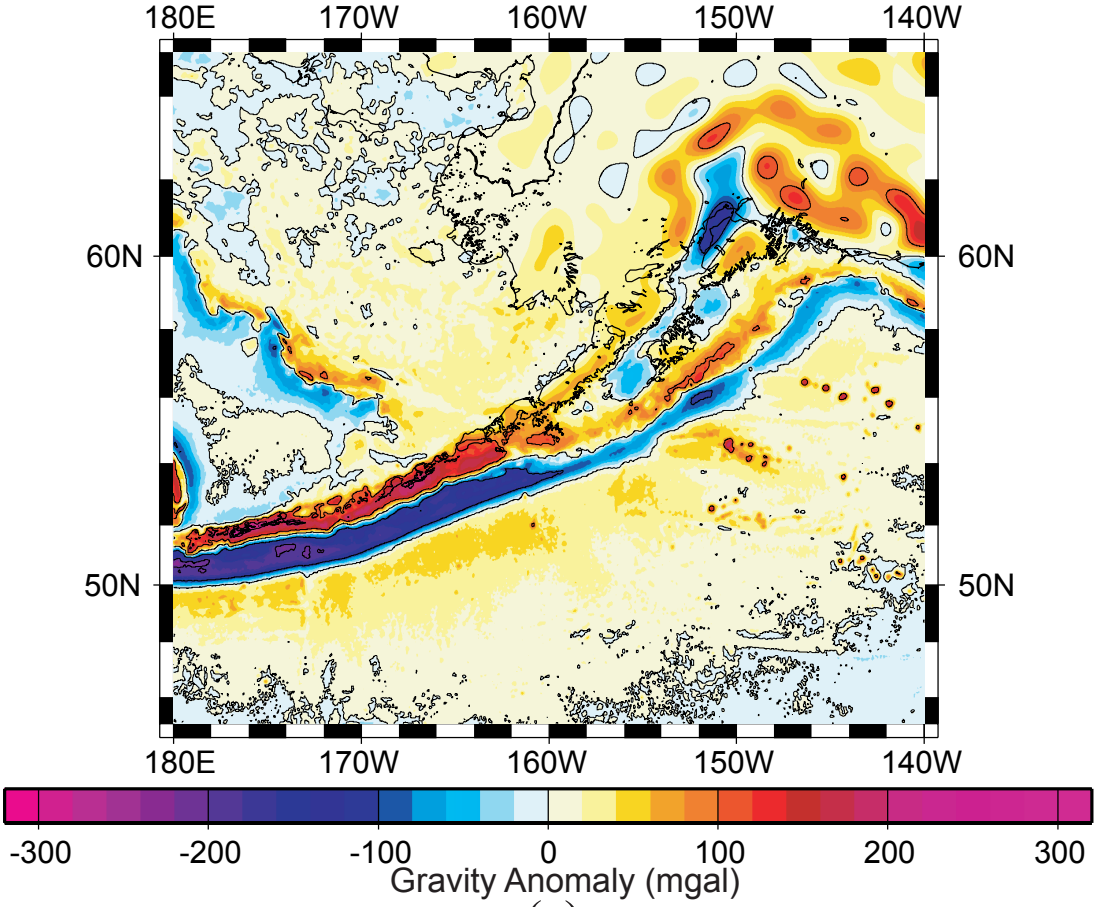
180E
170W
160W
150W
140W
60N
50N
-300
-200
-100
0
100
200
300
Gravity Anomaly (mgal)

(a)

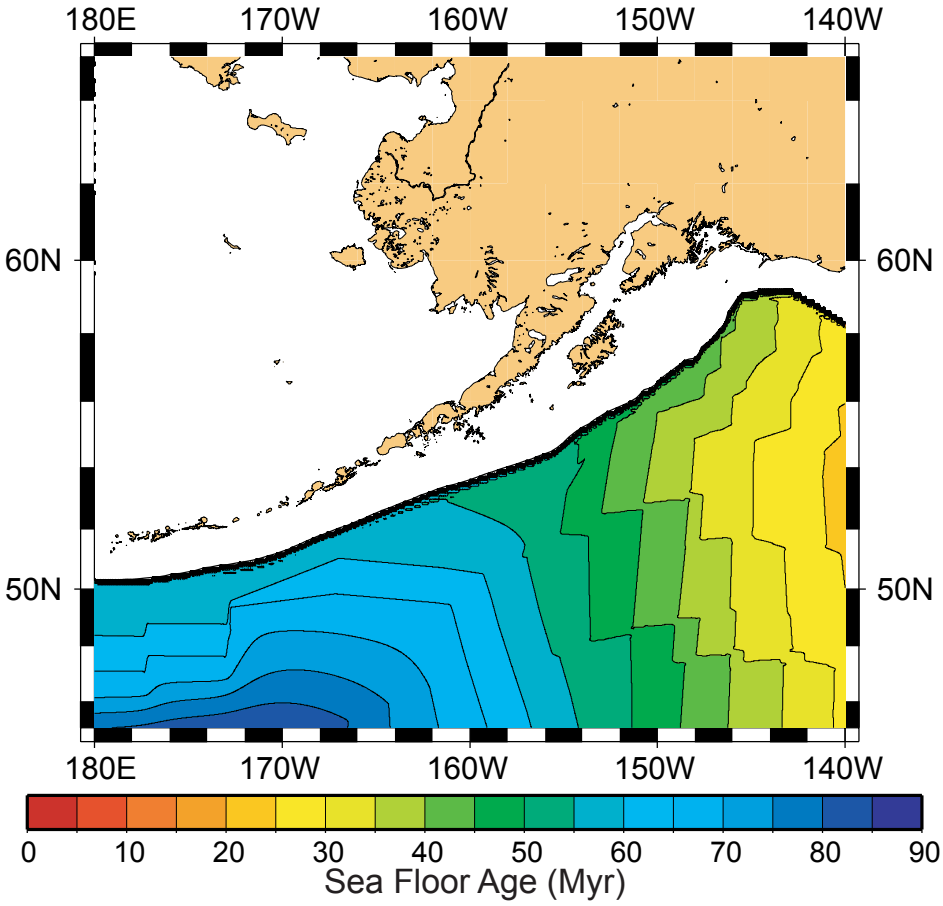
180E
170W
160W
150W
140W
60N
50N
0
10
20
30
40
50
60
70
80
90
Sea Floor Age (Myr)

(b)

Figure 19

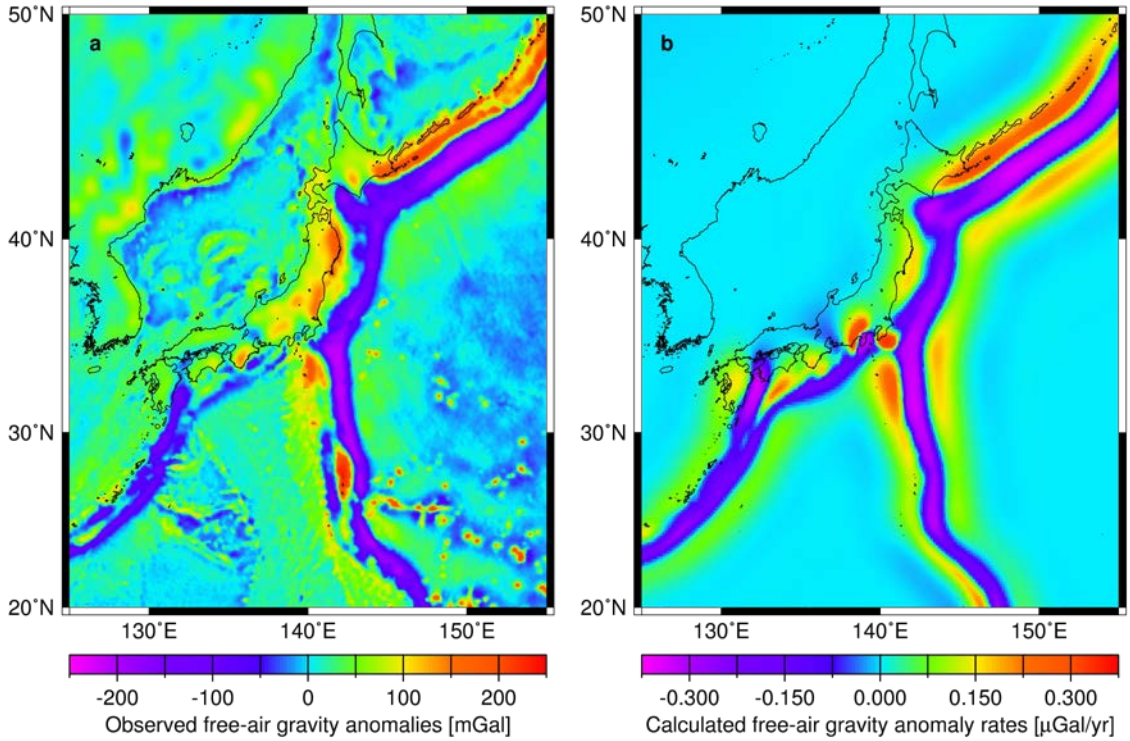
a
b
50°N
40°N
30°N
20°N
130°E
140°E
150°E
-200
-100
0
100
200
Observed free-air gravity anomalies [mGal]
-0.300
-0.150
0.000
0.150
0.300
Calculated free-air gravity anomaly rates [μGal/yr]

(a) (b)

Figure 20

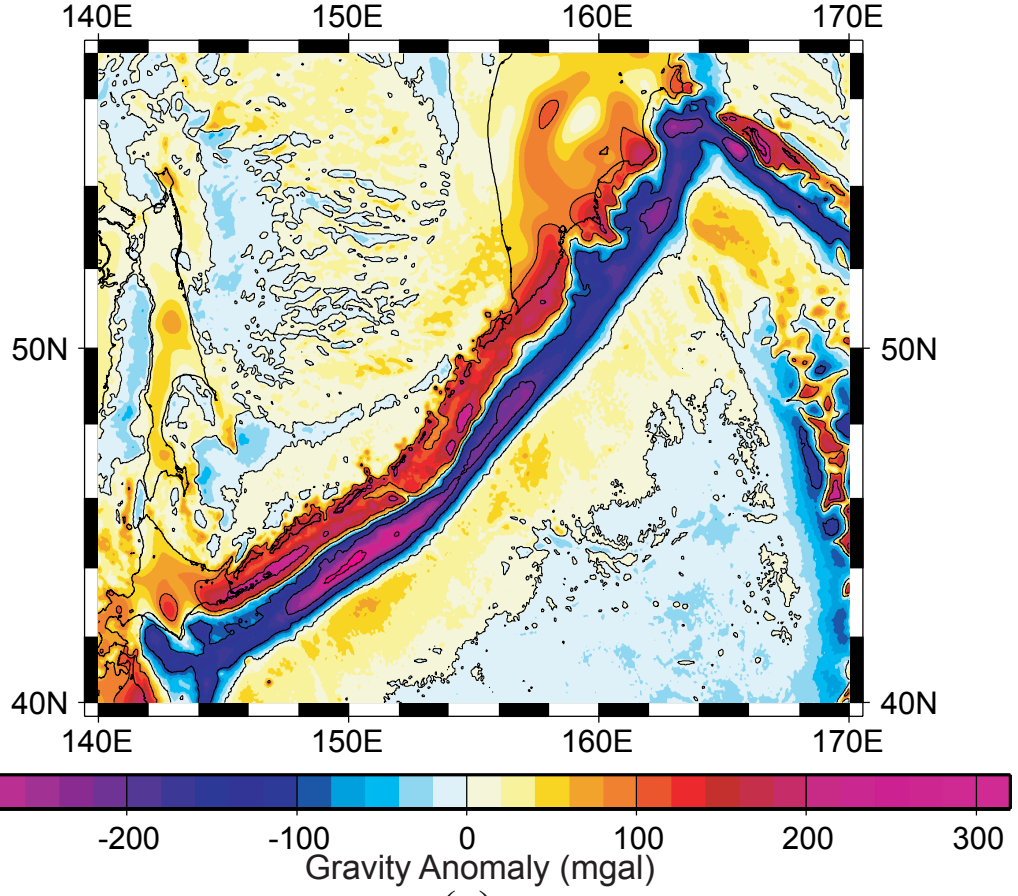
140E
150E
160E
170E
50N
40N
-300
-200
-100
0
100
200
300
Gravity Anomaly (mgal)

(a)

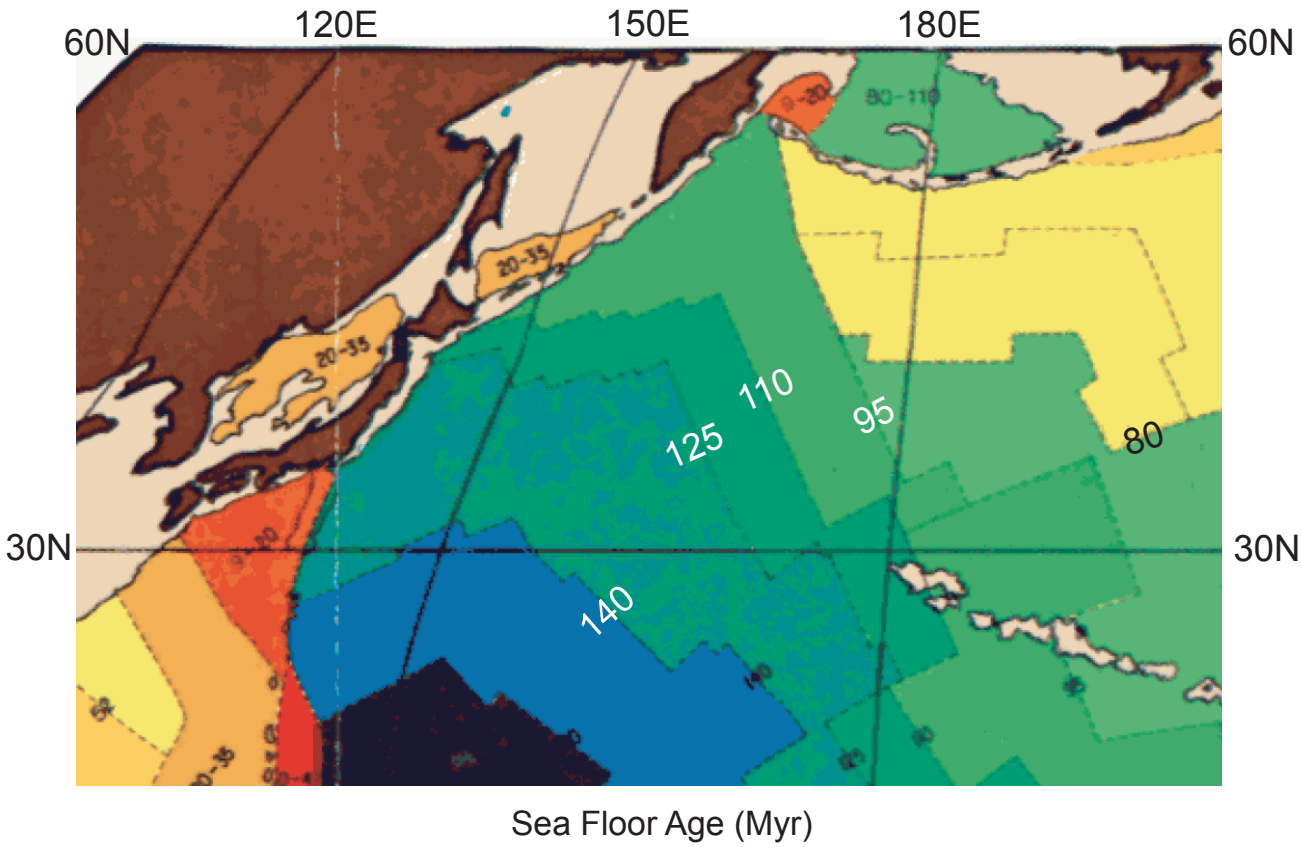
60N
120E
150E
180E
30N
125
110
95
80
140
Sea Floor Age (Myr)

(b)

Figure 21

Acknowledgements

First of all, I profoundly acknowledge my supervisor, Professor Mitsuhiro Matsu'ura of the University of Tokyo, for his continuous support, discussion, and advices throughout my doctoral course and this doctoral thesis. I do appreciate Professor Kengo Nakajima for his support and advice especially in the field of finite element method. I acknowledge Professor Yukitoshi Fukahata for his helpful discussions and continuous encouragement throughout the doctoral course.

I am deeply grateful to Professor Hikaru Iwamori, Professor Yasutaka Ikeda and Professor Takaya Iwasaki for their constructive criticisms and valuable comments. I appreciate the members of Professor Matsu'ura's laboratory, Dr. Chihiro Hashimoto, Dr. Akinori Hashima, Dr. Toshiko Terakawa, and Ms. Akemi Noda for their discussions and helpful comments especially in our marathon seminar. I am grateful to Professor Shoichi Yoshioka, Professor Toshinori Sato, Lecturer Satoshi Ide, Dr. Youichiro Takada, and other former and present members of Department of Earth and Planetary Science for their fruitful comments. I would like to thank all my friends for their warm encouragement.

Finally, I would like to express my gratitude to my family for their generous understanding and warm support.